

The atmospheric energy constraint on precipitation change ¹

Angeline G. Pendergrass

A dissertation
submitted in partial fulfillment of the
requirements for the degree of

Doctor of Philosophy

University of Washington

2013

Reading Committee:

Dennis L. Hartmann, Chair

Dargan M. W. Frierson

Gerard H. Roe

Program Authorized to Offer Degree:
Department of Atmospheric Sciences

¹Updated to correct typos.

University of Washington

Abstract

The atmospheric energy constraint on precipitation change ¹

Angeline G. Pendergrass

Chair of the Supervisory Committee:
Professor Dennis L. Hartmann
Department of Atmospheric Sciences

How does rain change with global warming? This dissertation investigates the rate of global-mean precipitation increase, changes in atmospheric radiative cooling, and the changes in frequency and intensity of rain events.

We examine changes in global-mean precipitation and atmospheric radiative cooling in comprehensive climate model simulations. In a realistic forcing scenario including both greenhouse gases and aerosols, clear-sky absorption of shortwave radiation is correlated with the rate of global-mean precipitation increase. In a scenario forced by increasing carbon dioxide alone, we make radiative transfer calculations to separate the responses of clear-sky atmospheric radiative cooling due to warming, moistening, and the carbon dioxide itself. Clear-sky atmospheric radiative cooling increases in response to vertically uniform warming and constant relative humidity moistening of the atmosphere. These increases are partially offset by decreases due to the direct radiative effects of carbon dioxide and black carbon. Global-mean precipitation increases by the same rate as the change in clear-sky atmospheric radiative cooling.

Changes in the frequency of rain and the rate at which it falls constitute the increase in global-mean precipitation. We develop a methodology for characterizing the frequency and amount of rainfall as functions of the rain rate. We define two

¹Updated to correct typos.

modes of response, one in which the distribution of rainfall increases in equal fraction at all rain rates (the increase mode) and one in which the rainfall shifts to higher or lower rain rates without a change in mean rainfall (the shift mode). We apply this description of change to simulations of global warming in climate models. We also calculate the response of the tropical rainfall distribution to ENSO phases in models and observations and apply the increase and shift modes. In addition to the increase and shift modes of change, some models show a substantial increase in rainfall at the highest rain rates. In some models this extreme mode can be shown to be associated with increases in grid-scale precipitation.

TABLE OF CONTENTS

	Page
List of Figures	iii
List of Tables	vi
Chapter 1: Introduction	1
1.1 Precipitation as a transfer of energy	2
1.2 Changes in global-mean precipitation and atmospheric radiative cooling	3
1.3 The distribution of precipitation and its change	5
1.4 Outline of the dissertation	7
Chapter 2: Global-mean precipitation and black carbon in AR4 simulations	9
2.1 Introduction	9
2.2 Data	10
2.3 Changes in global-mean precipitation and components of the atmospheric energy budget	12
2.4 Patterns of change in clear-sky atmospheric SW absorption	12
2.5 The timeseries of black carbon forcing	14
2.6 Contrast with CO ₂ -doubling scenario	18
2.7 Conclusions	19
Chapter 3: The atmospheric energy constraint on global-mean precipitation change	22
3.1 Introduction	22
3.2 Atmospheric energy and precipitation change	24
3.3 Radiative response to changes in moisture and temperature at a particular height	25
3.4 Atmospheric column radiative responses to idealized changes in temperature, moisture, and CO ₂	29

3.5	Inter-model spread in atmospheric radiative cooling response to CO ₂ forcing	42
3.6	Discussion	49
3.7	Conclusion	53
Chapter 4:	Changes in the distribution of rain in response to warming in models and observations	55
4.1	Introduction	55
4.2	Data and methods	56
4.3	The rain amount distribution and its change	62
4.4	Implications for changes in frequency distribution	84
4.5	Differences across models	95
4.6	Discussion	107
4.7	Conclusions	113
Chapter 5:	Concluding remarks	115
Appendix A:	Model simulations	130
Appendix B:	Rain amount and rain frequency distribution calculations	133

LIST OF FIGURES

Figure Number	Page
2.1 Rate of precipitation increase versus change in atmospheric radiative cooling	13
2.2 Maps of clear-sky atmospheric shortwave absorption change in NCAR CCSM 3 and GFDL CM2.1	15
2.3 Timeseries of clear-sky shortwave absorption and precipitation in NCAR CCSM 3.0 and GFDL CM 2.0 and 2.1	17
2.4 Rate of precipitation increase versus change in clear-sky shortwave absorption for carbon dioxide increase forcing scenario	20
3.1 Global-mean precipitation increase in CMIP5 models	24
3.2 Zonal-mean cross sections of temperature and moisture changes in CMIP5 models	27
3.3 TOA, surface, and atmospheric column radiative responses to the vertical structure of warming and moistening	29
3.4 Atmospheric column LW and SW radiative responses to the vertical structure of warming and moistening	30
3.5 Global mean of the baseline temperature and relative humidity profiles used for idealized calculations	31
3.6 Radiative response to vertically-uniform warming, constant-relative-humidity moistening, and carbon dioxide increase	34
3.7 Radiative response to vertically-varying warming with constant-relative-humidity moistening	37
3.8 Radiative response to idealized low and high clouds	41
3.9 Clear-sky atmospheric radiative cooling and the rate of global-mean precipitation increase across CMIP5 models	44
3.10 Comparison of GCM radiative responses with radiative transfer model calculations	45
3.11 Contributing factors to inter-model spread in precipitation and radiative response at the TOA and in the atmospheric column	46

3.12	The compensation between TOA and atmospheric column radiative responses to lapse rate and water vapor change	47
3.13	Relationship of the radiative response to vertically-varying and vertically-uniform constant-RH moistening with the response to changing lapse rate	49
4.1	Rain amount and rain frequency distributions in the CMIP5 multi-model mean and observations	64
4.2	Rain amount distribution in CMIP5 models compared with GPCP observations	66
4.3	Schematic of the modes of change of the rain distribution	69
4.4	Modes of change of the rain distribution compared to the CMIP5 multi-model mean response	71
4.5	Rain amount response to carbon dioxide increase, with fitted shift and increase modes, for the CMIP5 multi-model mean	75
4.6	Rain amount response to carbon dioxide increase, with fitted shift and increase modes, for CMIP5 models	77
4.7	Shift mode versus error of fit	78
4.8	Increase mode versus global-mean precipitation change	79
4.9	Rain amount response to ENSO phases, with fitted shift and increase modes, in observations and models	81
4.10	Magnitude of the shift and increase modes fit to response to ENSO phases in observations and models over land and ocean	83
4.11	Magnitude of the shift and increase modes fit to responses to CO ₂ increase and ENSO phases in models over land and ocean	85
4.12	Rain frequency response to carbon dioxide increase in CMIP5 multi-model mean	87
4.13	Extreme rain rate response to carbon dioxide increase in the CMIP5 multi-model mean	90
4.14	Extreme rain rate response to carbon dioxide increase in CMIP5 models	92
4.15	Extreme rain rate response to carbon dioxide increase and ENSO phases over land	93
4.16	Extreme rain rate response to ENSO phases in models and observations	94
4.17	Unresolved (convective) rain distribution in three models	98
4.18	Maps of the rain amount falling in heavy events in observations and MPI-ESM-LR and GFDL-ESM2G model simulations	101

4.19	Evolution of a heavy rain event in MPI-ESM-LR	103
4.20	Evolution of a heavy rain event in GFDL-ESM2G	104
4.21	Rain amount and extreme rain rate responses to carbon dioxide doubling and quadrupling in three models	105
4.22	Rain amount and extreme rain rate response to ENSO phases in two models	109
4.23	Vertical velocity and its change as a function of rain rate in three models	112

LIST OF TABLES

Table Number		Page
2.1	CMIP3 models ranked by rate of precipitation increase	11
3.1	Changes in CMIP5 multi-model, global-mean atmospheric energy budget components	25
3.2	Clear-sky radiative response to warming, moistening, and carbon dioxide from radiative transfer calculations	33
3.3	Comparison of CMIP5 radiative response with radiative transfer model calculations	40
3.4	Radiative response to idealized clouds	40
4.1	Shift and increase modes fit to CMIP5 model response to carbon dioxide increase	76
4.2	Shift and increase modes fit to the response to ENSO phases in observations and models	82
4.3	Dry-day frequency and extreme rain rate response to carbon dioxide increase in CMIP5 models	88
4.4	Dry-day frequency and extreme rain rate response to ENSO phases in observations and models	89
4.5	Responses to doubling, tripling, and quadrupling of carbon dioxide . .	106
4.6	CMIP5 models sorted by magnitude of shift mode and 99.99th percentile rain rate response to ENSO phase as consistent or inconsistent with observations	108
A.1	CMIP5 models	131

ACKNOWLEDGMENTS

Dennis Hartmann is the best advisor I could have hoped for. Dennis is good at science and also at life, and I'm very grateful I had the opportunity to work with him and learn from him.

I have the best committee imaginable. Dargan Frierson has provided lots of encouragement and he's been a good sounding board, as well as showing me how to teach. Gerard Roe taught me most of what little rhetoric I know, and kept me on my toes about what is and is not a feedback. Qiang Fu is another great scientific role model, and provided the most interaction of all of my committee members if interaction is counted in the number of times I ran his radiation model. LuAnne Thompson is a great example of an interdisciplinary scientist, as well as helping me find my way onto an oceanography cruise.

Many other faculty have contributed to my experience in grad school. David Battisti and Greg Hakim contributed considerable energy to my development as a scientist, and I learned a lot from them. I am grateful for all the teachers I've had, in the many wonderful classes I took, and also in the course of life here.

Brian Soden has been an ongoing source of support and scientific interaction throughout my education. My work with him when I was an undergrad started me down the path that led to this dissertation.

I've learned plenty not just from professors but also from my peers. I've been fortunate to have classmates, officemates, and fellow students who not only put up with me but also enrich my experience, and plenty of people who will talk to me about science, careers, and life over the years. I am especially grateful for Brian Smoliak for

the enormous support he has provided me.

The department staff are phenomenal. In particular, Marc Michelsen's technical support was crucial.

Graduate school isn't only about academics; one must also sustain oneself physically and emotionally. I've had great friends outside of school. Naomi Goldenson and Genevieve Walker in particular have helped me thrive while working on my PhD. I've also had many great activity partners and coffeeshop friends who made my time in Seattle enjoyable and taught me plenty of non-academic skills.

Last and definitely not least I must thank my Mom, Dad, brother, and Grandma. I am lucky to have a supportive family who I know are also my biggest fans.

DEDICATION

to everyone

Chapter 1

INTRODUCTION

Precipitation is a crucial component of the climate system from any perspective. It carries water from the ocean to the land surface. Its latent heating drives the atmospheric circulation. Both because of its impacts on the environment and society, and because of its role in the dynamics of the climate systems, it is important that we answer the question, how does precipitation change in response to global warming?

Precipitation is highly variable in space and time. It depends on processes at a wide range of scales, from global circulation (thousands of kilometers) to interactions of water vapor with aerosols (nanometers). This makes it difficult to measure and also simulate. Climate model simulations present a laboratory in which a diagnosis of fundamental drivers of precipitation change is possible.

This dissertation explores the energetic constraints on global precipitation change. By examining precipitation change in climate model simulations, we consider the following questions :

- How does atmospheric radiative cooling change in response to climate forcing?
- How does precipitation respond to these changes, in the global mean and in terms of its frequency and intensity?

This chapter will proceed with an overview of some aspects of the climate response to greenhouse gas forcing relevant to precipitation. Then, we will provide background on precipitation and its role in the surface and energy budget. Next we will present some background information on the distribution of precipitation and its changes. Finally, we will outline the contents of the dissertation.

1.1 Precipitation as a transfer of energy

The atmosphere exchanges energy via turbulent fluxes of heat and moisture with the surface, and radiatively with both the surface and space. The global-mean atmospheric energy budget, E_a , is described by Equation 1.1,

$$\frac{dE_a}{dt} = LE + SH + R. \quad (1.1)$$

Latent heat flux enters the atmosphere through evaporation of water from the surface, LE . The water budget is in balance on interannual and longer timescales, so evaporation and precipitation must be equal. Therefore the latent heat flux entering the atmosphere must be equal to LP , when the latent heat of condensation of water, L , is multiplied by the rain rate in $\text{kg m}^{-2} \text{ s}^{-1}$, P . Sensible heat flux, SH , is the turbulent transfer of heat from the surface to the atmosphere. The atmospheric column net radiation, R , is the sum of net radiant energy leaving the atmosphere through its top (to space) and its bottom (to the earth's surface). We can quantify these terms by examining the multi-model mean from ten years of climate model simulations (see Chapter 3 for details of the simulations). In these simulations, on average, LP is 85 W m^{-2} , SH is 20 W m^{-2} , R is -105 W m^{-2} , and these terms balance since storage of energy in the atmosphere is small. Compilations of the components of the planetary energy budgets based on observations were presented by Kiehl and Trenberth (1997), and updated by (Stephens et al., 2012).

Latent and sensible heat fluxes transfer energy to the atmosphere from the surface, and the atmospheric radiation removes this energy. If any one of these three terms changes, the other terms change to maintain balance. In the first part of this dissertation, we will focus on how R and LP balance. In the second part, we will focus on the ways in which P changes.

1.2 Changes in global-mean precipitation and atmospheric radiative cooling

As we just saw, precipitation is a substantial contributor to the atmosphere's energy budget. It also plays an important role in the water cycle by transferring moisture between the surface and atmosphere. In response to climate change, moisture changes by close to the Clausius-Clapeyron rate of $7\% \text{ K}^{-1}$, while precipitation changes at just $2\% \text{ K}^{-1}$, much less quickly (Held and Soden, 2006). Mitchell et al. (1987) was the first to establish that atmospheric radiative cooling plays the primary role in determining the rate at which global-mean precipitation increases in response to warming. This study examined in detail an early climate model simulation of the response to carbon dioxide (CO_2) increase, calculating contributions of latent heating to the atmospheric energy budget in the model simulation were calculated and comparing them with estimates of the change in radiative cooling due to warming, moistening, and CO_2 increase. Later, Boer (1993) showed that in equilibrium simulations of CO_2 doubling, the surface energy budget also balances precipitation change. More recently, Allen and Ingram (2002) popularized the atmospheric energy budget as the key constraints on precipitation change.

1.2.1 Response to realistic forcing including aerosols

The balance between changes in atmospheric cooling and precipitation change should be evident in modern climate model simulations. Model inter-comparisons of climate projections show large variations in the rate of global-mean precipitation increase per degree warming, but some studies had trouble reconciling these changes in precipitation with atmospheric cooling in realistic forcing experiments from the Coupled Model Intercomparison Project, phase 3 (CMIP3). These experiments include aerosol and ozone forcing in addition to greenhouse gases. Lambert and Allen (2009) formed a statistical model for directly-forced and temperature-dependent precipitation responses,

but had little success in using it to explain 21st-Century projections for global-mean precipitation change. Previdi (2010) adapted a popular technique used to study the top-of-atmosphere (TOA) radiation budget to the atmospheric column. While this allowed them to quantify the temperature-dependent response of the atmospheric energy budget, they found that other changes in atmospheric radiative cooling were also needed to explain the differing rates of precipitation increase. Shiogama et al. (2010) showed that the rate of increase of precipitation depends on the emissions scenario considered, but did not explain how.

At the same time, the role absorbing aerosol forcing plays in the atmospheric energy budget was becoming clearer. Ramanathan et al. (2001) reviewed both direct (radiative) and indirect (cloud) effects of aerosols. The absorbing and reflecting direct radiative effects of aerosols have very different effects on the hydrologic cycle. Andrews et al. (2010) and Ming et al. (2010) proposed formulas for radiative forcing of the hydrologic cycle, in which absorbing aerosol forcing is highlighted as having a much different effect from other forcings.

In Chapter 2, we investigate the differences in atmospheric radiative cooling in the CMIP3 realistic forcing scenario, how clear-sky shortwave radiation changes in these simulations, and how it relates to the change in global-mean precipitation.

1.2.2 Response to increasing carbon dioxide

We ought to be able to thoroughly understand the atmospheric radiative cooling response to a straightforward forcing such as a well-mixed greenhouse gas. The TOA radiation budget determines the amount of warming that occurs due to climate forcings, and it has been studied thoroughly, when compared to atmospheric radiative cooling. Some aspects of TOA radiative cooling that are well documented include the water vapor and lapse rate feedbacks (Manabe and Wetherald, 1967; Held and Soden, 2000), and cloud feedbacks (Schneider, 1972). One interesting feature of the response is the compensation of the water vapor and lapse rate feedbacks (Cess, 1975).

A similarly thorough understanding of the atmospheric radiative cooling is desirable. Some studies have begun this endeavor. Mitchell et al. (1987) made important calculations with an early climate model. Allen and Ingram (2002) brought different calculated estimates together to show how global-mean precipitation change has temperature-dependent and temperature-independent components. Allan (2006) examined changes in clear-sky longwave cooling due to water vapor change in observations. Stephens and Ellis (2008) examined the combined response to warming and moistening with an empirical formula for radiation change as a function of column water vapor. Previdi (2010) adapted the radiative kernel technique from the TOA to the atmospheric column.

Lacking from these studies is a consistent calculation of the contributions to the change in atmospheric radiative cooling, which would allow us to form a complete picture of its response. We will rectify this in Chapter 3.

1.3 The distribution of precipitation and its change

Atmospheric radiative cooling and precipitation must balance in the global, annual mean. But how the precipitation response manifests in frequency and intensity is not obvious. Whereas in the first part of this dissertation we will focus on the global-mean precipitation change and its balance with changes in atmospheric cooling, in the second part we will consider the character of the change in precipitation.

The rate of rainfall (or its intensity) varies by orders of magnitude in time and space, from 0.1 mm d^{-1} to 1350 mm d^{-1} (the highest daily accumulation present in the GPCP 1DD dataset, presented in Chapter 4). For comparison, the present-day global mean rainfall is 2.67 mm d^{-1} (again in GPCP), equivalent to 76 W m^{-2} of latent heat release. If we consider finer temporal resolution (hourly or instantaneous measurements) at a single point in space, we would find an even larger range of rain rates. And often, it is not raining at all.

In order to study the distribution of rainfall, we must quantify it. This can be done

by considering the frequency of rainfall for some range of rain rate. Alternatively, we can consider how much rain falls in some range of rain rates, which is the rain amount distribution.

There is reason to suspect that the distribution of precipitation changes with warming. The heaviest rain events increase, according to various measures, at a rate similar to the increase in moisture. Trenberth (1999) argued that the disparity between the rate of increase of moisture, about 7 % K⁻¹, and global-mean precipitation, 1-3 % K⁻¹, implies that rain must become less frequent, but more intense. This prompts questions, including: How does the distribution change? By how much? And, Why?

It has been confirmed that the rain rate of extreme events in model simulations forced by carbon dioxide increase goes up by at least 5.5 % K⁻¹. Allen and Ingram (2002) and Pall et al. (2007) noted that rain rates at the highest percentiles increase at about the same rate as water vapor under a climate change scenario in one global climate model (GCM). The rain rate of these events scales a measure of moisture convergence. Early studies used specific humidity (Emori and Brown, 2005), whereas recent studies have used the vertical derivative of saturation specific humidity (O’Gorman and Schneider, 2009b), along with vertical velocity. This scaling works in the Extra-tropics, but less well in the Tropics (O’Gorman and Schneider, 2009a; Sugiyama et al., 2010). There has been controversy about whether or not models and observations agree on the rate of change of extreme precipitation (Allan and Soden, 2008), though the discrepancy is greatly reduced by considering the large differences in response at inter-annual and centennial timescales in models (O’Gorman, 2012; Allan et al., 2013).

Other studies have considered changes in moderate and light rain events and the frequency of dry events in addition to extreme events. These studies have established a pattern of change, with increases at high rain rates and decreases at moderate rain rates. Sun et al. (2007) found increases in total wet-day intensity of just 2 % K⁻¹, and

decreases in total wet-day frequency in model simulations of climate change. Allan and Soden (2008) saw an increase in heavy rain events and decrease in moderate events with warming in observations of inter-annual variations. Lau et al. (2013) reaffirmed the pattern in CMIP5 models, and also documented an increase in light rain frequency. Chou et al. (2012) decomposed changes in the distribution of Tropical rain into thermodynamic (moistening) and dynamic (vertical velocity) components. They found that moistening increased the frequency of rainfall at all rain rates, but vertical velocity was responsible for decreasing frequency as well as the change in shape of the change in distribution. The importance of changes in vertical velocity is interesting, especially in light of recent research about the Tropical vertical velocity response to climate change (e.g., Vecchi and Soden, 2007).

A crucial factor in the Trenberth (1999) argument for changes in the distribution of precipitation is the discrepancy between the rates of mean and extreme precipitation change. But, our understanding of the connection between changes in mean and extreme precipitation is tenuous. A framework that quantifies the relationship between changes in precipitation at different rain rates is needed. In Chapter 4, we introduce such a framework, and then apply it to understand the changing distribution of precipitation.

1.4 Outline of the dissertation

This dissertation has two parts. The first part addresses how atmospheric radiative cooling changes on long timescales, and how these changes are connected to global-mean precipitation change. To do this, we examine sets of comprehensive climate model simulations. Chapter 2 investigates changes in the rate of increase of global-mean precipitation in a suite of simulations with realistic forcing, including greenhouse gas as well as changes in aerosols and ozone. This chapter highlights the role that shortwave absorption by aerosols plays in driving changes in global-mean precipitation. In Chapter 3 we focus on the atmospheric radiative cooling response to

carbon dioxide forcing. We present detailed calculations of the clear-sky atmospheric radiative cooling response to carbon dioxide increase and the patterns of warming and moistening in comprehensive climate models. Then we examine the differing radiative cooling and precipitation responses across the suite of model simulations.

The second part of the dissertation, Chapter 4, addresses how the distribution of precipitation responds to balance the change in atmospheric cooling. We introduce two modes to quantify coherent changes in the distribution of rain. Then, we apply these modes to understand the response of the distribution of rain to carbon dioxide increase, including changes in rain amount and rain frequency. We explore the response of extreme rain rate in the models, and the modes of change of extreme rain rate. We make composites of the observed Tropical rain distribution response to warm and cold phases of El Niño and the Southern Oscillation (ENSO), and apply the modes to these responses. Finally, we compare observed and modeled responses to ENSO phases.

Chapters 2 and 3 have already been published in scientific journals, and were adapted for inclusion into the dissertation. Chapter 2 is published as Pendergrass and Hartmann (2012), *Global-mean precipitation and black carbon in AR4 simulations*.¹ Chapter 3 is published as Pendergrass and Hartmann (in press).²

¹Copyright 2012 by the American Geophysical Union. Included by permission of John Wiley & Sons, Inc.

²©American Meteorological Society. Used with permission.

Chapter 2

GLOBAL-MEAN PRECIPITATION AND BLACK CARBON IN AR4 SIMULATIONS

In this chapter, we consider the changes in atmospheric radiative cooling and precipitation in a suite of comprehensive model simulations with a realistic forcing scenario.

2.1 Introduction

Held and Soden (2006) showed that in the the Intergovernmental Panel on Climate Change (IPCC) Fourth Assessment Report (AR4, IPCC, 2007) Special Report on Emission Scenarios (SRES, Nakicenovic and Swart, 2000) A1b forcing experiment, global-mean precipitation increases by 1-3% per degree of global-mean surface temperature increase. This inter-model spread in precipitation response corresponds to $1.6 \text{ W m}^{-2} \text{ K}^{-1}$. What causes this large range in precipitation response?

Reflecting aerosols in the atmosphere decrease the amount of shortwave (SW) radiation reaching the surface, which both cools the surface and decreases the amount of energy available for evaporation. The effects of absorbing aerosols vary with their height, but they decrease precipitation in most cases (Ming et al., 2010); their effect on surface temperature is smaller than the effect of reflecting aerosols or greenhouse gases (GHGs, Shiogama et al., 2009). The additional SW absorption adds heat directly to the atmosphere, which causes a decrease in the latent heating that would otherwise occur.

How precipitation varies across AR4 forcing scenarios was the focus of two recent studies. Shiogama et al. (2010) found that changes in global-mean precipitation

depend on the emissions scenario, with black carbon showing a significant effect, but their surface energy budget perspective precluded an explanation. Frieler et al. (2011) determined that precipitation changes across AR4 scenarios and models can be skillfully predicted from longwave (LW) and SW absorption and global-mean surface temperature change.

Increased black carbon forcing results in decreased global-mean precipitation in most but not all modeling studies. Black carbon also affects surface temperature, but this effect is small. Shiogama et al. (2009) compared integrations of the Model for Interdisciplinary Research on Climate (MIROC) separately forced with GHGs, black carbon, and sulfate aerosols, and found that black carbon forcing decreases precipitation. Roberts and Jones (2004) used the Hadley Center climate model (HadSM4) with online chemistry to find a very slight increase in global-mean precipitation at equilibrium with black carbon forcing, which is inconsistent with other studies. Andrews et al. (2010) updated Roberts and Jones (2004) using a newer version of the Hadley Center model (HadGEM1) and found that black carbon forcing decreases precipitation.

Here we explore how black carbon forcing influences the inter-model spread in global-mean precipitation change in IPCC AR4. We focus on two models and the A1b forcing scenario in order to explore in depth one reason why global-mean precipitation varies among models.

2.2 Data

For this study, we use data from the World Climate Research Programme's (WCRP's) Coupled Model Intercomparison Project phase 3 (CMIP3) multi-model dataset (Meehl et al., 2007b). Variables include surface air temperature (T), precipitation (P), total-sky and clear-sky LW and SW upwelling and downwelling radiation at the surface and upwelling radiation at the top-of-atmosphere (TOA) for models where these fields are available. Clear-sky downwelling LW radiation at the surface is not available for

National Center for Atmospheric Research Community Climate System Model 3.0 (CCSM3). Only the first ensemble member for each model is shown. In models with multiple ensemble members, the additional members have similar changes in precipitation and temperature to the first. For each variable and each model, the area-weighted global means are taken and the differences between twenty-year means of the monthly data from the beginning (2011-2030) and end (2080-2099) of the 21st-Century are computed (indicated by Δ). Atmospheric SW absorption is calculated by adding surface upwelling and TOA downwelling and subtracting surface downwelling and TOA upwelling; LW cooling is the same calculation with all signs reversed. Atmospheric SW absorption and LW cooling are normalized by the difference in global-mean surface temperature (ΔT). L is the latent heat of vaporization of water, which we multiply by ΔP for comparison with energetic changes. $L\Delta P/\Delta T$ computed in this way is the hydrologic sensitivity. Table 2.1 lists the models in descending order of $L\Delta P/\Delta T$, which varies from 2.1 to $0.57 \text{ W m}^{-2} \text{ K}^{-1}$ (a factor of 3.7).

2.3 Changes in global-mean precipitation and components of the atmospheric energy budget

Figure 2.1 shows $L\Delta P/\Delta T$ plotted against changes in clear-sky atmospheric SW absorption, clear-sky atmospheric LW cooling, and changes in LW and SW cloud radiative forcing (the difference between the total- and clear-sky radiative fields). If GHG forcing and water vapor feedback cause changes in precipitation, then precipitation change should correlate well with the changes in atmospheric LW cooling. While clear-sky atmospheric LW cooling change does explain most of the increase in $L\Delta P$ when it is not normalized by ΔT ($r = 0.73$, $r^2 = 0.53$, not shown), it correlates poorly with $L\Delta P/\Delta T$. This is because water vapor concentration depends strongly on temperature and largely determines clear-sky atmospheric LW cooling; normalizing by ΔT removes this dependence. Often, we think that intermodel spread in AR4 simulations is dominated by clouds (Bony et al., 2006); however, Figure 2.1 shows no

Table 2.1: Models ranked by $L\Delta P/\Delta T$ in the 21st Century of IPCC AR4 A1b scenario, and their changes in global-mean precipitation and total-sky SW absorption. Boldfaced models include black carbon forcing (Table 10.1, IPCC, 2007).

HS rank	Model name	$L\Delta P/\Delta T$ (W m ⁻² K ⁻¹)	$L\Delta P$ (W m ⁻²)	ΔSW (W m ⁻²)
1	NCAR CCSM3.0	2.1	3.5	0.094
2	MRI CGCM2.3.2A	1.8	3.2	0.47
3	IPSL CM4	1.8	4	2.5
4	MPI ECHAM5	1.8	4.7	2.7
5	CCCMA CGCM3.1	1.6	2.6	1.9
6	CCCMA CGCM3.1 T63	1.6	3.3	2.1
7	CNRM CM3	1.6	3.1	2.1
8	INMCM3.0	1.4	2.2	0.88
9	MIROC3.2 HiRes	1.4	4.3	3.8
10	MIROC3.2 MedRes	1.4	3.3	3.2
11	UKMO HadGEM1	1.1	2.6	4
12	MIUB ECHO G	0.98	2.1	3
13	UKMO HadCM3	0.88	1.9	2.6
14	GFDL CM2.0	0.73	1.5	3.7
15	GFDL CM2.1	0.57	1	3.4

significant relationship between $L\Delta P/\Delta T$ and changes in SW or LW cloud radiative forcing. On the other hand, $L\Delta P/\Delta T$ correlates well with changes in clear-sky atmospheric SW absorption, explaining over half of the intermodel spread ($r = -0.78$, $r^2 = 0.61$).

2.4 Patterns of change in clear-sky atmospheric SW absorption

Water vapor and absorbing aerosols are the main SW absorbers in the troposphere expected to change in the next century, aside from clouds. To explore how clear-sky atmospheric SW absorption changes in the 21st Century, we focus on two of the AR4 models: the model with the greatest precipitation increase and smallest increase in clear-sky atmospheric SW absorption, CCSM3, and the model with the smallest precipitation increase and largest increase in clear-sky atmospheric SW absorption, Geophysical Fluid Dynamics Laboratory Coupled Model 2.1 (CM2.1).

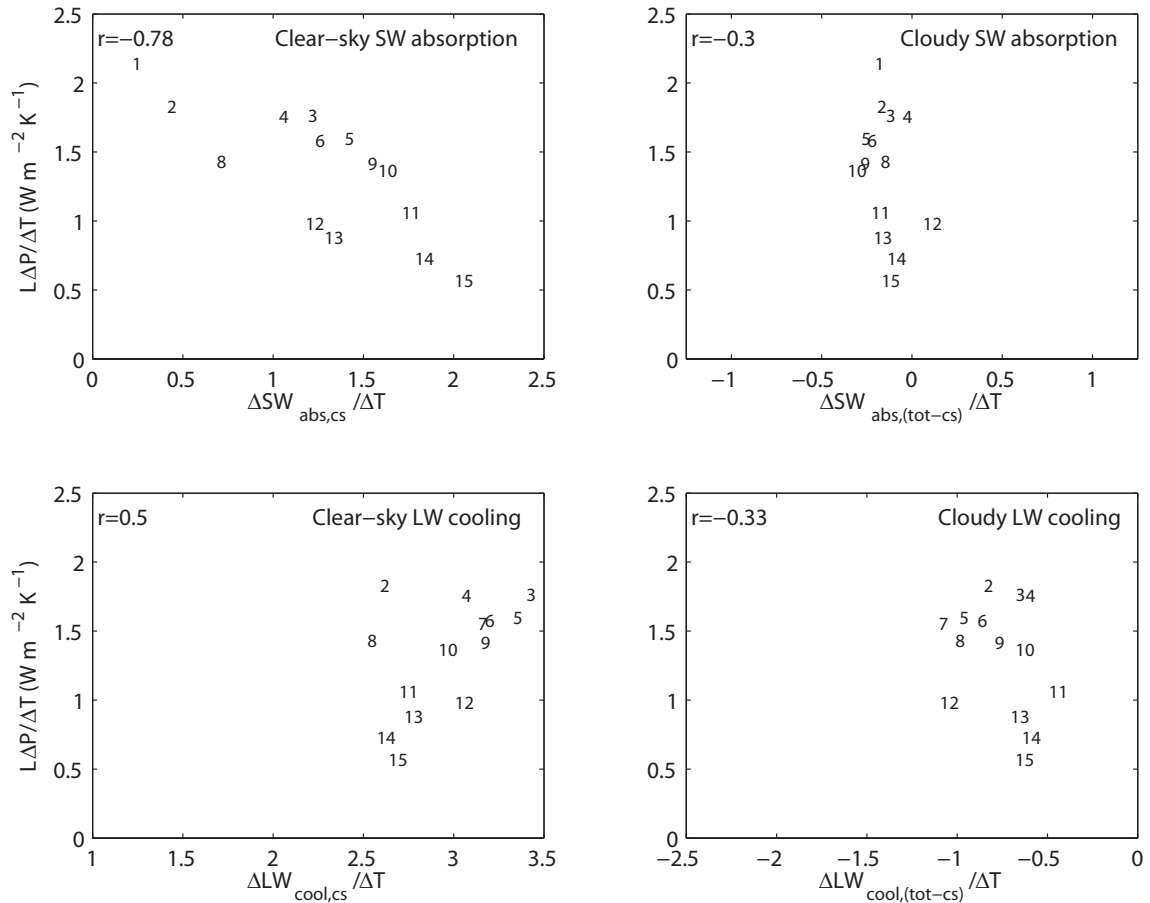


Figure 2.1: IPCC AR4 A1b forcing scenario 21st-Century changes in global-mean precipitation, clear-sky atmospheric SW absorption and LW cooling and SW and LW cloud radiative forcing per degree global-mean surface temperature change. See Table 1 for model key. LW cooling data is not available for Model 1.

Figure 2.2 shows A1b scenario 21st-Century change in clear-sky atmospheric SW absorption for CCSM3 and CM2.1. In CCSM3 SW absorption decreases, except in limited regions over the Tropics, while in CM2.1 it increases almost everywhere. Using feedback kernels for atmospheric column radiation from Previdi (2010), we remove the increase in absorption due to water vapor concentration increase. Previdi (2010) showed this calculation for four models from AR4 A1b, including CM2.0 and CM2.1, but not for CCSM3. The residual change in clear-sky SW absorption (total minus increased water vapor absorption) strongly resembles the spatial pattern of anthropogenic absorbing aerosol emissions. Tropospheric ozone changes have not been accounted for in this analysis, but these effects are likely to be small because fractional changes of tropospheric ozone in the 21st Century are small (Wigley et al., 2002). The sign of the residual change is negative in CCSM3 and positive in CM2.1.

2.5 The timeseries of black carbon forcing

The treatment of aerosols in IPCC AR4 model runs was documented in Table 10.1 of Meehl et al. (2007a). While the SRES scenarios specified GHG and sulfate aerosol emissions, they did not specify the black carbon forcing. Modeling groups took different approaches to incorporating black carbon forcing in the 21st Century. Most models did not include it at all; the ones that did are bold in Table 2.1. Models that do not include black carbon forcing can still have changes in absorbing aerosol forcing from sulfate aerosol changes, depending on the optical properties of sulfate aerosol in the model. CCSM3 scaled the present geographical concentrations of black carbon by projections of global mean sulfate (SO_x) aerosol burden, reported in Meehl et al. (2006). In contrast, an atmospheric chemistry model was used in CM2.0 and CM2.1 (CM2) to interactively calculate concentrations of black carbon (Horowitz et al., 2003). Concentrations of black carbon closely follow emissions because black carbon is short-lived in the atmosphere (Horowitz, 2006). The present-day spatial pattern of black carbon emissions scaled by the timeseries of global-mean carbon monoxide (CO) burden

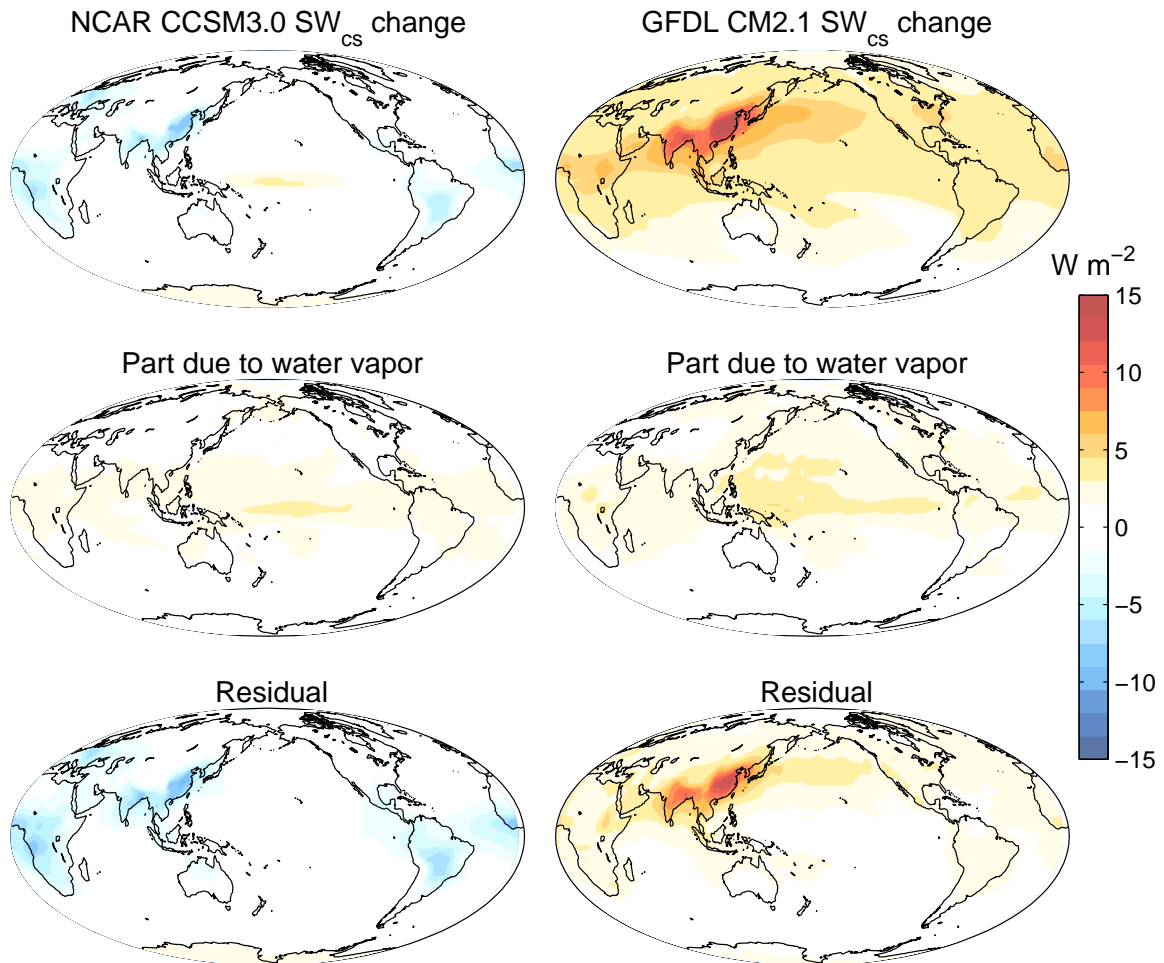


Figure 2.2: Change in clear-sky atmospheric SW absorption in A1b scenario for the 21st century of (left) NCAR CCSM 3 and (right) GFDL CM 2.1. (Top) Clear-sky atmospheric SW absorption change. (Middle) Part of clear-sky atmospheric SW absorption change due to water vapor increase, calculated with radiative kernels from Previdi (2010). (Bottom) Residual change in clear-sky atmospheric SW absorption. Solid contours are positive changes and dashed contours are negative changes; contour interval is 1.5 W m^{-2} ; and shaded areas are at least 1.5 W m^{-2} different from zero. Global mean of bottom left panel is -1.0 W m^{-2} and bottom right is 1.7 W m^{-2} .

drove the chemistry model in CM2 according to Levy et al. (2008). We obtain the SO_x and CO timeseries from 2000 to 2100 from the A1 scenario of the Asian Pacific Integrated Model (AIM) scenario from SRES (<http://www.grida.no/climate/ipcc/emission>, accessed 8/31/2011, Nakicenovic and Swart, 2000); the bottom left panel of Figure 2.3 shows them converted to black carbon timeseries following Meehl et al. (2006) for CCSM3 and Levy et al. (2008) for CM2. In CCSM3, black carbon increased until 2020 and then declined for the remainder of the century, ending lower than the 2000 values. In CM2, the emissions increased slowly but steadily throughout the century, nearly doubling from 2000 to 2100. The top left panel of Fig. 2.3 shows the timeseries of the clear-sky SW absorption with the contribution from water vapor removed, using feedback kernels as in Section 2.4. For CM2, the steady increase in absorption with time corresponds to what is expected if the black carbon emission timeseries is comparable to its forcing timeseries. For CCSM3, the residual SW absorption increases until around 2030 as expected, but it does not decrease substantially below the 2000 values, as would be expected from the black carbon forcing timeseries. This could be due to increasing ozone.

SW absorption and precipitation should respond to time-dependent aerosol changes; we test whether they do by comparing timeseries of black carbon forcing, clear-sky atmospheric SW absorption, and precipitation for CM2 and CCSM3 (Figure 2.3). The timeseries are smoothed once with a 1-2-1 weighted average filter (Gonzalez and Woods, 2002) for display purposes. In CM2.0 and CM2.1, precipitation increased slowly and steadily throughout the century, at a rate of $0.15 \text{ W m}^{-2} \text{ dec}^{-1}$. This steady and slow increase is consistent with precipitation increases driven by increasing LW cooling but continuously suppressed by increasing black carbon throughout the century. In CCSM3, precipitation increased slowly at first, though not as slowly as in CM2 ($0.2 \text{ W m}^{-2} \text{ dec}^{-1}$ from 2000-2020), rapidly around mid-century ($0.6 \text{ W m}^{-2} \text{ dec}^{-1}$ from 2030-2070), and slowly again at the end of the century ($0.05 \text{ W m}^{-2} \text{ dec}^{-1}$ from 2080-2100). The changes in rate of increase over the century are consistent

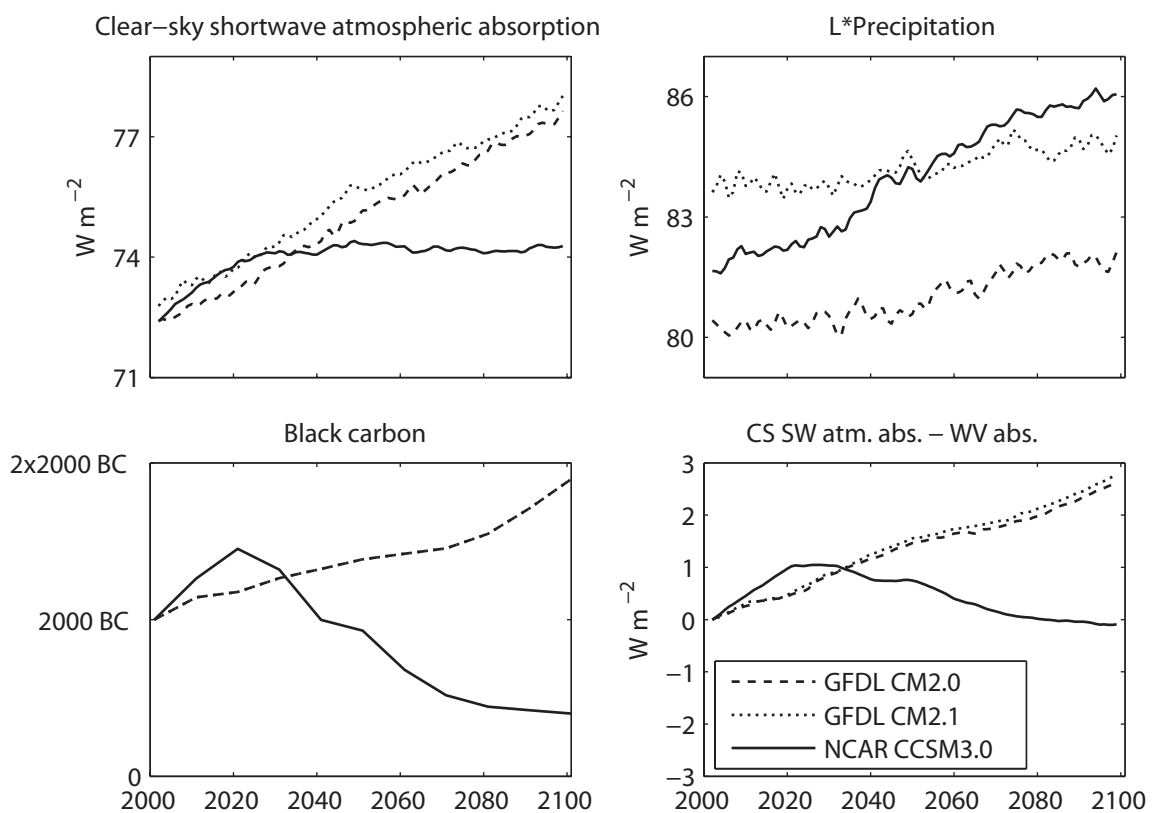


Figure 2.3: Clear-sky SW absorption, clear-sky SW absorption with water vapor contribution removed, precipitation, and black carbon forcing for GFDL CM 2.0, 2.1, and NCAR CCSM 3.0, smoothed once using a 1-2-1 filter (Gonzalez and Woods, 2002). Black carbon forcing is the timeseries of global mean A1b CO (GFDL CM2.0 and CM2.1 black carbon emissions) and SO_x (NCAR CCSM 3.0 black carbon concentrations).

with the initial increase and later decrease in black carbon.

For the atmosphere to maintain energy balance, an increase in SW absorption must be compensated by an increase in LW cooling or a decrease in sensible or latent heating. The precipitation responses in CCSM3 and CM2 are consistent with this expectation. In CCSM3, a large increase in precipitation ($L\Delta P=3.5 \text{ W m}^{-2}$) accompanied the decrease in SW absorption (-1.0 W m^{-2}) by aerosols in CCSM3 (though net increase in SW absorption occurred due to increased water vapor), while in CM2 only modest increases in precipitation (1 W m^{-2}) accompanied the increase in SW absorption by aerosols (1.7 W m^{-2}). Observational estimates of black carbon forcing on atmospheric absorption are much larger than the global-mean of the residuals shown here. Ramanathan and Carmichael (2008) estimate the present-day black carbon forcing of atmospheric absorption to be 2.6 W m^{-2} , and Chung et al. (2005) estimate that it is 3.0 W m^{-2} ; however, these estimates are highly uncertain.

The other models shown in Figure 2.1 and Table 2.1 that incorporated black carbon changes in AR4 simulations are MIROC medres, MIROC hires, and HadGEM3. They fall just in the bottom half of simulations in terms of $L\Delta P/\Delta T$, and they all contain indirect effects of aerosols. Indirect effects are expected to mitigate the direct effects on precipitation by increasing reflection of SW to space via cloud brightening and by decreasing the precipitation efficiency of clouds (Chuang et al., 2002). Both of these indirect effects are a result of the decreased size of cloud droplets that occurs when the number of cloud condensation nuclei increases (see review by Lohmann and Feichter, 2005). However, the indirect effect of black carbon is not expected to be large. The semi-direct effect, which is the decrease in cloud cover due to aerosol heating (Ackerman et al., 2000), is included in all simulations but does not affect the clear-sky radiation.

2.6 Contrast with CO₂-doubling scenario

If differences in absorbing aerosol forcing cause the intermodel spread in $L\Delta P/\Delta T$, scenarios without changes in absorbing aerosols should have less spread in clear-sky atmospheric SW absorption and $L\Delta P/\Delta T$. For the carbon dioxide (CO₂)-doubling scenario, precipitation, surface air temperature, and clear-sky SW upwelling and downwelling radiation at the surface and upwelling at the TOA are obtained from the WCRP CMIP3 database for the same models as above for the “1pctto2x” scenario, except for the Canadian Center for Climate Modeling and Analysis GCM (CCCMA CGCM3.1 T63), which has insufficient data for this scenario. The 1pctto2x scenario is also a transient simulation coupled to a full ocean, so it is the most appropriate scenario to compare to A1b. Differences are taken between decadal averages of years 60-69 and 1-10. Other calculations are the same as for the A1b scenario.

Figure 2.4 shows $L\Delta P/\Delta T$ plotted against clear-sky atmospheric SW absorption per degree change in global-mean surface temperature for CO₂-doubling scenario. There is almost no relationship between clear-sky atmospheric SW absorption change and $L\Delta P/\Delta T$, in stark contrast to the A1b scenario (Figure 2.1). This lack of relationship is consistent with the absorbing aerosol forcing in A1b driving the intermodel spread in precipitation. The range of $L\Delta P/\Delta T$ in the CO₂-doubling scenario is 0.8 W m⁻²K⁻¹, while for A1b the range was 1.5 W m⁻²K⁻¹. The smaller but still substantial range of $L\Delta P/\Delta T$ in the CO₂-doubling scenario indicates that variability in precipitation stems from sources other than absorbing aerosol forcing. This is consistent with clear-sky shortwave atmospheric absorption explaining half of the variance in $L\Delta P/\Delta T$ ($r^2 = 0.61$).

2.7 Conclusions

The IPCC AR4 dataset, and in particular the A1b scenario, have been widely used to study how and why precipitation could change this century. In this study, we compare

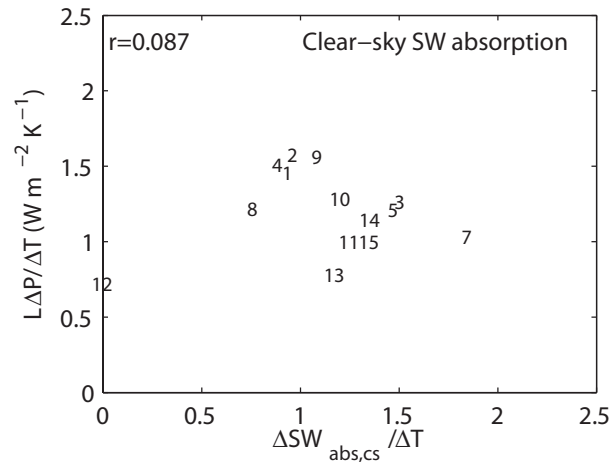


Figure 2.4: Changes in global-mean precipitation and clear-sky atmospheric SW absorption per degree global-mean surface temperature change for CO_2 -doubling experiments. See Table 1 for model key. Changes are calculated between years (60-70) and (0-10). Compare to the top-left panel of Fig. 2.1.

global-mean precipitation change and atmospheric radiation budget components, and we find that clear-sky shortwave absorption is highly correlated with precipitation change. We examine the spatial pattern of clear-sky SW absorption change in NCAR CCSM 3.0 and GFDL CM 2.1, and we find that it resembles the spatial pattern of anthropogenic aerosol emissions, but increases in GFDL CM2.1 and decreases in NCAR CCSM 3.0. We compare timeseries of black carbon forcing from those models with clear-sky atmospheric SW absorption, absorption with the increase due to water vapor increase removed, and precipitation, and find that the timeseries of precipitation change for CCSM3 and CM2 are consistent with the idea that clear-sky shortwave absorption drives precipitation changes, as would be expected from simple radiative-convective equilibrium. Finally, we compare global-mean precipitation and clear-sky atmospheric SW absorption from the CO_2 -doubling scenario, and find that in this scenario precipitation change does not correlate with clear-sky shortwave absorption. This indicates that black carbon forcing differences explain a substantial portion, but

not all, of the intermodel spread in global-mean precipitation in the A1b scenario of AR4. Details of the forcings in AR4, in particular the black carbon forcing, were left unspecified in the emissions scenarios, and forcing data was not available in a coordinated way, which is why this source of spread has gone unappreciated for some time.

Black carbon is short lived, so it is plausible that it could continue to increase throughout the century, or alternatively it could decrease. It is useful to explore a wide range of possibilities including both increases and decreases in black carbon to capture a range of potential future trajectories. Studies making use of A1b projections should take into account the effects that black carbon forcing has on precipitation, including in this dataset. In the future, model intercomparison studies that might be used to investigate precipitation changes should document and report black carbon forcing.

Since this work was undertaken, the CMIP5 model inter-comparison project has been released (Taylor et al., 2012). The black carbon forcing for scenarios including changes in aerosols is documented by Lamarque et al. (2011). In all Representative Concentration Pathway (RCP) scenarios, global-mean black carbon emissions decrease throughout the century. Based on this work, the decreasing black carbon would be expected to lead to decreasing SW absorption and more precipitation increase in the RCP scenarios than if aerosols did not change.

Chapter 3

THE ATMOSPHERIC ENERGY CONSTRAINT ON GLOBAL-MEAN PRECIPITATION CHANGE

In the last chapter, we saw that models disagree on the response of global-mean precipitation in part due to differences in prescribed aerosol forcing. But even in scenarios with carbon dioxide as the only climate forcing, with the same timeseries in each model, there is still substantial disagreement on the response of global-mean precipitation. In this chapter, we focus on the response of atmospheric radiative cooling and precipitation to carbon dioxide forcing.

3.1 Introduction

Climate models robustly predict an increase in global-mean precipitation in response to CO₂ doubling. They agree that the magnitude of this increase will be less than the increase of water vapor concentrations (Held and Soden, 2006). This is true for the multi-model mean, as well as for individual models (though the variation across models is large). The projected rate of increase of global-mean precipitation has long been attributed to the atmospheric energy budget constraint, but the mechanisms and sensitivities of this constraint have yet to be thoroughly explained. In this chapter, we calculate changes in clear-sky atmospheric radiative cooling and relate them to the projected global-mean precipitation change. The relative importance of surface and top-of-atmosphere (TOA) fluxes is illustrated, and the critical importance of downward emission by water vapor is shown. Although the global-mean precipitation change is less important to humans than regional changes, the global constraint affects the regional responses.

Allen and Ingram (2002) popularized the idea that atmospheric energy constrains precipitation on timescales longer than a year. They separated radiative cooling change into two components: one due to a forcing (e.g. CO_2), and another that depends on the change in surface temperature. They used calculations from the GCM experiments in Mitchell et al. (1987) to quantify the magnitude of these two terms, and showed that the atmospheric cooling predicted by this calculation fit the precipitation increase in CMIP2 model experiments.

Since Allen and Ingram (2002), a number of studies have addressed the energetic constraint on precipitation. Takahashi (2009b) developed a radiative-convective equilibrium model which highlighted the interplay between radiative and sensible heat flux, as well as changes in near-surface stability and relative humidity, in determining precipitation change. Lambert and Webb (2008) showed that in an ensemble of GCMs with perturbed physics, the precipitation change due to CO_2 doubling was strongly related to clear-sky atmospheric radiation. Allan (2006) examined observations of clear-sky radiative cooling. Stephens and Ellis (2008) examined changes in precipitation due to transient CO_2 increase in AR4 models. They calculated atmospheric radiation from an empirical relationship with column water vapor, preventing the separation of responses to warming and moistening. Previdi (2010) calculated the atmospheric radiative responses to AR4 GCM warming and moistening using feedback kernels. We aim to build upon these studies by providing a simple and understandable account of clear-sky atmospheric cooling response to warming and moistening.

This chapter will proceed as follows. First, we present the change in global-mean precipitation in CMIP5 transient CO_2 -increase experiments. Then, we show the effect of changes in temperature and moisture at varying heights in the atmosphere using radiative feedback kernels. This illustrates that the radiative response to moistening depends on the height at which it occurs. Next, we construct a framework for the global-mean atmospheric radiative energy balance. This framework consists of the atmospheric cooling response to idealized changes in temperature, moisture, and CO_2

forcing. The atmospheric radiative cooling calculations allow us to attribute the changes in clear-sky radiative fluxes seen in GCMs to the structure of changes in temperature, water vapor, and CO₂. We compare the sum of these changes to the clear-sky fluxes in the CMIP5 multi-model mean to ensure fidelity of our framework, and reconcile the framework with CMIP5 precipitation changes. Finally, we examine the inter-model spread in the rate of precipitation increase across models. In the last section, we discuss the role of clouds, aerosol forcing, and the surface perspective on precipitation change.

3.2 Atmospheric energy and precipitation change

The rate of global-mean precipitation increase in transient CO₂ increase experiments (1pctCO2, Taylor et al., 2012) is shown in Figure 3.1 for each of the CMIP5 models used throughout this chapter. These models are listed in Table A.1. Only models with available precipitation, total-sky and clear-sky radiation at the surface and TOA, and atmospheric and near-surface air temperature and moisture fields are used, and only one ensemble member from each model is included. Time differences are taken between years 1-10 and years 61-70 of the experiments (year 70 is the time of CO₂ doubling). For each model, the precipitation change is normalized by the change in global-mean surface air temperature.

All models show an increase in precipitation, though the variation in magnitude across models is large. The multi-model mean precipitation increase is $1.1 \text{ W m}^{-2} \text{ K}^{-1}$, which corresponds to 1.4% of the multi-model, global-mean precipitation. This is much less than the rate of increase of water vapor, about $7\% \text{ K}^{-1}$, which would correspond to $6 \text{ W m}^{-2} \text{ K}^{-1}$ of precipitation increase. The change in multi-model, global-mean precipitation and other energy fluxes of interest are listed in Table 3.1.

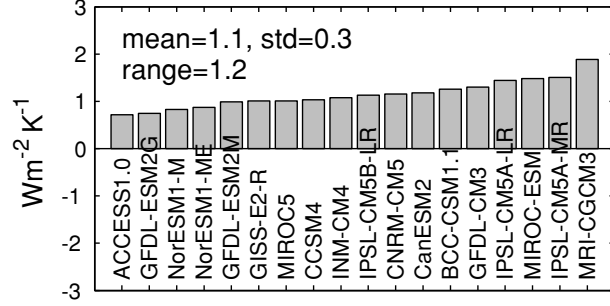


Figure 3.1: Global-mean precipitation sensitivity in CMIP5 models ($W m^{-2} K^{-1}$), estimated from the difference between first 10 years and years 61-70 in the transient CO_2 increase scenario.

Table 3.1: CMIP5 multi-model, global-mean change (Δ) in energy components for transient CO_2 increase ($W m^{-2} K^{-1}$) calculated directly from GCMs. Positive signs correspond to increasing precipitation. T is the surface air temperature, LP is precipitation times the latent heat of vaporization of water, SH is sensible heat flux, R_{atm} is atmospheric radiative cooling, cs indicates clear-sky, $cloud$ indicates cloudy-sky, and R_{TOA} is the TOA outgoing radiative response.

$L\Delta P/\Delta T$	1.1
$\Delta SH/\Delta T$	0.3
$\Delta R_{atm,cs}/\Delta T$	1.2
$\Delta R_{atm,cloud}/\Delta T$	-0.4
$\Delta R_{atm}/\Delta T$	0.8
$\Delta R_{TOA}/\Delta T$	-0.7

3.3 Radiative response to changes in moisture and temperature at a particular height

Since the energy constraint on precipitation is fundamentally radiative, it can be explored in a simple radiative context. In this section,¹ we illustrate the importance of the height at which moisture and temperature perturbations occur on the atmospheric radiative cooling response with qualitative calculations using the radiative kernel technique. We calculate the atmospheric column radiative response to temperature and moisture changes from the CMIP5 multi-model mean in order to determine the height at which changes in moisture and temperature are important. We calculate multi-model mean changes in air temperature, specific humidity, and surface temperature for the same experiments and time period as in the previous sections. The temperature and moisture changes for each model are normalized by the model's change in global-mean surface air temperature before averaging across models.

The CMIP5 multi-model mean temperature and moisture responses to CO₂ increase are shown in Figure 3.2. The top panel shows the warming. The warming is amplified with height, up to a maximum of about 2 K near 200 hPa across the tropics. Amplification decreases poleward. The bottom panel shows the percent increase in specific humidity. The change in specific humidity reflects this amplified warming and the dependence of saturation vapor pressure on the temperature. The overall effect is that the specific humidity increase (in percent) is highest at the equator and decreases poleward. It also increases from the surface up to 200 hPa. RH changes are small, changing by up to 2%.

Now we would like to calculate the response of atmospheric column radiative heating to these temperature and moisture changes, broken down by latitude and height. We can accomplish this by applying radiative feedback kernels for the atmospheric column to the model-projected changes in temperature and moisture. The radiative

¹This section was not included in the published version of the paper.

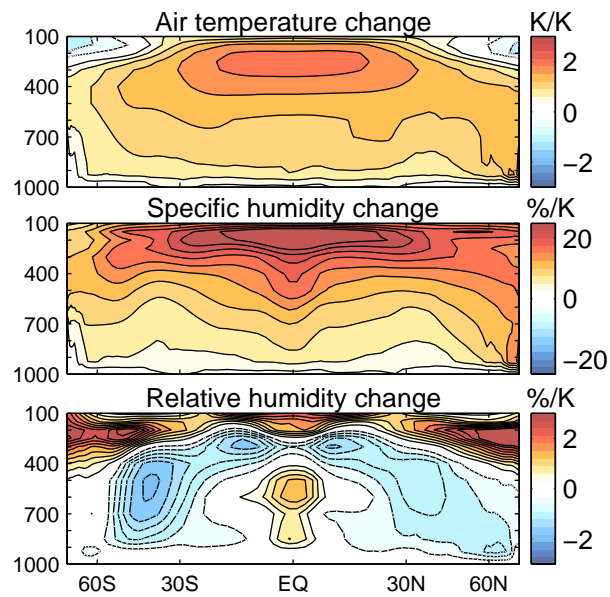


Figure 3.2: CMIP5 multi-model mean changes associated with 1 K global surface warming caused by transient CO_2 increase. Change in temperature (K K^{-1}) is on top, change in specific humidity ($\% \text{K}^{-1}$) is at center, and change in relative humidity is on bottom ($\% \text{K}^{-1}$). The horizontal axis is sine of latitude, so that equal distances represent equal areas of Earth's surface.

kernel technique was presented in Soden and Held (2006). Kernels were adapted for atmospheric radiative cooling in Previdi (2010). Here, we use total-sky kernels calculated in the GFDL CM2.0 model (which were calculated by Brian Soden).

The kernels are calculated by integrating a GCM for a year, and a few times each model-day re-running the radiation code offline, perturbing the temperature at each latitude, longitude, and height by 1 K, and saving the change in TOA and surface radiative flux due to each perturbation. Specific humidity is perturbed separately by the constant-RH moistening that would occur for 1 K warming. The monthly mean is taken, then the atmospheric column radiative response is calculated, so that we have the change in atmospheric column radiation due to 1 K warming or moistening at each latitude, longitude, and height for each month of the year. We interpolate model-projected changes onto the kernel grid, then multiply the kernels by the GCM changes in temperature and moisture. We present this calculation as a qualitative picture of where (vertically) moisture and temperature changes are important. These kernels are not quantitatively accurate because of topography and other issues with the surface layer. This calculation does not account for CO₂ forcing. Masking by clouds is included in the kernel calculation, so the effect of clouds in the mean state is accounted for but changes in clouds with warming are not.

As in our idealized calculations in Section 3.4, the atmospheric column changes are the sum of TOA and surface changes. All three are shown in Figure 3.3. The top panel shows the TOA radiative response to the multi-model mean temperature and moisture change. It is weak but positive (increased outgoing radiation to space, inducing cooling of the planet). The middle panel shows the surface radiative response. It is overwhelmingly dominated by the lower-tropospheric contributions. It is positive, indicating increases of surface downwelling radiation. The bottom panel shows the atmospheric column response. It is just the sum of the first two panels. It is positive, indicating increased atmospheric radiative cooling, via both increased upwelling radiation at the TOA and increased downwelling radiation at the surface. Signs are

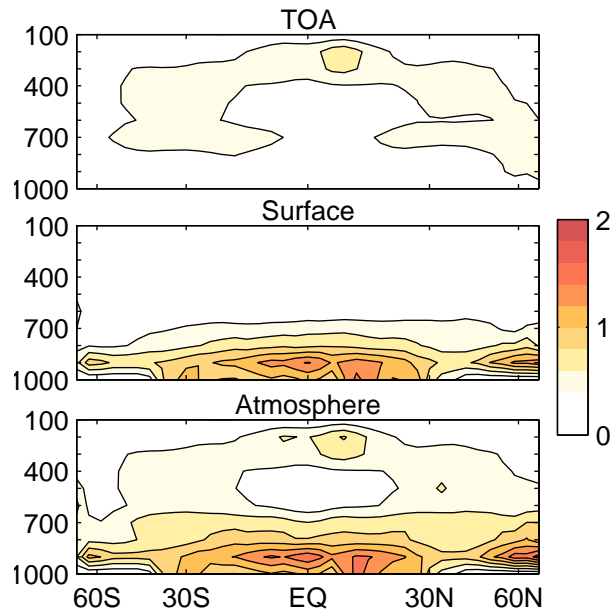


Figure 3.3: Radiative response ($\text{W m}^{-2} \text{K}^{-1} [100 \text{ hPa}]^{-1}$) at the TOA (top) and surface (middle), and atmospheric radiative cooling change (bottom), shown as functions of latitude and pressure.

chosen so that positive indicates increased atmospheric cooling and precipitation.

LW atmospheric column responses to temperature and water vapor changes are shown in Figure 3.4. The top panel shows the LW response to warming of the atmosphere with surface temperature fixed. The maximum increase in cooling coincides roughly with the upper-tropospheric amplification of warming. Increased emission to the surface due to warming at low levels is also evident.

The bottom panel shows the LW response to increased moisture. It has two lobes: increased emission to the surface from low-level moistening, especially in the tropics, and decreased OLR due to upper-tropospheric moistening. These TOA and surface responses partially cancel, as we will see in Section 3.4. The SW response to increased moisture is absorption increase (equivalently, cooling decrease) due to moistening below 600 hPa, mostly in the tropics but also in northern mid-high latitudes, which mitigates the lower tropospheric cooling increase due to LW changes.

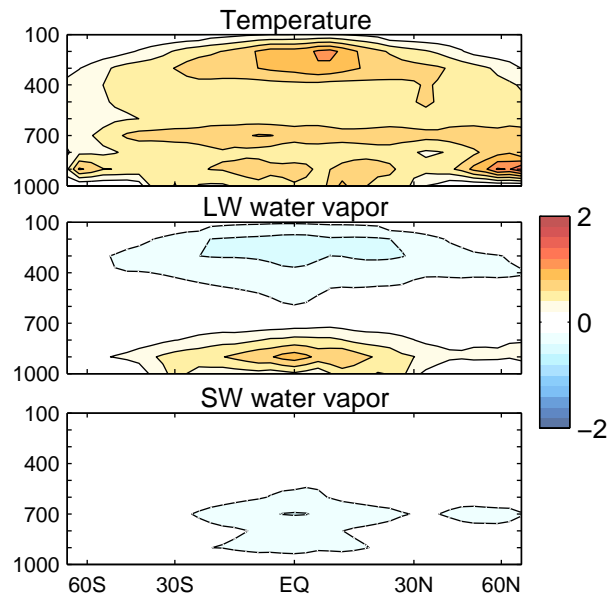


Figure 3.4: Atmospheric column radiative responses ($\text{W m}^{-2} \text{K}^{-1} [100 \text{ hPa}]^{-1}$), with LW response to temperature change on top, LW response to specific humidity change in the center, and SW response to specific humidity change in the center on bottom. Negative values are enclosed by dashed contour lines.

In the next section, we examine changes in atmospheric cooling, which we will later reconcile with the multi-model mean precipitation increase.

3.4 Atmospheric column radiative responses to idealized changes in temperature, moisture, and CO₂

3.4.1 Clear-sky radiative column calculations

In this section, we calculate the atmospheric column radiative response to idealized changes in temperature, moisture, and CO₂ increase. For baseline calculations, we use annual mean profiles of temperature and specific humidity at each point on the globe from the CMIP5 multi-model mean for the first ten years of the transient CO₂ increase experiment (global mean shown in Figure 3.5). The multi-model mean is interpolated onto a common grid with 90 latitude and 144 longitude points. Archived CMIP5 model fields share a common pressure grid with 17 vertical pressure levels, though at many locations some of these levels are below the surface. At each location, our calculations include all standard levels that are above the multi-model, annual mean surface pressure. We also specify the bottom atmospheric level to be at the surface pressure and surface air temperature, with surface air specific humidity. We use CMIP5 multi-model mean ozone profiles (though only six of the models have archived ozone). For the surface layer, we set ozone the same as the level above it. We calculate radiative fluxes with the Fu and Liou (1992) column radiation model. To have meaningful shortwave (SW) components, we use the zonal, annual mean insolation-weighted solar zenith angle. Clouds are not included.

From this baseline radiative calculation, we incrementally vary temperature, moisture and CO₂. We will consider them in turn, but the resulting atmospheric radiative responses are shown in Table 3.2. The sign is chosen so that an increase in atmospheric radiation corresponds to an increase in precipitation; that is, a positive change means more cooling. Since the atmospheric column response is the sum of the familiar TOA response and the surface response, the table also includes the TOA and surface

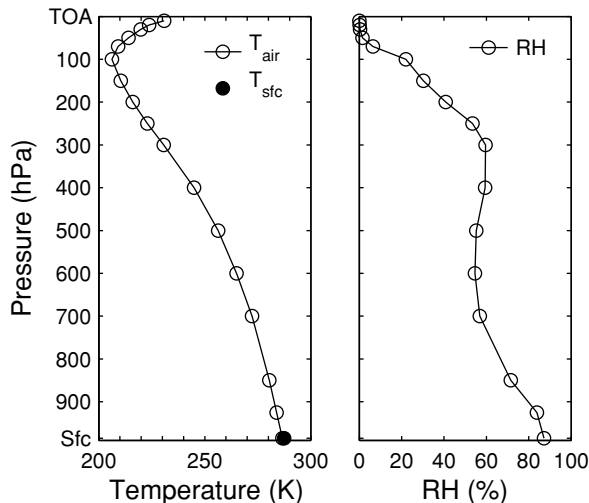


Figure 3.5: Global mean of the CMIP5 multi-model mean temperature and RH profiles used as the baseline for column radiation calculations.

responses.

We begin with an increase of atmospheric temperature by 1 K at all levels in the troposphere. The tropopause is defined as 100 hPa at the Equator, 300 hPa at the Poles, and linearly interpolated in between. In the first line of Table 3.2, we see that atmospheric warming results in an increase in atmospheric longwave (LW) cooling of $5.6 \text{ W m}^{-2} \text{ K}^{-1}$. Somewhat less than half of this cooling leaves from the TOA, and somewhat more than half is emitted toward the surface. This is an expected consequence of increasing the temperature of the atmosphere. The noteworthy aspect of this calculation is that the downward emission from the atmosphere to the surface is large, even larger than the change at the TOA.

In the second calculation (line 2 of Table 3.2), the atmosphere is returned to its baseline profile and the surface temperature is increased by 1 K. This results in an increase in LW emission from the surface of $5.0 \text{ W m}^{-2} \text{ K}^{-1}$. Twenty-four percent of this radiation ($1.2 \text{ W m}^{-2} \text{ K}^{-1}$) escapes to space through the TOA, and the rest

Table 3.2: Global-mean clear-sky radiative response to various temperature, moisture, and CO₂ changes at the TOA, surface, and in the atmospheric column (W m⁻² K⁻¹) calculated with Fu and Liou (1992) column radiation code. Signs are chosen so that a positive response contributes to increasing precipitation: increased cooling is positive for the atmospheric column, upwelling is positive at the TOA, and downwelling is positive at the surface. Note that the atmospheric cooling is the sum of net downwelling surface radiative flux and net upwelling TOA radiative flux, $ATM = SFC + TOA$. The two values of net change in clear-sky atmospheric radiative cooling are bolded.

	Description	Response		
		TOA	SFC	ATM
1	Vertically-uniform T_a	2.3	3.3	5.6
2	T_s	1.2	-5.0	-3.8
3	Vertically-uniform warming	3.4	-1.7	1.8
4	LW fixed RH q	-1.7	3.4	1.7
5	Vertically-uniform T , fixed RH, LW	1.8	1.7	3.4
6	SW fixed RH q , fixed RH	-0.1	-0.9	-1.0
7	Vertically-uniform Net	1.7	0.8	2.5
8	Vertically-varying T , idealized	0.7	-0.1	0.6
9	Vertically-varying T , fixed RH q	0.0	-0.1	-0.1
10	Cumulative net	1.7	0.7	2.4
11	Transient CO ₂	-2.0	0.9	-1.1
12	Net idealized response	-0.3	1.5	1.2
13	Vertically-varying T , CMIP5	0.7	0.1	0.9
14	Vertically-varying T , fixed RH q	0.1	0.3	0.3
15	Cumulative net	1.8	1.0	2.8
16	Transient CO ₂	-2.0	0.6	-1.4
17	Net CMIP5 response	-0.3	1.6	1.3
18	ΔRH	0.1	-0.1	-0.0

is absorbed by the atmosphere. This is in agreement with a recent calculation of the fraction of surface emission emitted to space by Costa and Shine (2012), who calculated clear-sky transmission of 25%, though this is reduced to about 10% when clouds are included.

Typical warming includes changes in both the surface and the atmosphere. The third calculation is uniform warming of the surface and each atmospheric level by 1 K, which we refer to as “uniform” warming. Responses are listed in the third line of Table 3.2; Figure 3.6 (left panel, solid line with filled circles) shows the change in net upwelling radiation at the surface, each level in the atmosphere, and the TOA due to the warming. The change in surface emission is higher than the change in downward atmospheric emission because the surface temperature is higher than the temperature at the effective atmospheric downward emission level. The overall effect of uniform warming is LW cooling of the atmosphere by $1.8 \text{ W m}^{-2} \text{ K}^{-1}$. Nearly double this amount of LW is lost from the TOA, but increased heating of the atmosphere by surface LW emission mitigates the TOA loss. Note the linearity of the temperature changes: the response to uniform warming differs from the sum of responses to warming the surface and atmosphere separately by just $0.1 \text{ W m}^{-2} \text{ K}^{-1}$.

Next we vary the moisture. First, the moisture is increased by the amount that would maintain constant relative humidity (RH) during a 1 K uniform warming, but the atmosphere and surface temperatures are maintained at their baseline values. The LW responses are tabulated in the fourth line of Table 3.2 and shown in Figure 3.6 (left panel, short-dashed line with open circles). At the surface, downward emission from the atmosphere increases by $3.4 \text{ W m}^{-2} \text{ K}^{-1}$ as the increased water vapor lowers the effective height of emission to a warmer level. At the TOA, $1.7 \text{ W m}^{-2} \text{ K}^{-1}$ less LW is lost to space as the level of emission is raised to a cooler level. The overall LW atmospheric response to this moistening is $1.7 \text{ W m}^{-2} \text{ K}^{-1}$, an increase very similar in magnitude to the uniform warming increase. So the increase in humidity increases the radiative cooling of the atmosphere through increased downward emission to the

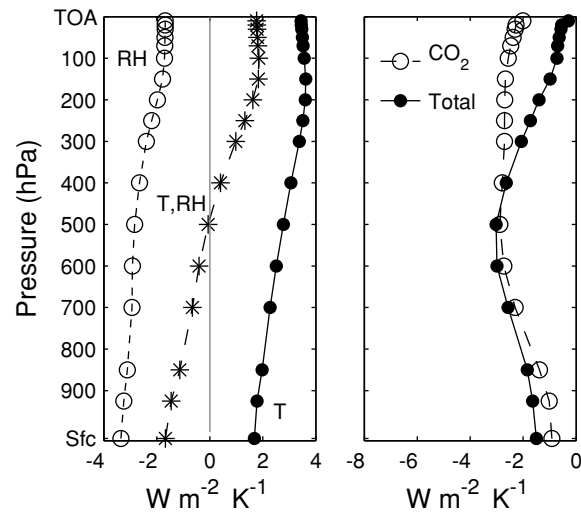


Figure 3.6: Net upwelling radiative response ($\text{W m}^{-2} \text{K}^{-1}$). On the left are the LW responses to air and surface temperature increase of 1 K (filled circles), constant RH moisture increase (open circles), and combined temperature and moisture increase (asterisks). On the right are net upwelling radiative responses to CO_2 forcing (open circles) and warming, moistening, and CO_2 forcing combined (solid circles).

surface. We infer from this that the precipitation rate in equilibrium is sensitive to the vertical distribution of humidity. As we saw in Section 3.3, increased humidity in the lower troposphere contributes to increases in precipitation, while increased humidity in the upper troposphere contributes to decreases in precipitation. The wavelengths of water vapor continuum absorption are most important in determining surface emission, while upper tropospheric emission is determined by the wavelengths of rotation and vibrational bands (Mitchell et al., 1987; Inamdar et al., 2004).

The fifth line of Table 3.2 lists the LW response to uniform increase in temperature along with moistening at constant RH; this is also shown in Figure 3.6 (left panel, long-dashed line with asterisks). Atmospheric cooling is increased by $3.4 \text{ W m}^{-2} \text{ K}^{-1}$, with the largest contributions coming from an increase in outgoing LW at the TOA (OLR) due to warming and an increase in LW emission to the surface due to moistening. In contrast, uniform warming decreases emission to the surface and moistening decreases cooling to space.

We next take SW changes into account, which come into play because water vapor absorbs SW radiation. Line 6 of Table 3.2 shows the change in SW absorption due to constant-RH moistening for 1 K warming. SW absorption offsets the increased LW cooling by $1.0 \text{ W m}^{-2} \text{ K}^{-1}$. Line 7 of Table 3.2 lists the net response to the uniform warming with constant RH moistening. The net effect of uniform warming and constant RH moistening is an increase in atmospheric radiative cooling of $2.5 \text{ W m}^{-2} \text{ K}^{-1}$.

Models and theory predict that warming is amplified with height, rather than vertically uniform. To incorporate the variation of warming with height, we calculate the difference between moist adiabats starting from the initial and warmed surface air temperature. The OLR response to the variation in warming with height is the lapse rate feedback.

Lines 8-10 of Table 3.2 show the response to vertical variations in warming with height (minus the response to uniform warming); this is also shown in Fig. 3.7.

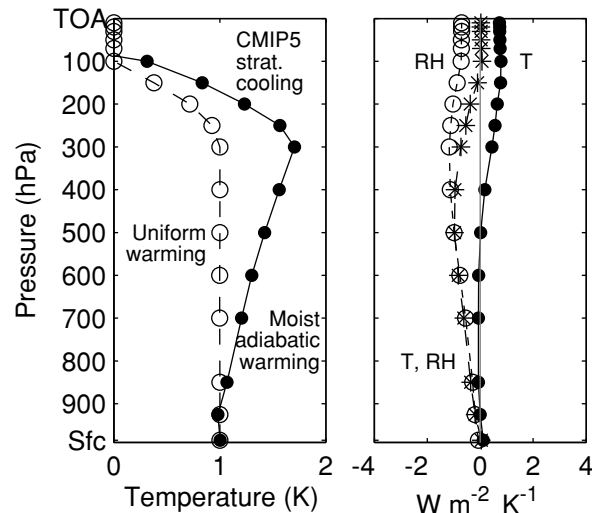


Figure 3.7: Amplification of warming with height is shown at left, with global-mean vertical temperature increase for uniform warming (open circles) and warming amplified with height (the difference between moist adiabats, filled circles). On the right is the LW upwelling radiative response ($W m^{-2} K^{-1}$) to amplified warming with height, with temperature increase alone (filled circles), constant-RH moistening alone (open circles), and warming and moistening together (asterisks).

Amplified warming with height enhances atmospheric cooling by $0.6 W m^{-2} K^{-1}$, mostly by increasing cooling to space from the warmer upper troposphere; but, there is also $0.1 W m^{-2} K^{-1}$ of decreased cooling to the surface. Constant-RH moistening mitigates the OLR increase to just $-0.1 W m^{-2} K^{-1}$. Using the CMIP5 multi-model mean change in warming with height instead of the moist adiabatic approximation (lines 13-15 of Table 3.2) gives a change that is slightly larger, with $0.3 W m^{-2} K^{-1}$ more increase in atmospheric cooling.

So far we have considered uniform and vertically-amplified warming, and moistening at constant RH. Now we must account for the radiative effect of the CO_2 forcing. We choose an initial CO_2 concentration corresponding to the mean of the first 10 years, 297.9 ppm, and a final concentration corresponding to the mean of years 61-70,

541.2 ppm. We incorporate stratospheric cooling due to the CO₂ forcing by using CMIP5 multi-model mean stratospheric temperatures. The mean temperature from years 61-70 is applied at all levels above the tropopause, which we define as a linear interpolation between 100 hPa at the equator and 300 hPa at the poles (following Soden and Held 2006; Previdi 2010). The response to CO₂ forcing is listed on line 11 of Table 3.2 and shown in Figure 3.6 (right panel, dashed line with open circles). The CO₂ increase reduces cooling from the TOA by 2.0 W m⁻² K⁻¹, and also increases cooling to the surface by 0.9 W m⁻² K⁻¹. The overall effect is a reduction of atmospheric cooling by 1.1 W m⁻² K⁻¹.

Combining the CO₂ forcing and responses to uniform and amplified warming and constant-RH moistening, we obtain 1.2 W m⁻² K⁻¹ of increased atmospheric cooling calculated from our radiative transfer model. This is the same as the clear-sky atmospheric cooling change in the CMIP5 multi-model mean. We will return to this result and compare it with CMIP5 precipitation change in Section 3.6.

The calculations in this section connect a set of simple, easily understandable changes in temperature and moisture to changes in atmospheric radiative cooling. Using these annual-mean, clear-sky profiles, we get reasonably close to CMIP5 precipitation change. Furthermore, they show how TOA radiative responses relate to the radiative response in the atmospheric column.

In the remaining lines of Table 3.2, we repeat lines 8-12 using the CMIP5 multi-model mean change in temperature with height, instead of the moist adiabatic warming. The net atmospheric cooling response differs by 0.1 W m⁻² K⁻¹, while individual components vary by up to 0.3 W m⁻² K⁻¹.

Additionally, we calculated the radiative effect of the CMIP5 multi-model mean change in RH, shown in line 18 of Table 3.2. The change in RH is determined from the model changes in specific humidity, in contrast to the assumption of constant RH we use in the rest of the calculations. RH in the lowest layer of the atmosphere increases slightly over ocean, by less than 2 % K⁻¹, while it decreases over land, typically by

about 2 % K^{-1} . The change in RH results in a decrease of $0.1 \text{ W m}^{-2} K^{-1}$ of net downwelling radiation to the surface because the decreasing near-surface RH over land dominates the increasing RH over ocean in the global mean. The decrease in emission to the surface is compensated by an increase in OLR of $0.1 \text{ W m}^{-2} K^{-1}$, so there is no net change in atmospheric cooling.

Previdi (2010) made similar calculations using the radiative feedback kernel technique. He found that the LW atmospheric cooling response to increased water vapor is a decrease in atmospheric cooling, dominated by the upper and middle tropospheric moistening. We find just the opposite, an increase in atmospheric LW cooling due to increased water vapor. Using the same clear-sky water vapor feedback kernels as that study with the multi-model mean moistening here, the change in atmospheric LW cooling is $-0.7 \text{ W m}^{-2} K^{-1}$, as compared to $1.1 \text{ W m}^{-2} K^{-1}$ calculated with Fu and Liou (1992) code. This direct comparison is with the same temperature and humidity profile, so the difference is due to the methodology or radiative transfer code. We think our calculation is accurate because we recover the change in clear-sky atmospheric radiative cooling from GCMs. Additionally, our finding that moistening increases atmospheric LW cooling is in agreement with variability seen in satellite and reanalysis data (Allan, 2006).

3.4.2 Consistency of radiative column calculations and GCM fluxes

The calculations above show that the dominant mode of temperature and moisture change for setting the atmospheric radiative cooling response is the vertically uniform warming with fixed RH moistening. Now we are in a position to reconcile the magnitude of atmospheric radiative cooling response in our framework with global-mean precipitation change projected by CMIP5 models. Returning to line 12 of Table 3.2, we would expect to see $1.2 \text{ W m}^{-2} K^{-1}$ of precipitation change for the transient CO_2 response. We can compare this to the tabulated multi-model, global-mean changes in precipitation as well as atmospheric cooling listed in Table 3.1. Our calculation agrees

Table 3.3: Comparison of clear-sky radiative fluxes calculated with Fu and Liou (1992) column radiation code and CMIP5 multi-model mean radiative fluxes ($\text{W m}^{-2} \text{K}^{-1}$).

	Fu-Liou (moist adiabat)	Fu-Liou (CMIP5 fields)	CMIP5
Atm Net	1.2	1.3	1.2
LW	2.3	2.4	2.4
SW	-1.1	-1.1	-1.2
TOA LW	-0.2	-0.2	-0.3
Surface LW	2.5	2.6	2.6

with the CMIP5 multi-model mean clear-sky atmospheric radiative cooling change of $1.2 \text{ W m}^{-2} \text{K}^{-1}$. The alternative calculation using CMIP5 patterns of change (line 17 of Table 3.2) agrees to within $0.1 \text{ W m}^{-2} \text{K}^{-1}$.

We can also compare the clear-sky LW and SW radiative flux changes from the CMIP5 multi-model mean with our calculations. Table 3.3 shows this comparison. For atmospheric column cooling, the radiative column calculations agree with the CMIP5 multi-model mean to within $0.1 \text{ W m}^{-2} \text{K}^{-1}$. For the TOA and surface, only LW comparison is shown. We expect the SW to differ because we have not incorporated changes in the surface albedo, especially sea ice; but this should not affect the atmospheric column much. At the TOA and surface, our values agree to within $0.1 \text{ W m}^{-2} \text{K}^{-1}$.

While the effect of clouds on atmospheric radiation cannot be obtained in our framework, we can consider how clouds influence the atmospheric cooling rate calculated by the GCMs. We will do this in Section 3.6.1.

3.4.3 Radiative column calculations of idealized clouds

Clouds play an undeniable role in the atmospheric energy budget. Figure 3.8 shows a column radiation calculation with two idealized clouds: a low cloud and a high cloud.

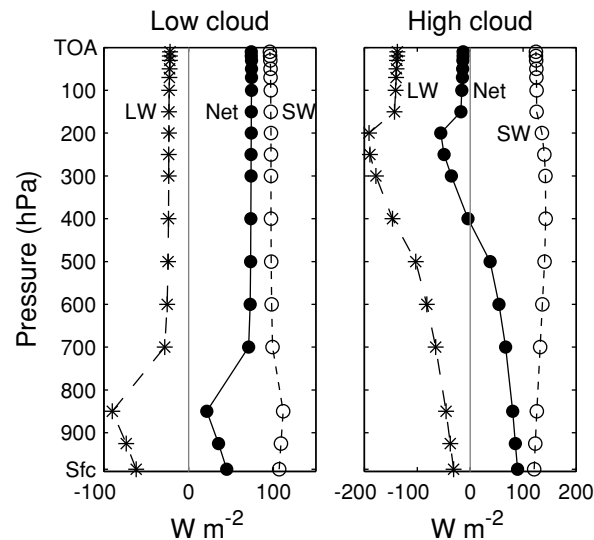


Figure 3.8: Upwelling radiative response (W m^{-2}) to idealized clouds, with low cloud at left and high cloud at right. LW is shown with asterisks, SW with open circles, and net with filled circles. Both clouds have liquid water path of 40 g m^{-2} and effective radius $14 \mu\text{m}$.

We use global-mean profiles of temperature, moisture, and ozone for this calculation. Each cloud has a liquid water path of 40 g m^{-2} and effective droplet radii of $14 \mu\text{m}$. The low cloud occupies one pressure layer, from about 1.5 to 3 km. The high cloud occupies multiple layers, from 5.5 to 12 km. The liquid water is spread evenly across the layers. Ice is not considered. The clouds have SW optical depth of 0.5. The radiative responses to these clouds are listed in Table 3.4.

Here we encounter one of the great advantages of the atmospheric energy budget perspective over the surface perspective: reflection of SW by clouds has little effect on the atmospheric energy budget. There is a modest change in SW absorption when clouds are present, but this is far overwhelmed by the clouds' effects in the LW.

Consider the low cloud (left panel, Figure 3.8). The low cloud has a LW emissivity near 1, causing the LW emission to the surface to come from a warmer temperature

Table 3.4: Radiative response (W m^{-2}) to idealized clouds. As in previous tables, signs are chosen so that increased atmospheric cooling is positive.

	TOA	SFC	ATM
Low cloud LW	-22	62	40
SW	96	-107	-11
Net	74	-45	29
High cloud LW	-137	31	-106
SW	124	-121	3
Net	-13	-89	-103

than it would in clear skies. This enhances atmospheric cooling to the surface. The cloud also intercepts LW emitted from the surface that would otherwise escape to space, decreasing the OLR and mitigating the increase in atmospheric cooling. The temperature difference between the surface and cloud top is relatively small, so that the increased emission to the surface dominates over the reduced OLR. Overall, the low cloud increases atmospheric cooling by 29 W m^{-2} .

The high cloud changes surface LW by only a small amount, by emitting some LW downward from its base (right panel, Fig. 3.8). It has a much larger effect on the OLR. The cloud traps the LW emitted by the surface and warmer parts of the atmosphere, re-emitting radiation from its cold top. The overall effect is strong atmospheric heating, with a magnitude of 103 W m^{-2} . The high cloud suppresses precipitation very strongly.

Clouds also affect radiation at the surface. In Figure 3.8, the effect of the cloud on surface energy is the absolute difference at the bottom of the panel (the effect on the atmosphere is the slope of the line between the surface and TOA). Unlike for the atmospheric column, both low and high clouds have a large effect on the surface SW, of about 100 W m^{-2} . For the low cloud, the reduction in SW is mitigated by an increase in absorbed LW. There is less mitigation for the high cloud.

3.5 *Inter-model spread in atmospheric radiative cooling response to CO₂ forcing*

In the previous section, we carefully examined the CMIP5 multi-model mean atmospheric cooling response to increasing CO₂ in order to understand the change in multi-model mean precipitation. Can we also understand the differences in the rate of precipitation increase across models? The range of climate response across models is often used to explore mechanisms for climate change. Previous studies have explored the inter-model spread in precipitation change due to climate forcing. Takahashi (2009a) examined the precipitation response in CMIP3 slab-ocean experiments forced by a doubling of CO₂. Previdi (2010), Chapter 2 and others examined precipitation change in the realistic A1b forcing scenario in CMIP3, which included changes in aerosol forcing, and found that the difference in aerosol forcing dominates the inter-model spread. Here we consider the inter-model spread in precipitation response to the CO₂ forcing alone.

Precipitation increase varies across the 18 models by a factor of two (Fig. 3.1). Change in precipitation is balanced by the sum of changes in sensible heat flux, cloud radiative forcing, and clear-sky atmospheric radiative cooling. Cloud radiative forcing change has a range of 1.2 W m⁻² K⁻¹ across models. Precipitation change is closely tied to the change in clear-sky radiative cooling alone in most models (Fig. 3.9). Omitting two outlier models, the correlation between precipitation change and clear-sky atmospheric radiative cooling is 0.91. The strong relationship of $\Delta R_{cs}/\Delta T$ to $\Delta P/\Delta T$ indicates that much of the inter-model spread in precipitation can be understood from changes in clear-sky atmospheric radiative cooling.

We calculate the clear-sky radiative cooling response to each model's pattern of warming and moistening, using the same procedure as in Section 3.4. When compared to fluxes directly output from the GCMs, our calculations do a tolerable job at recovering the response of clear-sky LW atmospheric cooling (per degree global-mean

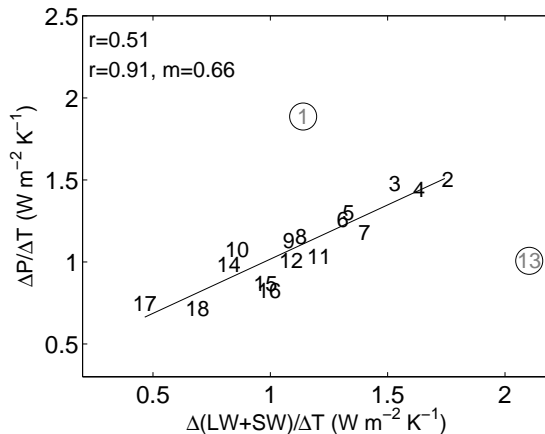


Figure 3.9: Change in clear-sky atmospheric radiative cooling (from model-output radiative fluxes) versus change in global-mean precipitation increase, normalized by global-mean surface temperature change for each CMIP5 model. Correlation is calculated with and without two outlier models, GISS E2-R and MRI CGCM3; slope is calculated without the outliers.

surface temperature increase) calculated by the models ($r=0.77$, slope=0.6), but they do a poor job capturing the change in clear-sky SW absorption (Fig. 3.10). The calculated change in the multi-model mean matches quite closely, but there is very little spread in the SW absorption in our calculation, despite a range of $0.9 \text{ W m}^{-2} \text{K}^{-1}$ in the GCM-calculated response. This suggests that much of the difference is due to different methods of computing SW heating in the CMIP5 models. Collins et al. (2006) compared GCM clear-sky radiative transfer calculations and found large differences in both SW and LW across models. Takahashi (2009a) also found differences in SW absorption between models in CMIP3. Their analysis suggested that the scatter in clear-sky SW absorption might be due to the spatial pattern of water vapor changes, but this is accounted for in our calculation and does not replicate the spread. For the remainder of this analysis we focus on the change in clear-sky LW atmospheric cooling.

It is well-known that the lapse rate and water vapor feedbacks compensate each

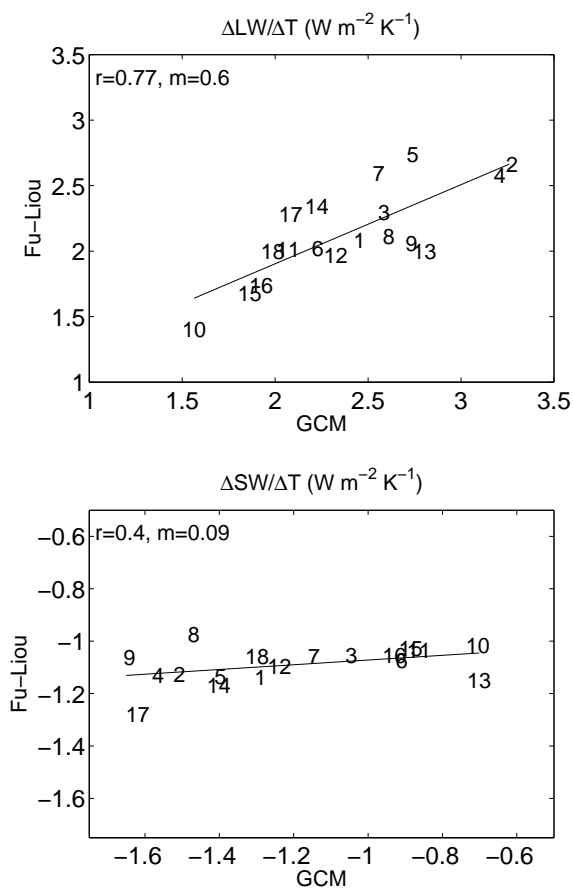


Figure 3.10: Clear-sky atmospheric cooling change calculated from CMIP5 model output (GCM) and Fu and Liou (1992) column radiation code, using each model's change in temperature and moisture. Changes in clear-sky LW cooling (top) and SW absorption (bottom) normalized by global-mean surface temperature change.

other at the TOA (e.g. Cess 1975; Zhang et al. 1994; Soden and Held 2006; Held and Shell 2012). Figure 3.11 shows our calculation of inter-model spread in the LW response to lapse rate and water vapor changes, and their sum, for each model, at the TOA and for the atmospheric column. At the TOA, the response to lapse rate and water vapor have similar spread but opposite sign. Their sum has a smaller spread than either individually. The total spread in TOA radiation is bigger than the sum of these two effects, indicating that other feedbacks also play an important role. Consistent with this compensation, the lapse rate and water vapor feedback are strongly anti-correlated ($r=-0.91$) with similar magnitudes of variation across models (slope $m=-0.76$, Fig. 3.12). If the responses scale across models as they do in the multi-model mean, then we can understand these responses from the calculations reported in on lines 8 and 9 (or 14 and 15), of Table 3.2. At the TOA, the response to changing lapse rate is comparable in magnitude and opposite in sign to the accompanying constant-RH moistening. There is also a contribution to the water vapor feedback from the moistening accompanying vertically-uniform warming.

For the atmospheric cooling (Fig. 3.11), the story is different from the TOA. The atmospheric cooling response to changes in lapse rate and water vapor have the same sign. The range of the sum of their responses has a magnitude similar to the response to lapse rate change alone. The range in the total clear-sky atmospheric radiative cooling is similar to the sum of these two effects, and to the change in precipitation. The relationship between the responses to moistening and changes in lapse rate has a weaker correlation ($r=-0.68$) and the variation across models in the magnitude of the response to changing lapse rate is twice as large as water vapor (slope $m=-2.1$).

Why don't the responses to changing lapse rate and water vapor compensate for the atmospheric cooling? As for the TOA response, we can understand this in light of the calculations documented in Table 3.2. The response of atmospheric cooling to changes in lapse rate and the accompanying constant-RH moistening do compensate (Fig. 3.13); models with larger responses to changing lapse rate have smaller responses

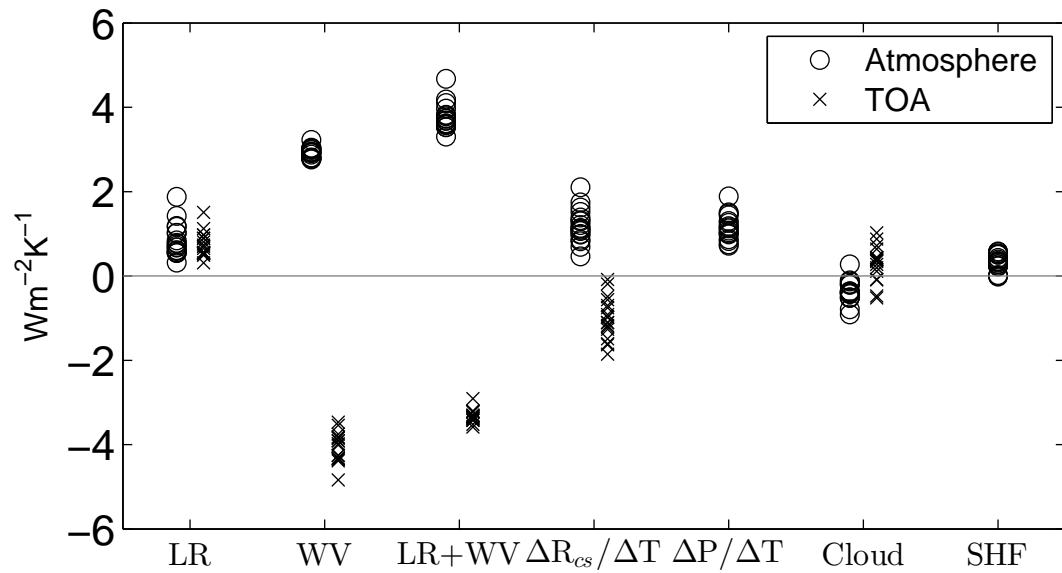


Figure 3.11: Clear-sky radiative responses at the TOA (x's) and for atmospheric cooling (circles) from different CMIP5 models. LW response to changes in lapse rate and water vapor are calculated with Fu and Liou (1992) radiative transfer code. ΔR_{cs} , Cloud, SHF , precipitation change are calculated directly from model output.

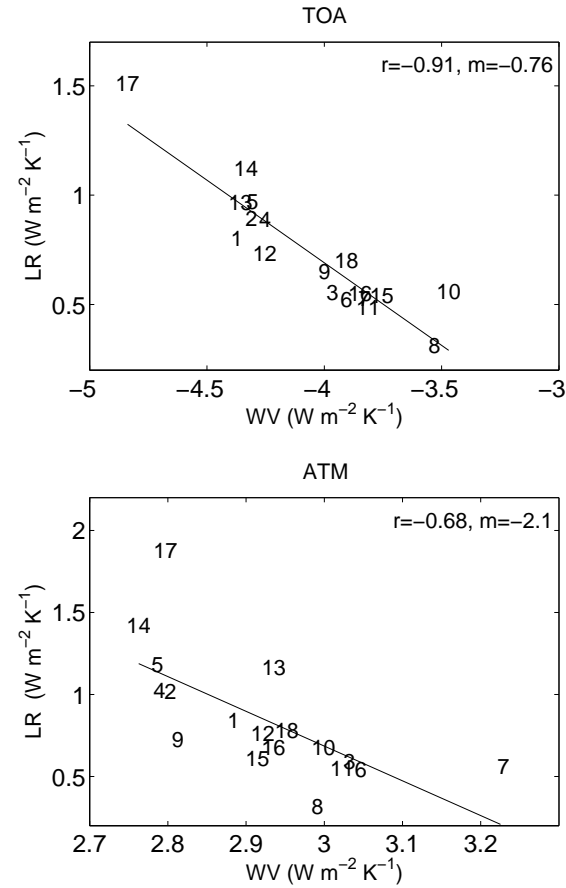


Figure 3.12: The relationship between the LW response to changing lapse rate and water vapor in CMIP5 simulations from different models according to calculations with Fu and Liou (1992) column radiation model for the TOA (top) and atmospheric column (bottom).

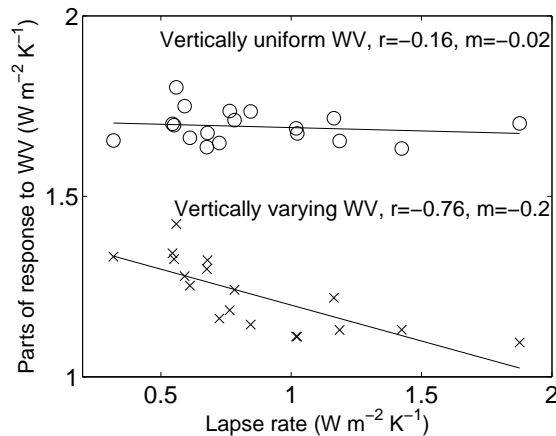


Figure 3.13: The relationship between the LW atmospheric cooling response to changing lapse rate (LR) and vertically uniform (circles) and vertically varying (x's) components of fixed-RH water vapor (WV) change in CMIP5 simulations from different models according to calculations with Fu and Liou (1992) radiative transfer code.

to changes in associated constant-RH moistening. However, the increased atmospheric cooling to the surface due to moistening that accompanies vertically-uniform warming is twice as large and of a different sign than for the TOA response in the multi-model mean (Table 3.2), and is unrelated to the response to changes in lapse rate (Fig. 3.13). This increase in emission to the surface due to moistening is the largest component of the atmospheric cooling response to moistening. So the part of the response to moistening that compensates for changes in lapse rate is smaller than it is for the TOA response, and the sum of the two still has a substantial range.

It should be noted that these findings are different from those of O’Gorman et al. (2012), who find that the compensation between the response to water vapor and lapse rate changes does extend to the atmospheric cooling. Their response to lapse rate is comparable to ours, but their response to water vapor has the opposite sign. One important difference between the analyses is that they examine models forced by a changes in aerosol forcing as well as greenhouse gases. Additional calculations with the same clear-sky radiative kernels (from Previdi 2010) indicate that our calculations

have a larger increase in emission to the surface due to moistening than theirs. Their clear-sky response to multi-model mean warming and moistening is $1.5 \text{ W m}^{-2} \text{ K}^{-1}$ smaller than ours.

The LW response to changes in lapse rate and moistening at constant RH, and the difference in SW absorption change across models each contribute to the inter-model spread in clear-sky atmospheric radiative cooling, and thus the rate of precipitation change. Changes in the cloud radiative effect are also a source of total-sky atmospheric cooling spread.

3.6 Discussion

3.6.1 Role of clouds and sensible heat flux

How do clouds play a role in precipitation change? Zelinka and Hartmann (2010) studied the LW cloud feedback (at the TOA) and showed that it is dominated by high clouds maintaining a constant cloud top temperature as the climate warms. This maintains nearly constant LW emission to space from these clouds. In the case of atmospheric cooling, high clouds will not contribute to changing emission to space unless cloud fraction changes, and they will shield some of the changes in clear-sky LW emission to space, as we saw in Section 3.4.3. If high clouds decrease in area or get warmer, precipitation will increase more with warming than otherwise. The presence of high cloud will mitigate some of the increase in radiative cooling calculated in our idealized setting.

Low clouds, on the other hand, increase precipitation. If low cloud were to decrease with global warming, this would result in decreased precipitation.

We can calculate the CMIP5 multi-model mean changes including clouds from total-sky TOA and surface radiative fluxes (rather than clear-sky, as in the rest of this study). The change in total atmospheric radiative cooling is $0.8 \text{ W m}^{-2} \text{ K}^{-1}$. Subtracting the change in clear-sky radiative cooling from the total radiative cooling

provides the change in atmospheric cloud radiative forcing, $-0.4 \text{ W m}^{-2} \text{ K}^{-1}$. This would reduce the precipitation increase compared to the clear-sky radiative response. The cloud radiative forcing change is driven by a change in LW cooling to the surface of $-0.9 \text{ W m}^{-2} \text{ K}^{-1}$, and is opposed by a change in LW cooling at the TOA of $0.4 \text{ W m}^{-2} \text{ K}^{-1}$ and a change in SW cloud radiative forcing of $0.1 \text{ W m}^{-2} \text{ K}^{-1}$. Simple calculations presented in Section 3.4.3 indicate that these are all consistent with a reduction in cloud fraction of both low and high clouds (Zelinka et al., 2012). Both changes in masking of clear-sky radiative cooling response and changes in the clouds themselves compose the cloud radiative forcing change.

In the multi-model mean of the transient CO_2 increase experiments (Table 3.1), sensible heat flux (from the surface to the atmosphere) decreases by $0.3 \text{ W m}^{-2} \text{ K}^{-1}$, or 30% of the precipitation increase. A reduction of sensible heat flux would support increased precipitation. This is a substantial but not dominant factor contributing to precipitation change. Coincidentally, perhaps, the changes in sensible heat flux and cloud radiative forcing nearly offset each other in this transient CO_2 increase experiment. Sensible heat flux plays a role in balancing global-mean precipitation change when changes in the climate state are very large (O’Gorman and Schneider, 2008).

3.6.2 Role of aerosol forcing

The atmospheric energy budget perspective on precipitation change is useful for climate forcing agents other than CO_2 . Black carbon is noteworthy because its TOA radiative forcing is small compared to its impact on precipitation change. Its main effect is to absorb SW in the atmosphere that otherwise would have been absorbed at the surface. While it causes warming as expected from its TOA radiative forcing, black carbon can dramatically reduce precipitation in ways that are not predictable from its TOA radiative forcing (Ming et al., 2010). Chapter 2 showed that variation in clear-sky shortwave absorption explains half of the variance across models in precipi-

tation change in the A1b scenario of AR4, and in two models the change in absorption is due to black carbon forcing prescription. For black carbon, the atmospheric energy balance is a more reliable guide than the TOA perspective.

Another interesting situation in which the atmospheric energy perspective can guide us is stratospheric sulfate aerosol geoengineering. McCusker et al. (2012) performed an experiment in which global-mean surface temperature was held constant by increasing CO₂ while simultaneously increasing sulfate aerosol in the stratosphere just enough to compensate. In this experiment, precipitation decreased steadily as CO₂ and stratospheric sulfate aerosol increased. We need only one of the calculations from our framework, the CO₂ forcing, to explain this experimental result. The CO₂ forcing caused the atmospheric cooling rate to decrease. The temperature did not change, so the surface temperature-dependent responses of atmospheric radiative cooling also did not change. The sulfate aerosol acts by reflecting SW to space that would usually be absorbed at the surface, but this has little effect on the atmospheric energy budget and precipitation. The CO₂ forcing can be viewed as directly suppressing the precipitation in this experiment, causing precipitation to decrease even without surface temperature change.

3.6.3 The surface energy perspective

In addition to the atmospheric radiative approach taken here, there are at least two other approaches to diagnosing the global-mean sensitivity of precipitation or evaporation to climate change: the surface radiation and the bulk flux perspectives. The bulk flux perspective is taken by Lorenz et al. (2010) and Richter and Xie (2008). Lorenz et al. (2010) differentiate the formula for bulk evaporative moisture flux from the ocean into terms depending on near-surface RH change, air-sea temperature difference change, and drag coefficient change (which includes changes due to near-surface wind speed). This approach paints a qualitatively different picture of surface turbulent moisture flux from the ocean, rather than radiative flux change globally (over

land as well as ocean), but both diagnostic approaches must be physically consistent; moisture and energy fluxes must balance.

As for the surface and atmospheric radiative constraints; there are reasons to choose the atmospheric energy constraint on precipitation over the surface energy constraint on evaporation. First, clouds have a strong effect on SW radiation at the surface, whereas they only weakly affect the atmospheric SW balance. SW reflected by clouds can have an effect on precipitation primarily by cooling the planet. Lambert and Webb (2008) pointed out that the shortwave cloud feedback does not enter the atmospheric radiation budget as it does the TOA radiation budget, which is fortuitous since the SW cloud feedback is the most uncertain component of the TOA radiation budget. However, SW cloud feedback is very important for the surface and planetary energy budgets.

The changes in SW cloud forcing for the atmosphere and surface in the CMIP5 multi-model mean are comparable in magnitude: $0.1 \text{ W m}^{-2} \text{ K}^{-1}$ in the atmosphere and $0.2 \text{ W m}^{-2} \text{ K}^{-1}$ at the surface. But the range of these values across the models is telling. For the atmosphere, the range is $0.2 \text{ W m}^{-2} \text{ K}^{-1}$, while at the surface it is $2.0 \text{ W m}^{-2} \text{ K}^{-1}$, ten times bigger.

Second, the surface heat capacity is bigger than the atmosphere's heat capacity, so the timescale for the surface to achieve balance is longer than the timescale for the atmosphere. For the surface to be in balance, we need to consider the ocean mixed layer, and deep circulation. The rate of change of storage in the ocean is estimated to be about 0.5 W m^{-2} at the present time (Loeb et al., 2012). The atmosphere equilibrates more quickly, so precipitation is more immediately constrained by the atmospheric budget.

3.7 Conclusion

Calculations with a column radiative transfer model and profiles of temperature and relative humidity quantify the sensitivity of the atmospheric cooling rate to uniform

warming, upper tropospheric amplification of warming, constant relative humidity moistening, and CO₂ forcing. These calculations are used to understand the changes driving atmospheric cooling, which is the thermodynamic constraint on global-mean precipitation response to CO₂ forcing. The change in atmospheric cooling accounted for here is $1.2 \text{ W m}^{-2} \text{ K}^{-1}$, and includes the response to changing temperature, constant relative humidity moistening, and CO₂ increase. In CMIP5 transient CO₂ increase experiments, clear-sky atmospheric cooling increases by $1.2 \text{ W m}^{-2} \text{ K}^{-1}$, while precipitation increases by $1.1 \text{ W m}^{-2} \text{ K}^{-1}$.

In both idealized calculations and in global warming simulations with GCMs, the atmospheric cooling rate response is dominated by surface, rather than top-of-atmosphere, flux change. The dominant response at the surface is increased downward emission from the atmosphere, to which increases in water vapor in the lower troposphere make the dominant contribution. We expect that the underlying principles of this framework should extend to other forcings including aerosols and non-CO₂ greenhouse gases as well (as in Kvalevåg et al. 2013).

Radiative responses to the presence of idealized clouds are calculated. High clouds suppress precipitation while low clouds enhance it. The change in GCM atmospheric column cloud radiative forcing (including both cloud feedback and change in cloud masking) due to CO₂ increase is $-0.4 \text{ W m}^{-2} \text{ K}^{-1}$, bringing the total atmospheric column radiative cooling increase to $0.8 \text{ W m}^{-2} \text{ K}^{-1}$.

We show that the inter-model spread in the rate of precipitation increase across the CMIP5 simulations can be attributed to differences in the atmospheric cooling. Clear-sky atmospheric shortwave absorption varies widely across models, not due to the spatial and temporal pattern of moistening, but more likely to differences in the formulation of shortwave absorption. The clear-sky atmospheric longwave cooling response to changing lapse rate and water vapor contribute substantially to the inter-model spread in atmospheric cooling rate, in contrast to the top-of-atmosphere. Cloud radiative forcing change has the same range of inter-model spread as each of the

aforementioned components, but it is not significantly correlated with precipitation change. Changes in relative humidity are not an important contributor to inter-model spread.

This study demonstrates that a nearly sufficient framework to understand the atmospheric energy constraint on global-mean precipitation is the clear-sky response of the atmospheric radiation to changes in profiles of temperature and moisture and to CO₂ forcing. This framework connects precipitation changes to temperature and moisture changes through their role in the atmospheric energy budget. These connections provide a straightforward physical understanding of how and why global-mean precipitation increases with global warming at a rate much less than the increases in water vapor.

Chapter 4

CHANGES IN THE DISTRIBUTION OF RAIN IN RESPONSE TO WARMING IN MODELS AND OBSERVATIONS

Chapters 2 and 3 examined how atmospheric radiative cooling responds to carbon dioxide increase, and established that global-mean precipitation responds to this change in radiative cooling. In this chapter, we explore how this response unfolds in terms of the distribution of rain frequency and intensity.

4.1 Introduction

Rain responds to global warming in climate models in two robust ways: the total amount of rainfall increases, and the rain rates of the heaviest events increase more. The rate of increase of global-mean rainfall is constrained by energetics to roughly 2 % K⁻¹ (Held and Soden, 2006), while the intensity of extreme events is driven by increases in moisture (specifically, moisture convergence) and increases by at least 5 % K⁻¹ (O’Gorman and Schneider, 2009a) but possibly much more (Allan et al., 2010). Trenberth (1999) determined that this disparity implies a change in the frequency distribution of rainfall toward more heavy rain, as well as a decrease in rain frequency.

We approach the response of the rainfall distribution from the energetic perspective. It is the latent heat imparted by rain, rather than rain frequency, that is energetically constrained. For this reason, we focus on the distribution of rain amount. The energetic perspective also motivates us to take a global perspective to integrate over large areas that include shifts of precipitating systems in space, and ensure that we capture the entire distribution of rain, without missing the heaviest events, which

make substantial contributions to rain amount.

Atmospheric cooling is smoother in space and time than precipitation, so we expect the increased atmospheric cooling to affect the entire precipitation distribution. We anticipate coherent modes of change, where changes at any rain rate are related to those at other rain rates, so we formulate modes of response of the distribution.

The goals of this study are: to describe the character of the changes in precipitation that balance increased atmospheric cooling, and to quantify ways the distribution of rain could change in order to understand how the constraints of energy and moisture are simultaneously met. To accomplish this, we introduce two modes of coherent change of the rain amount distribution: an increase in rain amount at all rain rates (the increase mode), and a shift of the rain amount distribution to higher rain rates (the shift mode). The increase mode changes the total amount of rain, while the shift mode is energetically neutral. We apply these two modes to the GCM response to CO₂ increase, and to the responses of modeled and observed distributions over ENSO phases. In addition to the coherent modes of response, some models show an isolated response at heavy rain rates, which we call the extreme mode.

In the next section, we introduce the GCM and observational datasets we will use, and consider the climatological rainfall distributions. Then, we discuss the two modes of change. Next, we fit the modes of change to the rain amount response to carbon dioxide increase and ENSO phases in CMIP5 models, and ENSO phases in observations. Later, we consider the implications for the change in frequency distribution, particularly extreme events. Finally, we try to understand the differing responses across models.

4.2 Data and methods

In this section we document the GCM simulations and observational datasets, and our methodology for calculating the distributions. We analyze daily rainfall accumulation from models and observations.

4.2.1 *Daily rainfall data*

To calculate the model precipitation distributions and their response to CO₂ doubling, we use climate model simulations from the CMIP5 archive (Taylor et al., 2012). Models whose simulations we use are listed in Table A.1. We use simulations from three experiments; one-percent-per-year CO₂ increase (1pctCO2), Representative Concentration Pathway with radiative forcing reaching 8.5 W m⁻² near 2100 (RCP8.5), and Atmosphere Model Intercomparison Project (AMIP). The fully-coupled 1pctCO2 scenario provides the response to CO₂ doubling. We compare years 1-10 (the start of the simulation) and years 61-70 (CO₂ doubles at year 70). We use one ensemble member from each of the 22 models with archived daily rainfall accumulation and surface air temperature. To evaluate the response to tripling of CO₂, we take years 102-111 of the experiment, and for CO₂ quadrupling we use years 130-139. From the RCP8.5 simulations, we compare 2006-2015 with 2090-2099. For models and scenarios where convective and large-scale precipitation are separately reported, we perform a separate analysis of these classes of model precipitation.

To examine the modeled response to ENSO, we use the AMIP experiments from the CMIP5 archive, though they are not coupled. In AMIP experiments, sea surface temperature (SST) is prescribed from observations over the historical period, along with prescribed historical forcings. These experiments allow us to examine the modeled response to ENSO SST forcing despite that not all models have good ENSO responses when run in coupled mode. We use one ensemble member from each of the 27 models with archived daily precipitation data from 1979-2007. We normalize by each model’s tropical mean surface air temperature change from cold to warm ENSO phase. We choose warm and cold ENSO months based on the same NINO3.4 dataset index we use for observational data (described below), which is possible because the SSTs are prescribed in the models.

For observational distributions of rainfall and its response to ENSO phases, we use

two gridded observational datasets that merge data from satellite and rain gauges. Global Precipitation Climatology Project One-Degree Daily data (GPCP 1DD, Huffman et al., 2001) has global coverage at one degree resolution in latitude and longitude. We use data from 1997-2012. TRMM 3B42 version 7 (Huffman et al., 2007) covers 50 S to 50 N at 0.25 degree resolution from 1998-2012.

To determine ENSO phase, we obtained the monthly timeseries of SSTs in the NINO3.4 region (5 N - 5 S, 170-120 W) from NOAA ESRL PSD (<http://www.esrl.noaa.gov/psd/data/climateindices/list>) and calculated NINO3.4 index following Trenberth (1997). For the warm phase composite, we choose the months with the highest NINO3.4 index. We use 50 months for observations and 100 for AMIP simulations (to make use of the longer model simulations). Because we do not remove the seasonal cycle when calculating the rainfall distribution, it is important to make sure we use the same months of the year in the warm and cold phases. In order to enforce this requirement, we choose cold months so that the distribution of months is the same as for the warm months. For example, 5 of the warm months over the GPCP period are January, so we choose the 5 coldest Januaries for the cold phase. We use HadCRUT4 (Jones et al., 2012) to calculate the observed change in tropical surface temperature from cold to warm ENSO phase (0.35 K for the GPCP period).

Finally, we touch briefly on the climatological rainfall distribution from weather stations with the Global Historical Climatological Network Daily data (Klein Tank et al., 2002). We use only the GCOS surface network (GSN) subset of stations, which are distributed more evenly than the full set of stations (though station data is only available on land). Following IPCC (2013), we only use stations with at least 40 years of data ending after 2003.

4.2.2 Calculating rain amount and rain frequency

Now that we have described the datasets that we are using, we next discuss our methodology for calculating distributions of rain amount and frequency, and their

changes.

We analyze daily rainfall accumulation data, rather than instantaneous, hourly, 5-day or monthly data. Trenberth et al. (2003) and Stephens et al. (2010) argue that instantaneous rain rate is the best variable to consider. However, Liu and Allan (2012) find that some averaging of observational data is necessary for purposes of inter-comparison. They show that the distributions of precipitation in satellite data and gridded analyses agree better when averaged over five days than for daily or instantaneous data. Daily satellite observations are the average of only two snapshots, while the daily merged, gridded products have more implicit averaging. Other recent studies use monthly-mean data to look at the distribution of rain (Liu et al., 2012; Lau et al., 2013). This removes all variability on less than monthly timescales, which is not desirable. Daily gridded data preserves as much information as possible by providing some temporal averaging, but not more than is necessary to make (gridded) observations comparable with models.

The choice of rain rate bin structure is fundamental to all rainfall distribution calculations. Rain rate, even accumulated over a day, varies by over orders of magnitude from day to day and from one location to another. A wide variety of possible bin structure choices can be found in the scientific literature. Some studies use linearly distributed rain rate bins, often with 1 mm d^{-1} spacing (e.g., Chou et al., 2012). Linear spacing of bins has the benefit that the bins are related in an obvious way, but a substantial drawback is that the bins do not have reasonable sampling at high rain rates. Other studies use irregular bin spacing to improve sampling and capture the entire distribution, but this may make it impossible to work with the distribution mathematically. Following Watterson and Dix (2003), we use logarithmically-distributed rain-rate bins. This coordinate makes mathematical operations tractable and captures the entire distribution from light to heavy rain with adequate sampling.

In log coordinates, each rain rate bin is a fixed percentage wider than the previous one, and has a bin center the same percentage larger. We choose bin spacing of seven

percent to balance resolution and sampling. For example, one rain rate bin is centered at 10.6 mm d^{-1} and has a width of 0.78 mm d^{-1} , while the next bin is centered at 11.4 mm d^{-1} and has width 0.84 mm d^{-1} . The smallest non-zero bin is centered at 0.03 mm d^{-1} and has width 0.0025 mm d^{-1} , and the largest bin needed for CMIP5 model data is centered at 663 mm d^{-1} and has width 49.0 mm d^{-1} . Bins include all rain rates in the dataset greater than 0.03 mm d^{-1} and are spaced widely enough to provide adequate sampling. Because of the logarithmic structure, movement along the rain rate axis is expressed as a percentage change in rain rate. A seven percent increase in rain rate is simply a movement of one rain-rate bin.

Another decision that must be made is the dry threshold. The ability to detect rainfall varies by measurement technique. Gridded observations and model data represent a spatial average rather than a single point in space, so that an objective threshold is not obvious. Some studies and guidelines define wet days as having a minimum accumulation of 1 mm (Sun et al., 2006; Klein Tank et al., 2009). Other studies extend the dry threshold to 0.1 mm d^{-1} (e.g., Chou et al., 2012). We extend the distribution to somewhat below 0.1 mm d^{-1} to capture most of the distribution. We add into the dry frequency the amount below the dry threshold, which is an additional 3% of days in GPCP. We miss a negligible amount of the total rainfall (0.014% in GPCP) by ignoring the rain amount below the dry threshold.

Focusing on the global scale allows us to integrate over spatial shifts in precipitating systems, like the ITCZ and storm tracks, which occur with climate change. Some studies (e.g., Pall et al., 2007; O’Gorman and Schneider, 2009a) take a zonal mean perspective, in which expected shifts of the ITCZ and storm tracks are prominent. Watterson and Dix (2003) look at the changes in distributions at individual locations. For changes in precipitation at many locations (and thus for impacts of precipitation change), geographical shifts in precipitation systems may dominate over thermodynamic effects.

Spatial resolution of precipitation data has been identified as a contributing factor

to disagreements among observational datasets and between models and observations (Chen and Knutson, 2008; Kopparla et al., 2013). When comparing two distributions, we coarsen the higher spatial-resolution precipitation data using an averaging scheme that conserves the total amount of rain (Jones, 1999) before calculating the distribution. We coarsen the 0.25 degree TRMM dataset to the 1 degree GPCP grid. Model resolution ranges from 0.75 to 2.8 degrees (for models analyzed from the CO₂ increase experiment). We coarsen the GPCP to model grids when the model resolution is more coarse than 1 degree, and coarsen neither GPCP nor the model for the two models with at least 1 degree resolution. Both daily gridded data and model data have implicit spatial averaging, so in this sense they are fundamentally different from station data, which represent single points in space.

With these decisions about coordinate system, dry threshold, and spatial averaging made, we calculate the distribution of rain frequency and amount. At each grid-point, we calculate the rain histogram to form the rain frequency distribution. We tabulate the total amount of rain that falls in each rain rate bin to form the rain amount distribution. Then we take the area-weighted average of the distributions over the globe to obtain global-mean distributions. A mathematical description of how we calculate the distributions is presented in Appendix B.

Climate models calculate rain in two different ways: when a grid cell reaches saturation, they create large-scale (or resolved) precipitation, and a convective parameterization produces rain that represents events unresolved at the grid scale. We calculate two additional distributions using daily convective rainfall data. The first is the convective precipitation fraction in each bin of total rain rate. The second is the amount of convective precipitation falling in each total rain rate bin. These are also described in Appendix B.

We calculate rain amount and rain frequency distributions separately for the first ten years of the CO₂ doubling model simulations and the ten years immediately prior to doubling (years 61-70), and for the warm and cold phases of ENSO. We report

the absolute changes in rain frequency and rain amount. Some studies report the percentage change of rain frequency and amount distributions (e.g., Sun et al., 2007; Lau et al., 2013), but this has some undesirable properties. The maximum rain rate increases with warming, so for the highest rain rates the percent change in the distribution is not defined. The percentage change will also depend very strongly on the bin structure used. For these reasons, we look at absolute changes in the rain frequency and amount distributions.

Extreme precipitation is typically quantified by the rain rate for some cumulative percentile of the rain frequency distribution (e.g., Allen and Ingram, 2002; Pall et al., 2007; O’Gorman and Schneider, 2009a). Using our global distribution of rain frequency, we form the cumulative probability distribution of rainfall. We include both wet and dry days, following other studies (e.g., O’Gorman and Schneider, 2009a). Including wet and dry days in cumulative frequency calculations increases agreement between models and observations. We then interpolate the rain rates from this cumulative distribution onto a logarithmic percentile axis to compare the rate rain as a function of percentile between an initial distribution and a later one. We report the percent change in rain rate at a given percentile of the distribution. The large range of rain rates makes relative change a convenient measure.

Finally, we put error bounds on our calculated distributions. To estimate the error in model simulations, we use the spread across models as a measure of variability, and determine the 95 % confidence interval using the Students t -test assuming each model is independent. To estimate the error of our observed composites, we calculate the distribution for each month of the 50 months of data separately, and then determine the 95 % confidence interval using the difference-of-means test.

4.3 *The rain amount distribution and its change*

4.3.1 *Climatology*

In this section we look at similarities and differences among modeled and observed rain amount and rain frequency distributions. The global-mean distributions of rain amount and rain frequency for both GPCP and the CMIP5 multi-model mean are shown in Fig. 4.1. To address potential inconsistency between models and observations due to their differing resolution, the GPCP distribution is calculated as follows. The GPCP data is coarsened to each model's grid, the distribution of the coarsened GPCP data at each grid-point is calculated, each distribution of coarsened data is averaged globally, and then the global distributions are averaged together to obtain the distribution shown in Fig. 4.1. The GPCP and model rain amount distributions agree broadly. They both peak around 10 mm d^{-1} , and are in agreement for moderate rain rates. But, the model rain amount is slightly higher at the highest and lowest rain rates. The GPCP rain amount distribution is narrower than the multi-model mean. The area under the rain amount curve is the global-mean rainfall, which is lower in GPCP, at 2.7 mm d^{-1} , than in the models, at 2.9 mm d^{-1} . Stephens et al. (2012) argued that GPCP underestimates the total rainfall compared to what is needed to balance observed atmospheric radiative cooling.

The multi-model mean rain frequency distribution agrees relatively well with GPCP above about 10 mm d^{-1} . At lighter rain rates, between about 0.1 and 5 mm d^{-1} , models have a much higher frequency of rain than GPCP or TRMM. Modeled rain frequency peaks at 1.1 mm d^{-1} , where it is nearly twice as frequent as GPCP. Models and GPCP disagree drastically on the dry-day frequency. The dry-day frequency is 24% in the multi-model mean, but 42% in GPCP. Extending the precipitation bins below 1 mm d^{-1} heightens the discrepancy compared to studies that include this light rain in the dry-day count.

The rain amount distribution emphasizes higher rain rates more than the rain

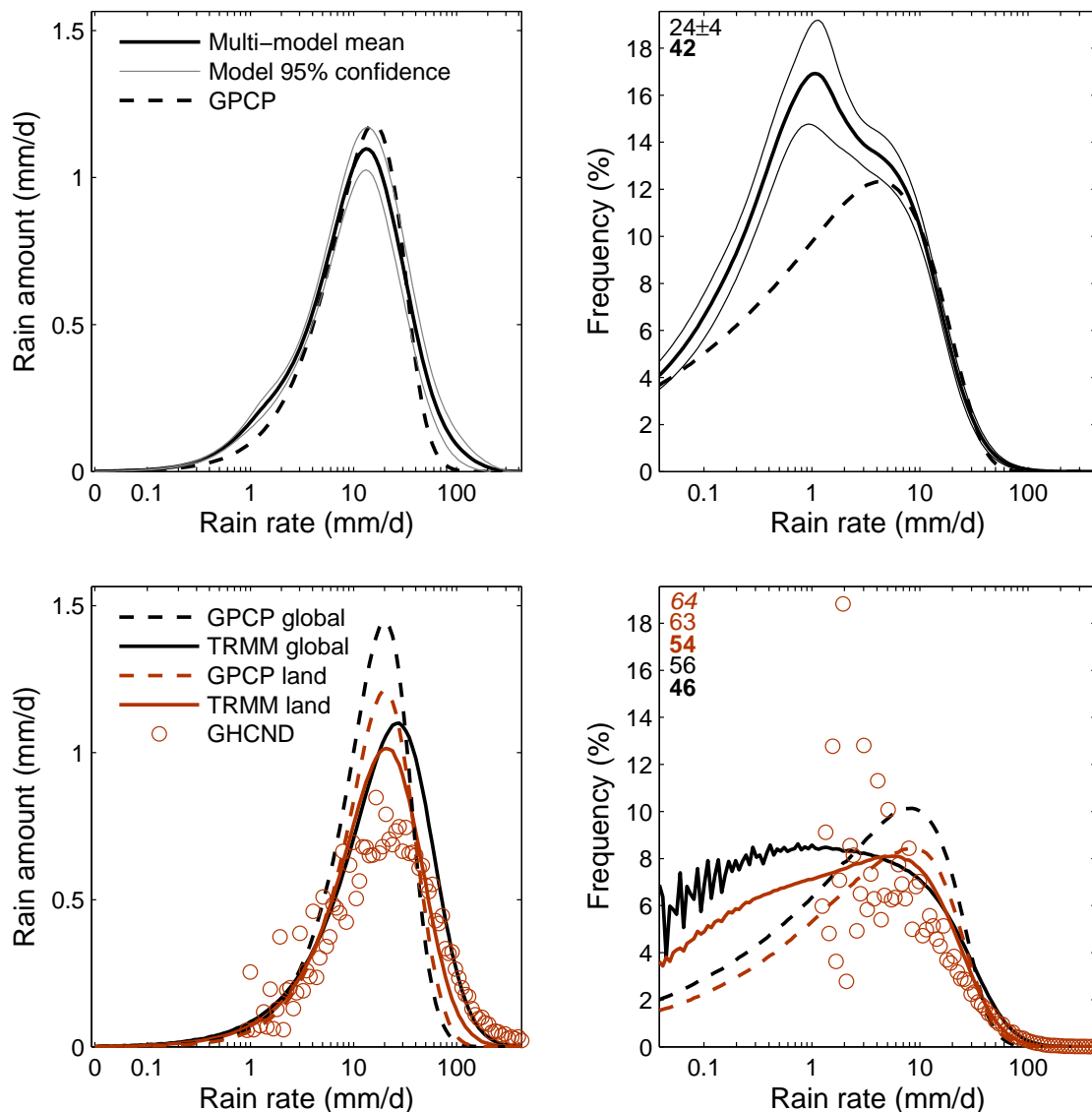


Figure 4.1: (left) Rain amount (mm d^{-1}) and (right) rain frequency distribution (%) climatologies in (top) CMIP5 models and GPCP observations globally and (bottom) TRMM 3B42 and GPCP gridded observations from 50 S to 50 N. For observational data, both total (black) and land (brown) are shown. Dry frequency is noted at the top left, with GHCND in italic, models and TRMM in bold, and GPCP normal. Gridded observations are coarsened before distributions are calculated. Gray lines show the 95% confidence interval on the multi-model mean according to the student's t -test across the model distributions.

frequency distribution does. Models and observations agree better at higher rain rates than lower ones, so the modeled rain amount distribution is more similar to GPCP than the frequency distribution. The similarity in rain amount despite differences in rain frequency could be anticipated because rain amount is an important factor in the energy budget, and models are roughly in energetic balance. The other side of this coin is that having many or few light rain events makes only a small difference in terms of latent heating.

Most models have a shape similar to GPCP, with a peak somewhere slightly above 10 mm d^{-1} , shown in Figure 4.2. Some models (including BCC-CSM1.1 and IPSL-CM5B-LR) have an extra feature on the high end of the distribution, and the IPSL models each have an extra bump at light rain rates. Many models have distributions that closely resemble GPCP, including the MPI-ESM models (Mauritsen et al., 2012).

The bottom panels of Figure 4.1 compare the rain amount and rain frequency distributions from different observational datasets. Data are restricted to $50 \text{ S} - 50 \text{ N}$ consistent with TRMM's coverage, and coarsened to the GPCP 1-degree grid. The datasets agree on the general shape of the distribution, but disagree on many details. TRMM has a broader distribution of rainfall than GPCP, with more rain at low and high rain rates, particularly over ocean. The datasets agree closely the total amount of precipitation. Overall, GPCP and TRMM show better agreement on rain amount than rain frequency, just as GPCP and models agree better on total amount than frequency.

Also included in the bottom panels of Figure 4.1 is the distribution of station-based GHCND data, which can be most closely compared with land data from GPCP and TRMM, though the station data measures rain at individual points in space (and only locations with weather stations) while GPCP and TRMM represent area-averaged rain accumulation. Because GHCND data is stored with a resolution of just 0.1 mm d^{-1} , calculating the distribution for wet days below about 10 mm d^{-1} of rain is problematic (as is evident in the rain frequency distribution). At the heaviest rain rates,

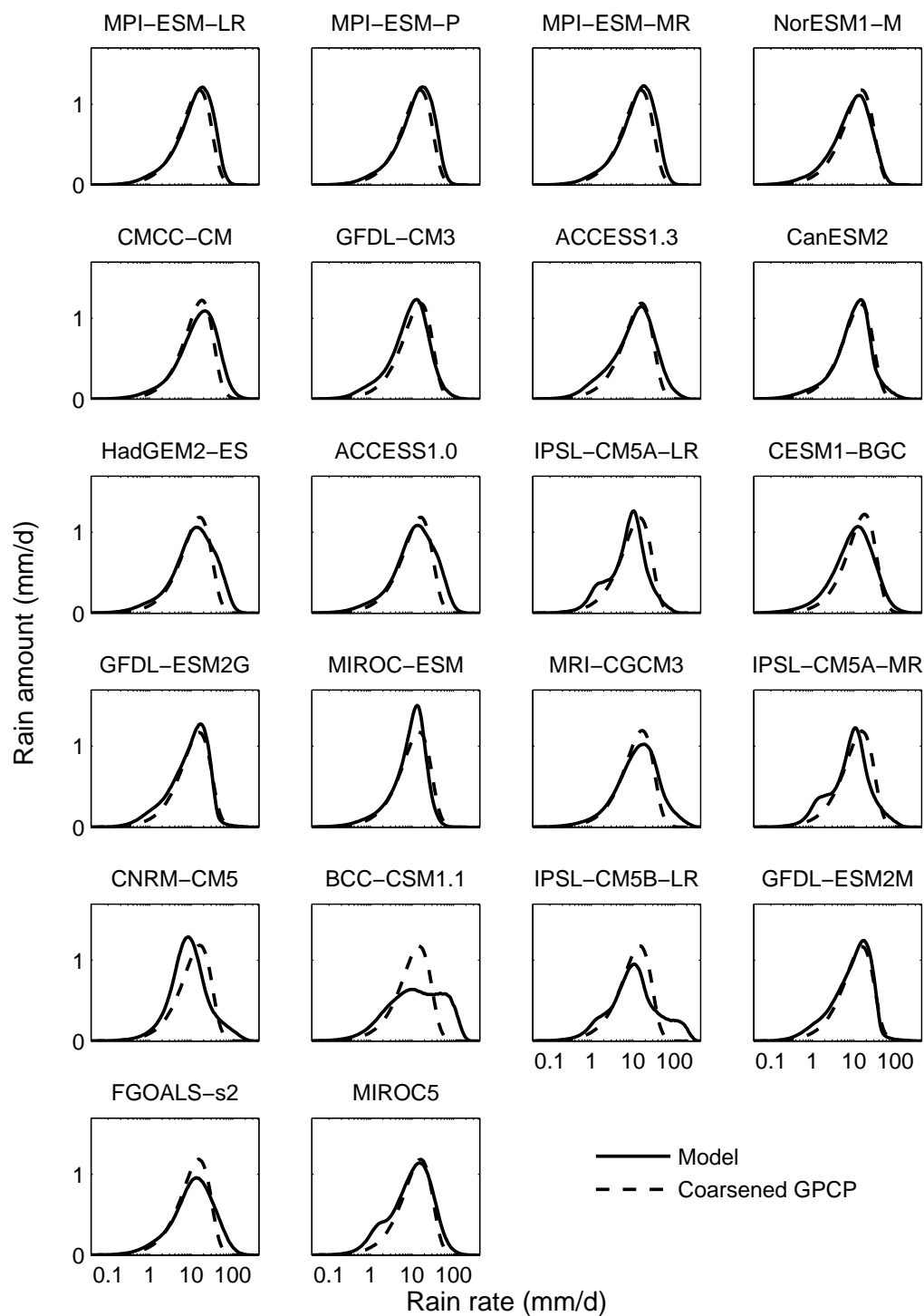


Figure 4.2: Rain amount distribution for each CMIP5 model (thick solid lines) and GPCP (dashed lines; GPCP data is coarsened to model grid before binning as in Fig. 4.1).

TRMM and GPCP slightly underestimate rain amount compared to GHCND, while at moderate rain rates they underestimate it more severely. The dry-day frequency in GHCND data agrees more closely with TRMM than GPCP. Overall, the degree of agreement on rain amount among the three observational datasets is reassuring.

We focus our analysis on the change in modeled and observed distributions relative to their own base states to account for the differences in climatological distributions among models and observations.

4.3.2 *Two modes of change: shift and increase of rain amount*

In this section we will formulate some simple modes of change of the rain amount distribution. Before considering changes in rain, we must define some terms. The rain rate r is in mm d^{-1} , though we'll work in coordinates of $\ln r$. The cumulative distribution of rain amount $P(r)$ is,

$$P(r) = \int_{\ln r_{min}}^{\ln r} p(\ln \dot{r}) d \ln \dot{r}, \quad (4.1)$$

where $p(\ln r)$ is the precipitation density function. Dots indicate placeholder variables over which the integral is taken. The units of P are mm d^{-1} , and $p = dP/d \ln r$. Then the total rainfall (the global-mean precipitation) is $\bar{P} = P(\infty) = P(r_{max})$. The dry-day threshold is r_{min} , and the maximum daily rainfall in our dataset is r_{max} . We assume $P(r_{min}) = 0$. The cumulative distribution of rain $F(r)$ is,

$$F(r) = \int_{-\infty}^{\ln r} f(\ln \dot{r}) d \ln \dot{r} = F_d + \int_{\ln r_{min}}^{\ln r} f(\ln \dot{r}) d \ln \dot{r}, \quad (4.2)$$

where $f(\ln r)$ is the probability density function of rain, and $F(\infty) = F(r_{max}) = 1$. We'll refer to f as the rain frequency distribution. $F_d = F(r_{min})$ is the dry-day

frequency. The rain amount (p) and rain frequency (f) distributions are related by,

$$p(\ln r) = r f(\ln r), \text{ and} \quad (4.3)$$

$$f(\ln r) = \frac{p(\ln r)}{r}. \quad (4.4)$$

We have $d \ln r = dr/r$, and as long as changes are small, we can approximate the infinitesimal changes with finite ones, $\Delta \ln r = \Delta r/r$. We express $\Delta r/r$ in percent. Changed distributions will be indicated by primes (f' , p' , and F'_d).

How might the distributions of rain amount and rain frequency respond to changes in climate? One way rain could change is that it could become more frequent. The distribution of rain when it is raining would stay the same, but it would rain more often, with more rain falling at each rain rate. We'll call this mode the *increase mode*. If the rain increases by a fraction a at each rain rate,

$$p'(\ln r) = (1 + a)p(\ln r), \text{ which also requires} \quad (4.5)$$

$$f'(\ln r) = (1 + a)f(\ln r). \quad (4.6)$$

The increase mode results in a decreased dry-day frequency, $F'_d = 1 - (1 + a)(1 - F_d)$, and an increase in total rainfall $\bar{P}' = (1 + a)\bar{P}$. Note that the increase in rain must be balanced by a corresponding increase in total atmospheric cooling. We can also have negative a , where the total precipitation and frequency of rainfall decrease.

The increase alone is unlikely for energetic reasons and lacks some features that we might anticipate in the rainfall response. For example, it does not allow for an increase in the maximum rain rate. For fixed circulation, we expect an increase in the maximum rain rate in a moister atmosphere. Also, the increase requires a change in the total atmospheric cooling needed to balance precipitation, which must be achieved by increased loss to space or to the surface (Chapter 3).

Another possible response is that the rain amount distribution could shift to higher

rain rates. Then, the same amount of rain would fall, but at higher rain rates. If the distribution stays the same shape, enclosing the same total area, then this change will be energetically neutral, not requiring a change in the atmospheric radiative cooling to balance it. If the distribution shifts to the right by $b = \Delta r/r$, then this *shift mode* is,

$$p'(\ln r) = p(\ln r - b). \quad (4.7)$$

If the same amount of rain falls at higher rain rates, then less time is spent raining. So, we should expect the rain frequency to decrease and dry-day frequency to increase with a shift to higher rain rates. Noting that $r(\ln r - b) = re^{-b}$, we can find the new frequency distribution,

$$f'(\ln r) = e^{-b}f(\ln r - b), \quad (4.8)$$

$$F'_d = 1 - \frac{1 - F_d}{e^b}. \quad (4.9)$$

The total rainfall does not change, so $\overline{P}' = \overline{P}$. A schematic of the increase and shift is shown in Fig. 4.3.

The modes we have chosen to focus on are somewhat arbitrary; others are possible. One can imagine a mode where the shape of the rain frequency distribution and the total frequency of rain do not change, but rain amount increases when it is raining. This would be a shift of the rain frequency distribution to higher rain rates, $f'(\ln r) = f(\ln r - \Delta \ln r)$, analogous to the shift of the rain amount distribution in the shift mode. This would not change the dry-day frequency, but the total amount of rain would increase, and the shape of the rain amount distribution would change. In fact, this movement of the rain frequency distribution with no change in shape is equivalent to the shift and increase modes simultaneously changing by the same amount, $a = b$ (for small changes $a, b \ll 1$ when f and p can be linearized). We'll call this the

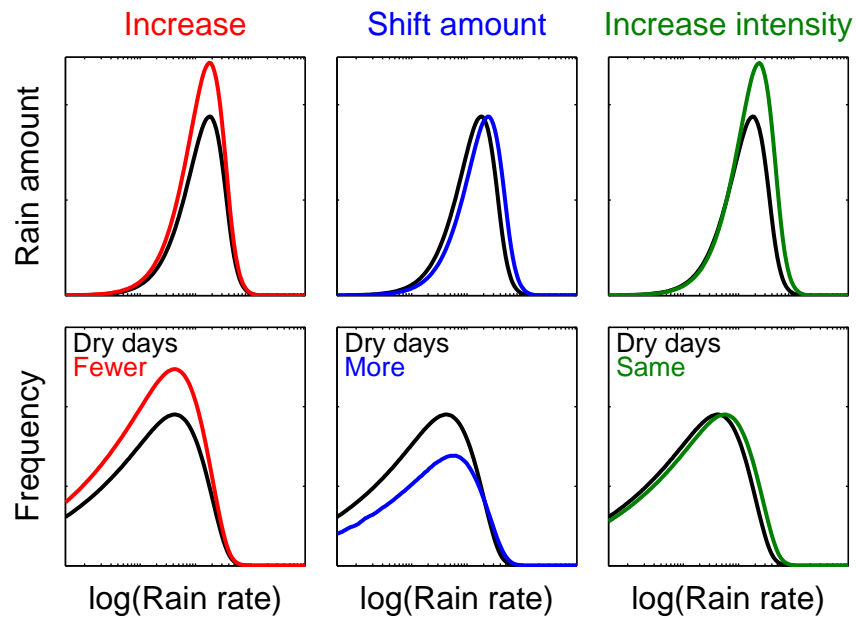


Figure 4.3: Schematic of the modes of change of the rain distribution introduced here: the increase (red, left), shift (blue, center), and increase intensity (green, right) in the rain amount distributions (top) and the accompanying rain frequency distributions (bottom). Initial distributions from GPCP are shown in black, and the new distribution resulting from a large, 30 %, shift or increase shown in color. Only the increase mode and shift mode are used in calculations; the third mode occurs when the first two have equal magnitude.

increased intensity mode. Because this mode is degenerate with the sum of the shift mode and the increase mode, we will show it schematically but we will not calculate it independently.

4.3.3 *The shift and increase in response to CO₂ doubling*

In this section we compare the response of CMIP5 models to CO₂ doubling using our modes of change as metrics. Water vapor increases at around 7 % K⁻¹, and previous work discussed in Section 4.1 established that rate as a reasonable estimate of the change in extreme precipitation. What would the response of the rain distribution to a 7 % increase mode, shift mode or increased intensity mode look like? Figure 4.4 shows these changes in terms of the rain amount, rain frequency, and extreme precipitation response, along with the CMIP5 multi-model mean response to CO₂ doubling.

To calculate the CMIP5 multi-model mean response, the globally-averaged rain amount and rain frequency distribution for each model is calculated for the first ten years of the simulation, and for the ten years immediately prior to CO₂ doubling. The model distributions are averaged together to get the initial and doubled-CO₂ distributions. Finally, the initial rain amount and rain frequency distributions are subtracted from the doubled-CO₂ distributions.

First, focus on the change in rain amount distribution. The CMIP5 response has an increase at heavy rain rates and a decrease at moderate rain rates, though the total area under the change curve is positive (indicating increased total rainfall). The shift mode resembles the rain amount distribution most closely, both in the amount of the change that it captures and in overall shape. Recall (from Section 1.3) that other studies have found an increase at high rain rates and decrease at moderate rain rates, reminiscent of this shift. The zero-crossing line of this shift occurs at the peak of the rain amount distribution, around 10 mm d⁻¹. The increased intensity mode has far too high of a peak, and lacks the minimum at moderate rain rates shown by

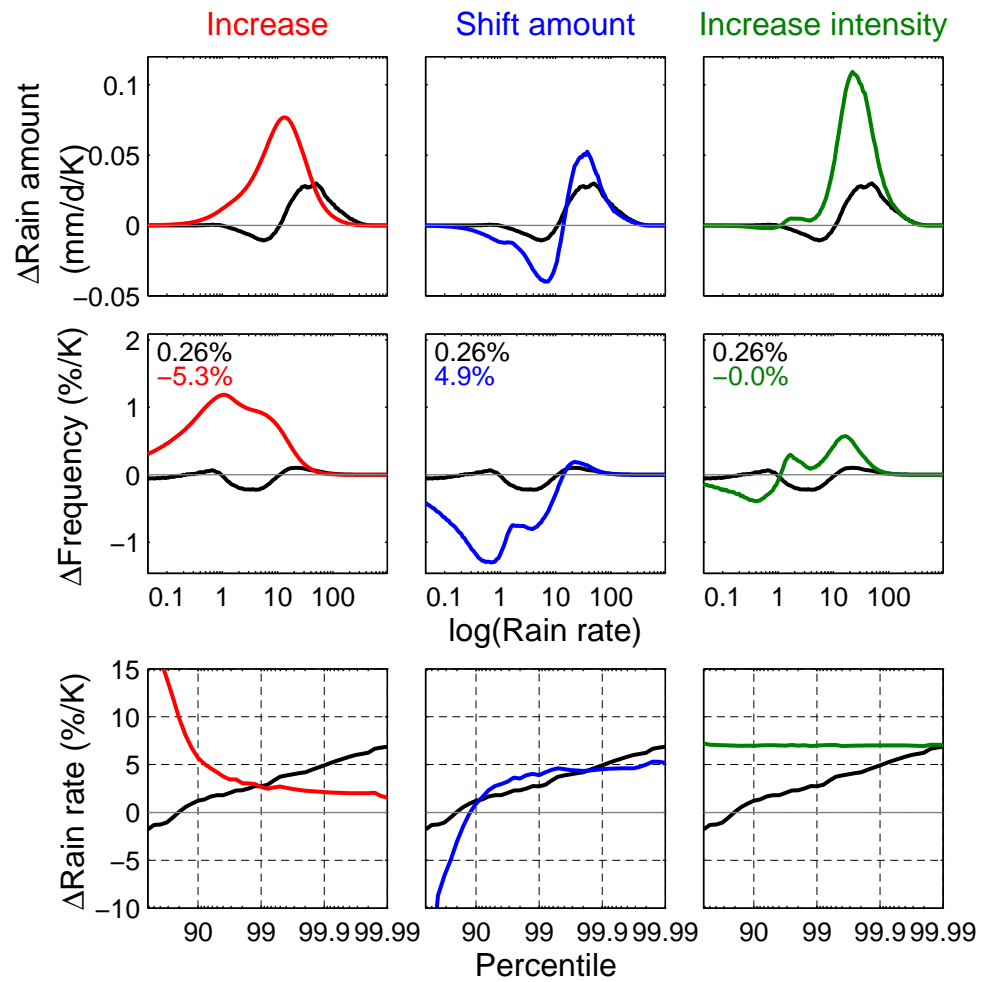


Figure 4.4: The change in (top) rain amount, (middle) rain frequency, and (bottom) extreme rain in the CMIP5 multi-model mean CO_2 doubling experiment (black), and the changes resulting from (left, red) an increase, (center, blue) a shift, or (right, green) an increase in intensity of the CMIP5 multi-model mean by 7 %. The change in dry-day frequency of the CMIP5 multi-model mean (black) and each mode (color) is noted at the top left of the center panels.

the shift mode. For all three modes, a change of 7 % K^{-1} greatly overestimates the model response.

Now turn to the response in rain frequency distribution. The model response shows slight increases at heavy rain rates and decreases at moderate rain rates (consistent with the change in rain amount). It also has a slight increase at light rain rates which plays a negligible role in the rain amount distribution. Finally, dry-day frequency increases modestly. This pattern is consistent with Lau et al. (2013).

Both the increase and shift modes show some agreement with the change in frequency at high rain rates, but these make up only a small portion of the change in rain frequency (in contrast with rain amount). The model response has a small increase in dry-day frequency, consistent with the shift. Both the increase and shift of 7 % K^{-1} drastically overestimate the comparatively modest changes in rain frequency. The increased intensity pattern shows a more reasonable degree of change, since it is the difference between the large and opposing changes in the increase and shift modes, but the pattern of change it shows is inconsistent with the model response. Note that in this frequency shift, the zero-crossing occurs at the peak of the rain frequency distribution, which is at light rain rates for the multi-model mean. Light rain decreases in frequency, while both moderate and heavy events increase.

Finally, focus on the extreme precipitation response. The model response is modestly negative below the 80th percentile, and increases with percentile almost linearly (though the percentile scale is logarithmic), reaching 7 % K^{-1} at about the 99.99th percentile. The shift mode comes closest to matching the shape of the modeled extreme precipitation response. But, it underestimates the response at the highest and lowest rain rates and overestimates it at moderate rain rates. In contrast, the increase mode has increases at all percentiles, which decrease with rain rate. It has dramatic increases in rain rate at moderate percentiles and more modest increases at the highest percentiles. The increased intensity is the superposition of these, with rain rate increasing 7 % at all percentiles. It is consistent with the response at the 99.99th

percentile, but overestimates the response in the rest of the distribution.

Instead of arbitrarily choosing a shift and increase of 7 % K⁻¹, we can calculate the magnitudes of the shift and increase modes that produce the closest possible fit to the model response. We can superpose the shift and increase to allow aspects of both modes in our fit. We will call their superposition the *shift-plus-increase*.

In order to optimize the shift-plus-increase, we make some assumptions. First, we assume that all changes are small, so changes in p can be linearized,

$$p(\ln r - b) \approx p(\ln r) - b \frac{dp}{d \ln r}. \quad (4.10)$$

Next, the model distribution and its response are discrete distributions, so we use a discrete approximation to the problem. Then, we must choose an error metric. We choose the sum of the square of the difference between the shift-plus-increase and the model response, $E = \sum (\Delta p - \Delta p^m)^2$, where Δp^m is the model response, $\Delta p = p' - p$, and the sum is taken over all r bins.

To fit the magnitude of the increase and shift, a and b , we find where E has a local minimum with respect to each of a and b . This produces the following two-variable linear set of equations,

$$\begin{bmatrix} \Sigma p^2 & -\Sigma p \frac{dp}{d \ln r} \\ -\Sigma p \frac{dp}{d \ln r} & \Sigma \left(\frac{dp}{d \ln r} \right)^2 \end{bmatrix} \begin{bmatrix} a \\ b \end{bmatrix} = \begin{bmatrix} \Sigma p \Delta p^m \\ -\Sigma \frac{dp}{d \ln r} \Delta p^m \end{bmatrix}. \quad (4.11)$$

We cannot also fit the increased intensity mode because it is degenerate with the sum of the shift mode and increase mode, so Equation 4.11 would be under-determined. We must choose two of the three modes to fit, and we choose the shift and increase modes.

The optimal shift-plus-increase for the multi-model mean response is shown in Fig. 4.5. The magnitude of the shift mode is 3.3 % K⁻¹ and the increase mode is 0.9 % K⁻¹. Between about 1 and 50 mm d⁻¹, the shift-plus-increase falls within the

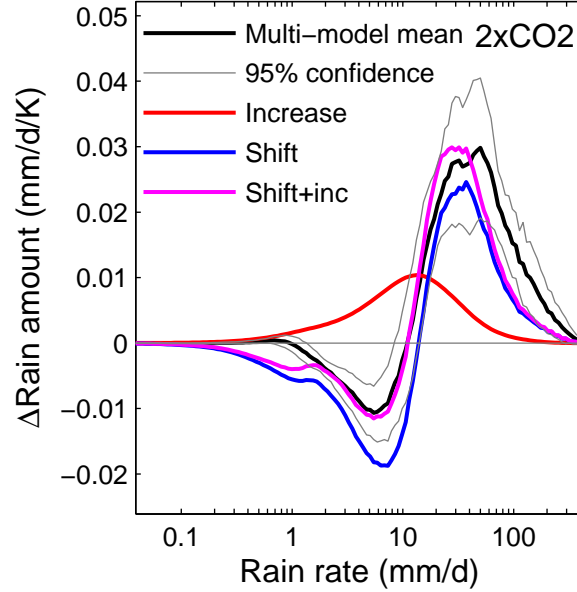


Figure 4.5: CMIP5 multi-model mean rain amount response to CO_2 doubling ($\text{mm d}^{-1} \text{K}^{-1}$). The model response (black), increase (red), shift (blue), and shift-plus-increase (magenta) are shown. Gray lines show 95% confidence interval of the multi-model mean response.

range of uncertainty in the model response. At the highest and lowest rain rates, the shift-plus-increase underestimates the rain amount response. The sum of squared differences will emphasize the largest differences, but we are more interested in how much of the change in rainfall is captured by the response. We report the error in terms of how much of the precipitation response it fails to capture,

$$Error = \frac{\sum |\Delta p - \Delta p^m|}{\sum |\Delta p^m|}. \quad (4.12)$$

The error of the shift-plus-increase is 0.33 (33%), indicating that the shift-plus-increase captures all but a third of the modeled response.

The change in total rainfall captured by the shift-plus-increase is the same as the increase portion itself, $0.9 \% \text{K}^{-1}$. The model response of total rainfall is $1.5 \% \text{K}^{-1}$,

Table 4.1: The shift and increase in response to CO₂ doubling in CMIP5 model simulations, along with the error of the fit. (left) Fit to the multi-model mean response and (right) average of the fits to each model’s response. Shifts, increases, and ΔP have units of % K⁻¹, where changes are normalized by the global-mean surface air temperature change. The error is the absolute value of the difference in rain amount normalized by the target change in rain amount.

Region	Change in model mean			Mean of model changes			Actual ΔP (% K ⁻¹)
	Shift (% K ⁻¹)	Inc (% K ⁻¹)	Error	Shift (% K ⁻¹)	Inc (% K ⁻¹)	Error	
Global	3.3	0.94	0.33	3.3	1.1	0.49	1.5
Sea	3.1	0.94	0.36	3.1	1.0	0.52	1.4
Land	3.5	0.86	0.49	3.7	0.99	0.53	1.8
Extra-tropics	4.0	1.3	0.34	3.9	1.3	0.36	1.9
Tropics	2.9	0.56	0.43	3.1	0.78	0.50	1.2

which is larger. The missing rainfall occurs at heavy and light rain rates. Of the total error, 52% comes from the missing rain falling at rates of at least 40 mm d⁻¹, and 25% comes from the missing rain falling at rates below 2.5 mm d⁻¹.

We can also calculate the optimal shift-plus-increase for each model’s response to CO₂ forcing. The responses for each model, along with their shift-plus-increase fits, are shown in Fig. 4.6. Most, but not all, models share the increase in rain amount at high rain rates and decrease at lower rain rates. The increase mode ranges from 0.3 to 2.4 % K⁻¹. The shift mode ranges from 5.8 to -0.16 % K⁻¹. Errors of the fit range from 14 to 93%. The average of the model responses, along with the multi-model mean, are listed in Table 4.1.

For some models, the shift-plus-increase fits the response quite closely. For other models, some aspects of the model response are captured, while others are not. In two models, the shift-plus-increase does not resemble the model response at all. Models with larger shifts have smaller error (Figure 4.7).

Instead of fitting the increase, we can simply use the total rainfall change as the increase. This forces the entire increase in rainfall to occur evenly across the

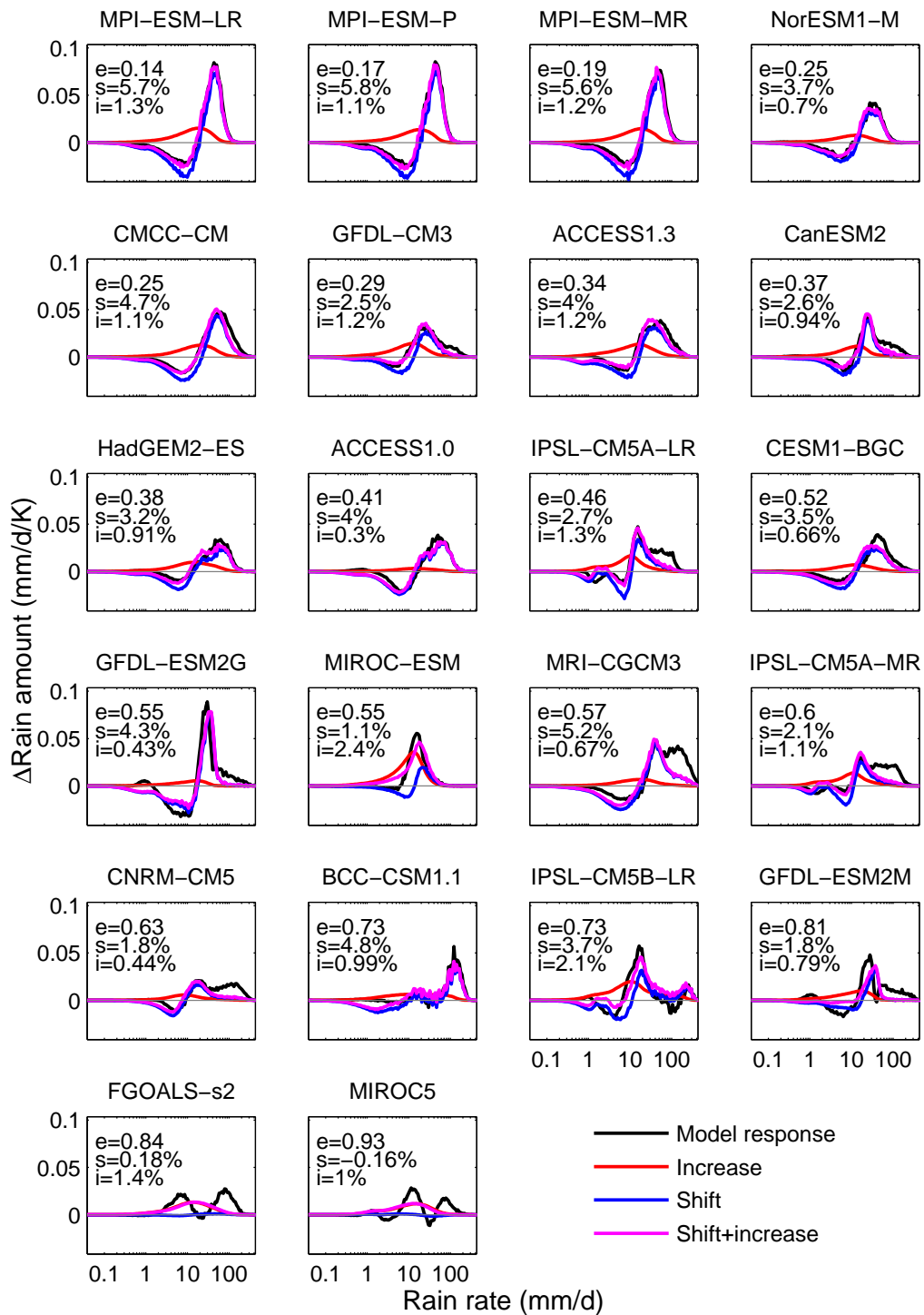


Figure 4.6: Rain amount response to CO₂ doubling for each CMIP5 model and its shift, increase, and shift-plus-increase fit. At top left error (e), shift (s) and increase (i) are listed. Models are ordered from smallest to largest error. As in Fig. 4.5.

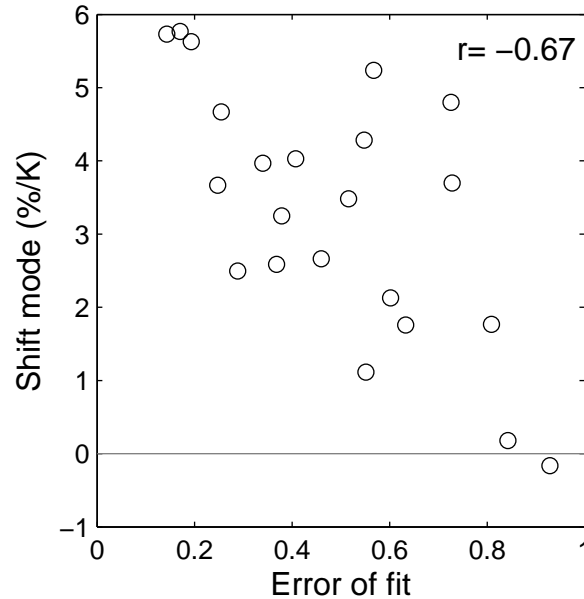


Figure 4.7: Magnitude of shift mode ($\% \text{ K}^{-1}$) versus error of the fit (unit-less fraction). The correlation is at the top right.

distribution. Then, we can do a one-parameter fit of only the shift. This makes no qualitative difference on the magnitude of the shift, but increases the error of the multi-model mean fit and most of the model fits.

For all but two models, the fitted increase is smaller than the model's total rainfall change (Figure 4.8). One explanation is that only some of the change in total rainfall occurs as a mode of change of the whole distribution. The rest occurs as a change isolated at light or heavy rain rates, and unrelated to the changes across the rest of the distribution. We will return to this missing rainfall in Section 4.4.

There is reason to expect that the Tropical and Extra-tropical precipitation distributions could respond differently. Studies of extreme precipitation find that Extra-tropical precipitation change is more readily decomposed into thermodynamic and dynamic components than Tropical precipitation (e.g., O'Gorman and Schneider, 2009a). Table 4.1 shows fits of both shift and increase parameters to the Tropical

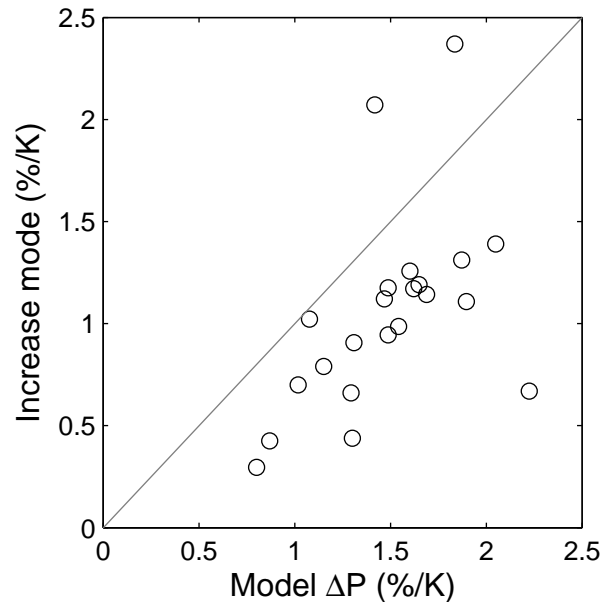


Figure 4.8: Global-mean precipitation increase versus magnitude of the increase mode for each model ($\% \text{ K}^{-1}$). The gray line shows the 1:1 relationship.

and Extra-tropical regions in each model (split at 30 degrees). The fit has lower error in the Extra-tropics than the Tropics. The Extra-tropics generally have a bigger increase (1.3 \% K^{-1}) and bigger shift (4.0 \% K^{-1}), while the Tropics have a smaller increase (0.6 \% K^{-1}) and shift (2.9 \% K^{-1}). We will return to the difference between the Tropics and Extra-tropics in Section 4.4.1.

Unlike the differences between Tropics and Extra-tropics, the differences between land and sea are modest. The land has a slightly larger shift (3.5 \% K^{-1}) than sea (3.1 \% K^{-1}), while both have an increase of 0.9 \% K^{-1} .

So far we have shown that in some CMIP5 models forced by CO_2 doubling, the distribution of rain amount shifts to higher rain rates by 3.3 \% K^{-1} and increases by 0.9 \% K^{-1} . This reasonably fits the change in much of the distribution of rain amount. In Section 4.4, we will discuss how the increase and shift modes fit the rain frequency response. In the next section, we look at changes in the rain amount distribution in

response to ENSO phases.

4.3.4 *Response to ENSO phases*

In this section, we ask: Are the shift and increase in the rain amount distribution a good model for observed rainfall change? Gridded daily observational precipitation datasets only go back to 1997, so at present we would not expect to see statistically significant global trends in rain frequency or rain amount in observations. Instead of looking at trends, we explore the response of tropical rain to ENSO. We look at changes in Tropical (30 S - 30 N) precipitation in the GPCP 1DD and TRMM 3B42v7 datasets (described in Section 4.2) composited over warm and cold phases of ENSO. Unlike the response to CO₂ forcing, the response to ENSO can be studied in both observations and models. So we can also ask whether model changes are similar to the observed changes. We analyze the response to ENSO in AMIP experiments from the CMIP5 simulations.

Figure 4.9 shows the difference between warm and cold ENSO rain amount distributions (along with the fitted shift and increase modes) for the two sets of observations as well as the multi-model mean. As was the case for the model response to CO₂ doubling, the difference in rain amount distribution crosses zero near the peak of the climatological rain amount distribution, with a local maximum at high rain rates and minimum at lower rain rates. This is consistent with Allan and Soden (2008), though they looked at changes as a function of percentile of the cumulative frequency distribution.

Table 4.2 lists the shift, increase, error, and total rainfall response for each case. In all cases, the shift and increase fit the response to ENSO phase within the uncertainty at most rain rates. Figure 4.10 shows the magnitude of the shift and increase modes over the whole Tropics, sea, and land. Over land, the shift and increase closely fit the rain amount response in all cases. Both observational datasets and the AMIP models show a large negative increase mode of 25-26 % K⁻¹ over land, which is slightly

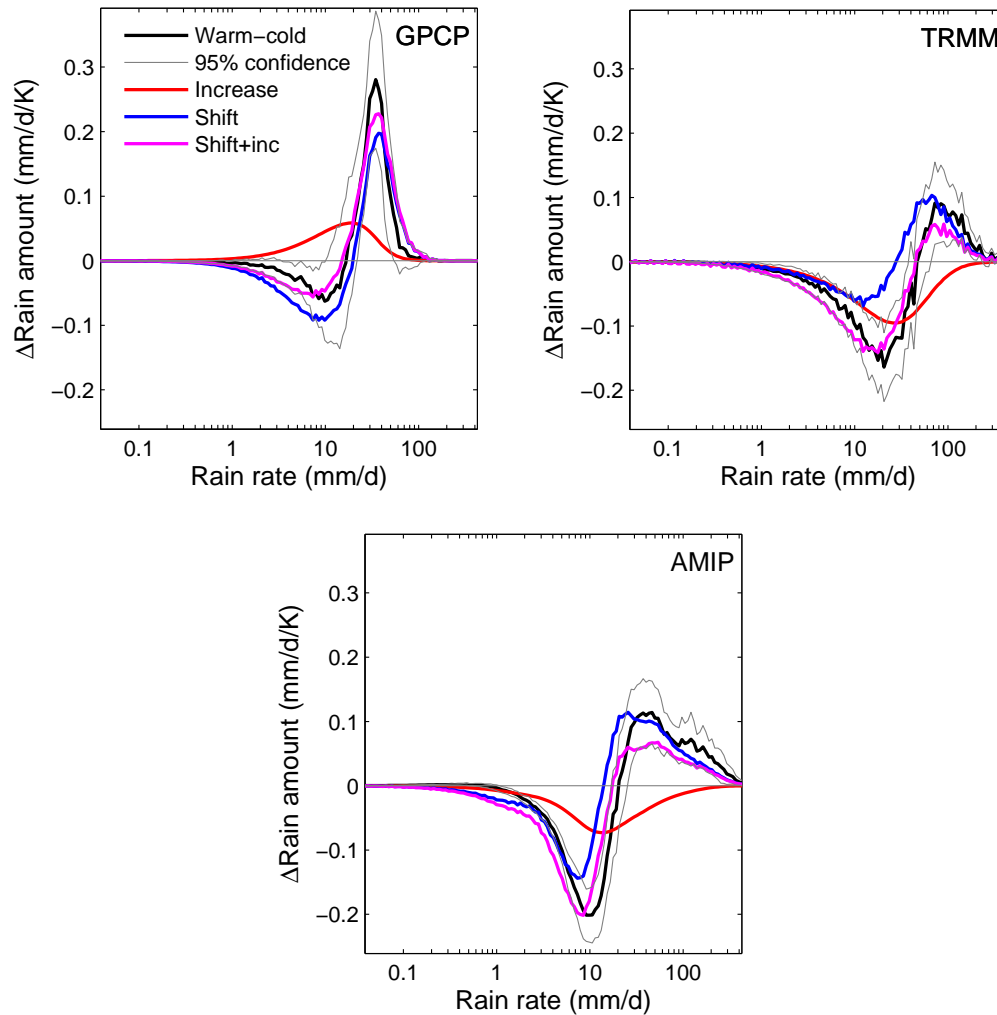


Figure 4.9: Rain amount response in the Tropics to ENSO phases in (top left) GPCP, (top right) TRMM 3B42, and (bottom) AMIP models. Warm minus cold ENSO precipitation from GPCP 1DD over the Tropics (30 N-S). Gray lines show 95% confidence interval of the change according to the difference-of-means test on the observations. As in Fig. 4.5.

Table 4.2: The shift and increase in response to ENSO phases for GPCP and TRMM observations and AMIP model simulations, along with the error of the fit and the change in mean precipitation. For the AMIP simulations, both the fit to the multi-model mean and the average of the fit to each model are shown. Shifts, increases, and ΔP have units of $\% \text{ K}^{-1}$. Temperature changes are taken from tropical average HadCRUT4 for observational datasets and surface air temperature for models.

Dataset	Shift ($\% \text{ K}^{-1}$)	Inc ($\% \text{ K}^{-1}$)	Error	ΔP ($\% \text{ K}^{-1}$)
Whole Tropics				
GPCP	14	6.8	0.31	6.1
TRMM	14	-7.8	0.21	-6.1
AMIP-mean of models	15	-4.7	0.51	-1.8
AMIP-MMM	15	-5.2	0.49	-1.8
Sea				
GPCP	20	19	0.21	17
TRMM	18	-0.85	0.17	-0.92
AMIP-mean of models	20	2.0	0.48	3.9
AMIP-MMM	22	1.2	0.31	3.8
Land				
GPCP	-3.6	-26	0.30	-22
TRMM	-5.7	-25	0.24	-22
AMIP-mean of models	-3.3	-25	0.42	-21
AMIP-MMM	-4.5	-24	0.32	-21

larger than the decrease in total rainfall (on which the datasets, both observations and models, also agree). The datasets also agree on a shift of rain amount to lighter rain rates, ranging from -3.3 to -5.7 $\% \text{ K}^{-1}$. Most of the response to ENSO phase over land is a decrease in rain amount.

Over the ocean, the observational datasets disagree on the response in total rainfall. Interannual variability over the ocean in the previous version of TRMM, version 6, was different from other observational datasets (both GPCP and satellite) (Liu and Allan, 2012). As a result of the difference in the total rainfall response, the observational datasets disagree on the sign of the change of increase mode over ocean. TRMM has a decrease of 6.1 $\% \text{ K}^{-1}$, while GPCP has an increase of 6.1 $\% \text{ K}^{-1}$.

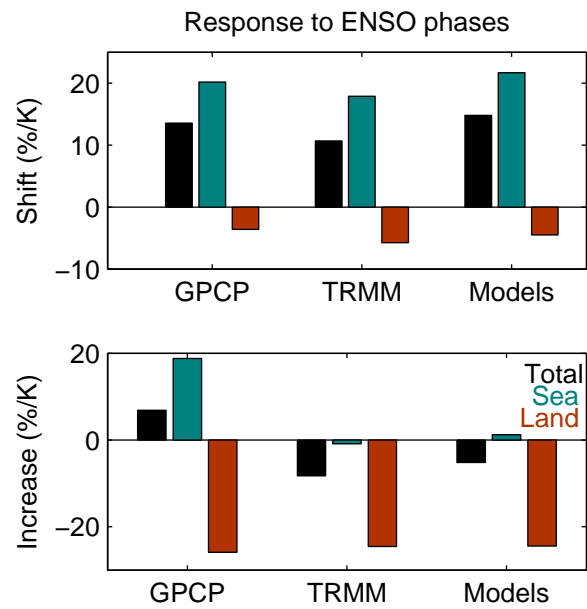


Figure 4.10: The shift (top) and increase (bottom) modes fit to the response to ENSO phases in GPCP (left) and TRMM (center) observations and AMIP models (right). Units are $\% K^{-1}$. The fit to the whole Tropics (black), ocean (green), and land (brown) are included.

AMIP models fall in between the two, with 1.8 \% K^{-1} of decrease. ENSO occurs over inter-annual timescales, which are short enough that the atmospheric energy budget may not be in balance, so there is not necessarily an energetic constraint on the total rainfall over ENSO phases.

The observational datasets and AMIP models agree on a shift between 18 and 22 K^{-1} over ocean, despite the disagreement in total rainfall response. The rain amount response to ENSO is dominated by a shift to higher rain rates in both observational datasets and models.

The response to ENSO phases differs from the response to increasing CO_2 . Figure 4.11 compares the magnitude of the shift and increase fit to the modeled responses to CO_2 increase and ENSO phases. The differences between land and ocean in response to CO_2 increase are much smaller than the differences in response to ENSO phases. The magnitude of the shift is much bigger in response to ENSO (15 \% K^{-1}) than in response to CO_2 increase (3.3 \% K^{-1}) for the total area and over the ocean. Finally, the increase mode has a larger magnitude in the model response to ENSO phases.

It is remarkable that the shift and increase fit the rain amount response to ENSO phases in both observations and models. Next we consider the implications of the shift and increase on the change in the frequency distribution, first considering the entire distribution and then focusing on extreme events.

4.4 Implications for changes in frequency distribution

Figure 4.12 shows the change in rain frequency in the CMIP5 multi-model mean, along with the fitted shift and increase modes, and the shift-plus-increase. In the model response, the decrease in rain frequency is largest at moderate rain rates, though all rain rates lower than the peak of the rain amount distribution have a decrease in rain frequency. The multi-model mean change in dry-day frequency in models is $0.26 \pm 0.17 \text{ \% K}^{-1}$.

The shift mode has the largest decreases in frequency at light rain rates, around

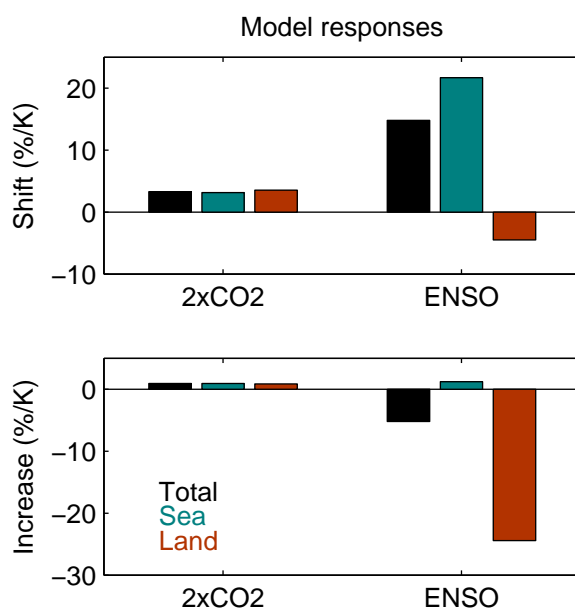


Figure 4.11: The shift (top) and increase (bottom) modes fit to the global response to CO_2 increase (left) and Tropical response to ENSO phases (right) in the CMIP5 multi-model mean. Units are $\% \text{ K}^{-1}$. The total (black), ocean (green), and land (brown) are included.

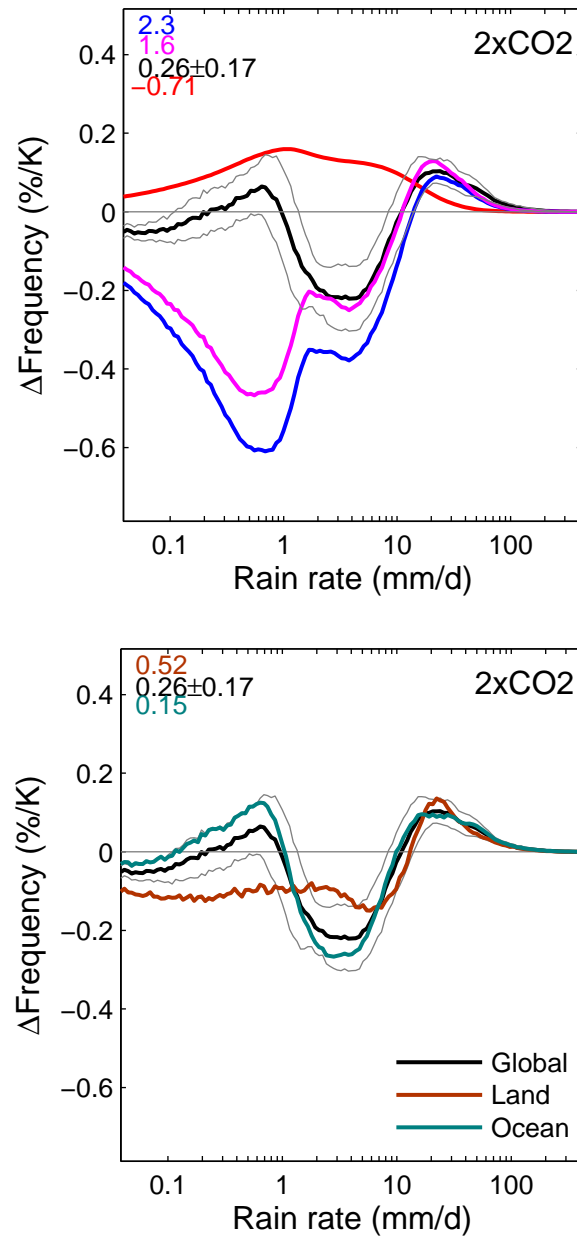


Figure 4.12: Rain frequency response to CO_2 doubling in CMIP5 models ($\% \text{ K}^{-1}$), with change in dry-day frequency noted at the top left. (left) As in Fig. 4.5, the multi-model mean response (black), increase (red), shift (blue), and shift-plus-increase (magenta) are shown. Land (brown), ocean (green), and global (black) rain frequency response.

1 mm d⁻¹. But instead of a large decrease in the frequency of light rain, the models have an increase. This light rain mode accounts for some of the total rainfall increase that is not present in the shift-plus-increase. But as we saw in Fig. 4.1, light rain makes up only a small fraction of the total rainfall. The shift-plus-increase has a 1.6 % K⁻¹ increase in dry-day frequency. The difference in dry-day frequency response between models and the shift-plus-increase is probably related in part to the increase in frequency of light rain. Because the integral over the frequency distribution must sum to one, differences in frequency response at one rain rate must be balanced by differences of the opposite sign at another rain rate. The larger increase in dry-day frequency of the shift-plus-increase compared to the model response is balanced by the large decrease at light rain rates (which is due to the light rain mode).

The land and ocean multi-model mean change in rain frequency are also shown in Fig. 4.12. The peak at high rain rates is similar for land, ocean, and the global mean. But the peak at light rain rates is different: it occurs entirely over the ocean. Over land, rain frequency decreases at all but the highest rain rates. As discussed in Section 4.3.3, the increase in light rain over ocean makes only a small contribution to the change in rain amount distribution, so it is relatively unconstrained by changes in atmospheric cooling.

Table 4.3 lists the change in dry-day frequency for the Extra-tropics and Tropics in model simulations and predicted by the shift-plus increase for CO₂ doubling experiments. Just as in the global mean, in all regions model simulations show much smaller increases, of 0.15-0.52 % K⁻¹, while the shift-plus-increase predicts increases in dry-day frequency of 1-2 % K⁻¹. The total rain frequency changes less than the shift-plus-increase predicts, even over land where there is no light rain mode.

Table 4.4 lists the modeled, observed, and shift-plus-increase-predicted dry-day frequency response to ENSO phases in AMIP model experiments and GPCP and TRMM observational datasets. The response to ENSO phases is much larger than the global (and Tropical) response to CO₂ doubling. Dry-day frequency increases

Table 4.3: Dry-day frequency ($\% \text{ K}^{-1}$) and 99.99th percentile rain rate ($\% \text{ K}^{-1}$) responses to CO_2 doubling. The average model response is shown, along with the average of fitted responses, for various geographical regions. The standard deviation of the 99.99th percentile rain rate response is also included.

Region	$\Delta R_{99.99}$ ($\% \text{ K}^{-1}$)			Δf_d ($\% \text{ K}^{-1}$)	
	Fit	Actual	std	Fit	Actual
Global	2.9	8.4	5.8	1.5	0.26
Sea	2.9	8.7	7.2	1.5	0.15
Land	3.1	8.7	3.9	1.3	0.52
Extra-tropics	3.5	6.5	1.7	1.8	0.22
Tropics	2.9	8.7	6.3	1.4	0.29

in AMIP models, both observational datasets, and from the shift-plus-increase in all regions except for GPCP over ocean. In nearly all cases, the shift-plus-increase dry-day frequency response is much bigger than the modeled or observed change, just as for to the modeled response to CO_2 doubling.

4.4.1 Extreme events

In this section we take a closer look at changes in extreme precipitation. Figure 4.13 shows the percent change in rain rate as a function of percentile of the cumulative frequency distribution for the multi-model mean response to increased CO_2 . Table 4.3 lists the rain rate response at the 99.99th percentile for the global-mean, as well as the geographic divisions introduced earlier. As in Allen and Ingram (2002) and Pall et al. (2007), we find a decrease in rate rate below the 90th percentile, and increases above the 90th percentile in the multi-model mean response to CO_2 doubling. The percentage increase in rain rate goes up with the percentile. At the 99.9th percentile, the increase is $4.9 \% \text{ K}^{-1}$, consistent with O’Gorman and Schneider (2009a), though they looked at zonal-mean changes in CMIP3 models. At the 99.99th percentile, the increase in rain rate is $6.9 \% \text{ K}^{-1}$.

The shift-plus-increase, which was fit to the rain amount distribution, has some

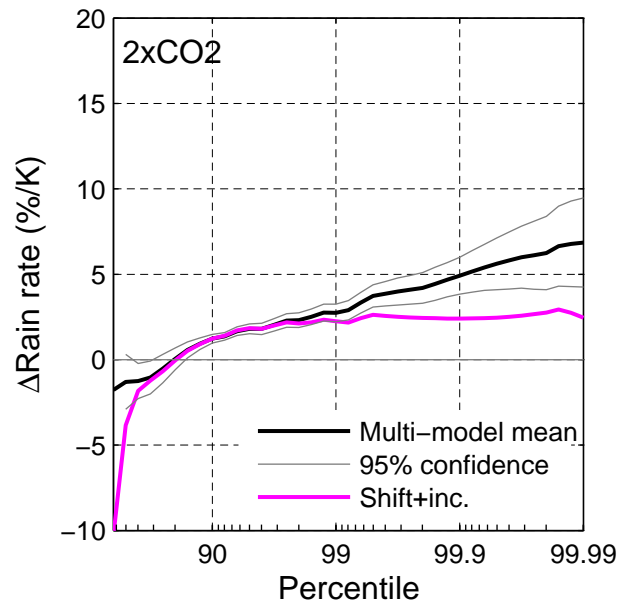


Figure 4.13: Extreme precipitation response ($\% K^{-1}$) for CMIP5 multi-model mean CO_2 doubling (black) and the shift-plus-increase (magenta). Percent change in rain rate per degree warming by percentile of the cumulative frequency distribution. Gray lines show 95% confidence of the multi-model mean response.

Table 4.4: Dry-day frequency ($\% \text{ K}^{-1}$) and 99.99th percentile rain rate ($\% \text{ K}^{-1}$) responses to ENSO phases in GPCP and TRMM observations and AMIP model experiments. The “Fit” is from the fitted shift-plus-increase, while “Actual” indicates from the models or observational dataset. For models, the average of model responses is shown.

Dataset	$\Delta R_{99.99}$ ($\% \text{ K}^{-1}$)		Δf_d ($\% \text{ K}^{-1}$)	
	Fit	Actual	Fit	Actual
Whole Tropics				
GPCP	11	4.0	2.5	1.4
TRMM	8.7	12	12	4.8
AMIP-mean of models	10	15	14	2.1
Sea				
GPCP	15	6.0	-0.03	0.60
TRMM	12	14	10	5.3
AMIP-mean of models	14	17	14	2.1
Land				
GPCP	-8.3	1.5	8.8	3.8
TRMM	-13	-1.4	9.1	3.4
AMIP-mean of models	-10	-1.1	12	1.9

similarities to but also some differences from the modeled response. The shift-plus-increase is the sum of the increase and shift modes (the shape of which are shown in the bottom panels of Fig. 4.4). Below the 90th percentile, the shift-plus-increase crosses from negative to positive. Negative extreme rain rates indicate a decrease in the rate of light rain events, which is due to the shift. Between the 90th and 99th percentiles, the shift-plus-increase flattens with continued increase in percentile. All events beyond the 99th percentile increase between 3 and 4 $\% \text{ K}^{-1}$, in contrast to the continued increase with percentile of the model response. The shape of this part of the shift-plus-increase depends on the magnitude of the shift and increase modes as well as the shape of the initial rain frequency distribution.

Figure 4.14 shows each model’s change in rain rate as a function of percentile along with its fitted shift-plus-increase. There are two types of model responses: those that increase by a similar percentage for all extreme precipitation (beyond the

99th percentile), and those that increase most at the most extreme percentiles. The responses with similar increases for all extreme percentiles are well-captured by the shift-plus-increase. In contrast, responses that increase most at the most extreme percentiles are not captured. We'll call this uncaptured response the *extreme mode*. Other studies have also shown the model responses fall into two camps. Sugiyama et al. (2010) found that extreme precipitation increased by more than water vapor in half of CMIP3 model simulations.

The Tropics have a slightly larger increase in rain rate at the 99.99th percentile, $8.7\% \text{ K}^{-1}$, than the Extra-tropics, $6.5\% \text{ K}^{-1}$. However, models agree much more closely on the Extra-tropical response than on the Tropical response. In the Tropics, the standard deviation of the 99.99th percentile rain rate response across models is $6.3\% \text{ K}^{-1}$, while in the Extra-tropics it is just $1.7\% \text{ K}^{-1}$. Previously, O’Gorman and Schneider (2009a) found that Extra-tropical extreme precipitation change follows the moisture convergence scaling law more closely than Tropical change. In Section 4.3.3, we saw that in the Extra-tropics, the shift mode was bigger and the error of the shift-plus-increase was smaller than in the Tropics. The difference in shift mode, error, and extreme rain are consistent with a bigger extreme mode response in the Tropics than in the Extra-tropics. We will consider the differences across models more in Section 4.5.

Land and ocean could be expected to have different responses for physical reasons (Trenberth, 2011). Figure 4.15 shows the multi-model mean response to CO_2 doubling over land. It is very similar to the total response, except for somewhat better agreement among models than for the global response. The inter-model standard deviation of 99.99th percentile increase is $7.2\% \text{ K}^{-1}$ over ocean, and $3.9\% \text{ K}^{-1}$ over land.

Now we turn to observations: How does observed Tropical extreme precipitation respond to ENSO, and do models capture the observed changes? The response of extreme precipitation to ENSO phases in both observational datasets is shown in

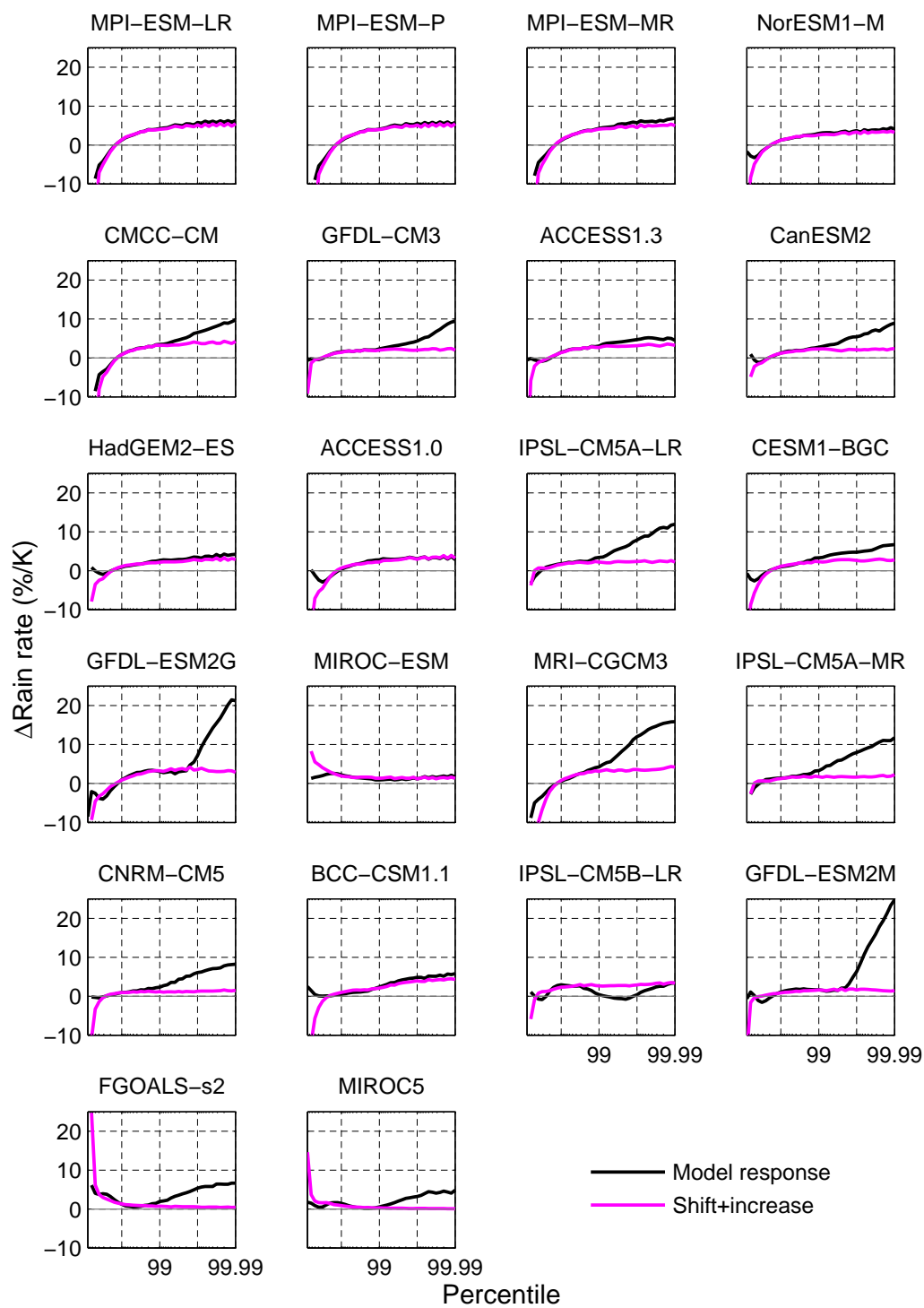


Figure 4.14: Extreme precipitation response ($\% \text{K}^{-1}$) to CO_2 doubling in each CMIP5 model (black) and its shift-plus-increase (magenta). As in Fig. 4.13.

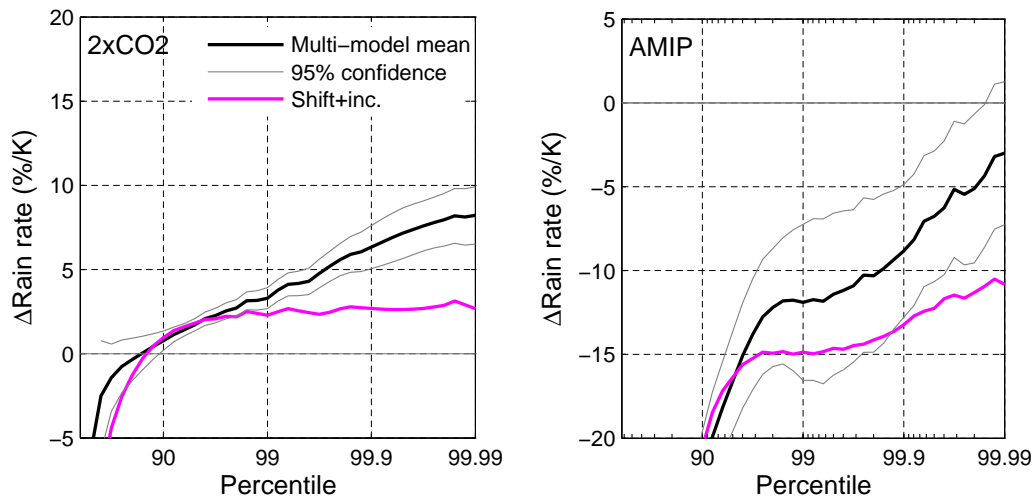


Figure 4.15: Change in extremes over land in models in response to CO_2 doubling (left) and ENSO (right). As in Fig. 4.13.

Fig. 4.16. All datasets and the fitted shift-plus-increases show increases in extreme events beyond the 99th percentile in the Tropical mean. At the 99.99th percentile, the increases are highest in AMIP models ($19 \% \text{ K}^{-1}$), followed by TRMM ($12 \% \text{ K}^{-1}$), and then GPCP ($5 \% \text{ K}^{-1}$). At the 99th percentile, GPCP (at $10 \% \text{ K}^{-1}$) has more increase than TRMM ($5 \% \text{ K}^{-1}$), while AMIP is similar to GPCP ($10 \% \text{ K}^{-1}$). Up to the 99th percentile, the shift-plus-increase is within the uncertainty in each observational dataset. At the 99.9 and 99.99th percentiles, the shift-plus-increase underestimates the increase for AMIP models.

The change in extreme precipitation over ocean follows the same pattern as the whole Tropics. The multi-model mean response over land in AMIP experiments is shown in Figure 4.15. GPCP and TRMM responses over land are similar to the AMIP response. Unlike for CO_2 doubling, the response of extreme rain rate over land is very different from the total response. The shift-plus-(de)crease predicts a decrease in rain rate at nearly all percentiles in both observational datasets and AMIP experiment. The only exception is that in GPCP, the most extreme percentiles do

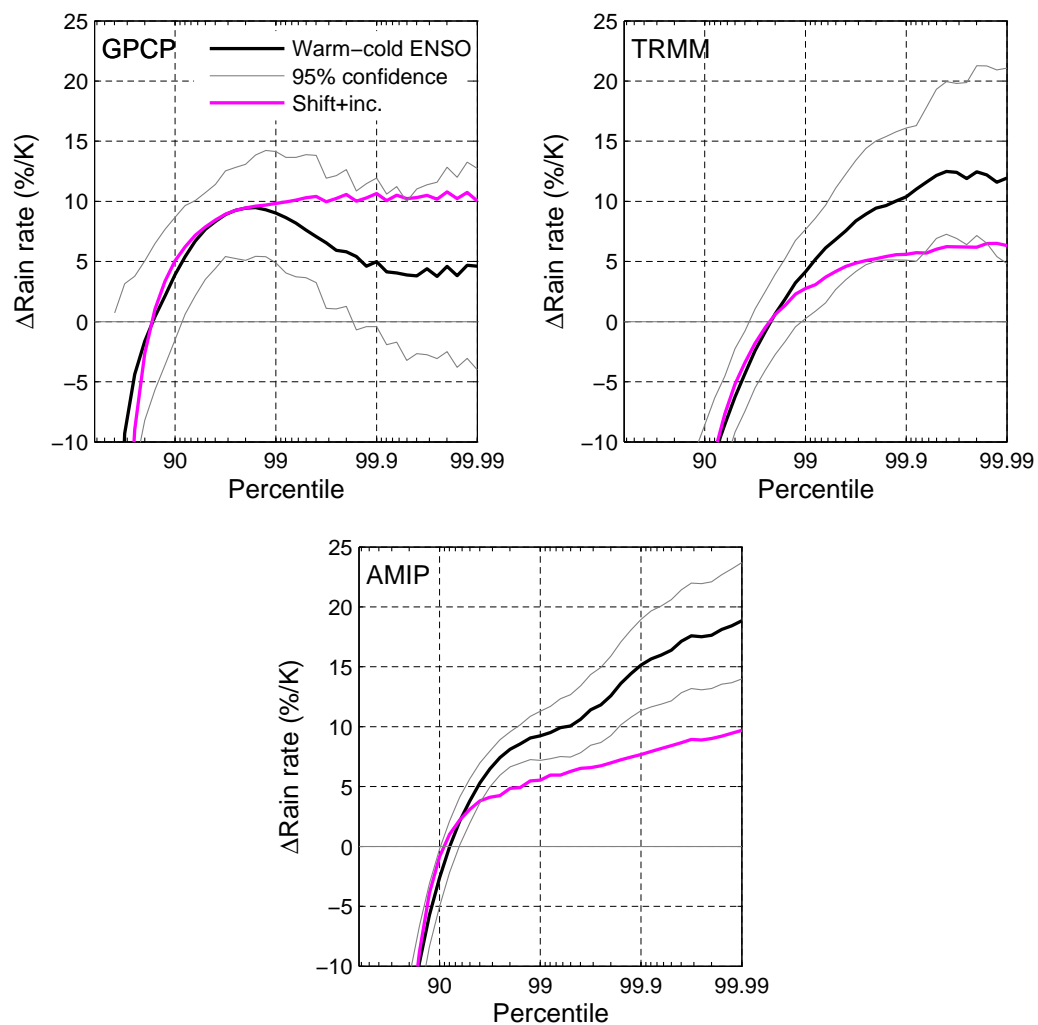


Figure 4.16: Extreme precipitation response ($\% \text{ K}^{-1}$) to ENSO phases in AMIP models and GPCP and TRMM observations. As in Fig. 4.13.

not show significant change. The shift-plus-increase predicts a larger decrease in rain rate at all percentiles beyond the 99th in all datasets over land. The models agree less over land than over ocean, unlike in response to CO₂ doubling. The standard deviation of the 99.99th percentile rain rate response is 16 % K⁻¹ over land and 10.8 % K⁻¹ over ocean. For the entire Tropics, the standard deviation among models is lower than for either land or ocean, at just 9.0 % K⁻¹. This is consistent with shifting of rain (spatially) from land to ocean resulting in some compensation across models.

The increase in extreme precipitation implied by the shift-plus-increase is tightly tied to the magnitude of the shift mode. The response of the 99.99th percentile rain rate in AMIP models, observations, and for the shift-plus-increase is compared in Table 4.4. The finding that the shift is much greater for changes during ENSO events than for the response to CO₂ doubling (by a factor of at least 4) is consistent with the finding that the sensitivity of 99.9 percentile precipitation is 2.5 times greater for inter-annual variability than for increases expected over the next century in models (O’Gorman, 2012). Allan et al. (2013) also found muted increase of extreme precipitation for climate change relative to inter-annual variability.

4.5 Differences across models

Why does the extreme rain rate response to CO₂ doubling follow the shift-plus-increase so closely in some models, but increase much more in other models? In this section we focus on a subset of models to explore the extreme mode behavior in more detail.

4.5.1 Resolved and unresolved rain events

Convective parameterizations are an important difference between models, and they are important for modeled rainfall. Climate models form rain in two ways. When the relative humidity of a grid box reaches 100%, the model produces grid-scale (or large-scale) precipitation. When a grid box is below saturation, the convective param-

eterization produces precipitation, which represents the rain coming from unresolved motions.

Neither large-scale nor convective precipitation is obviously more realistic than the other. As model resolution increases, more motions are resolved, so more precipitation should be large-scale and less should be convective. Kopparla et al. (2013) showed that increasing model resolution decreased of the bias in extreme precipitation over land compared to observations. Large-scale and convective precipitation are not independent. Lin et al. (2013) showed that when convective precipitation is inhibited, large-scale precipitation increases to compensate. Large-scale and convective precipitation do not correspond to the classification of observed stratiform and convective precipitation types (Held et al., 2007). Mesoscale organization relevant to realistic heavy precipitation is not represented in climate models (Rossow et al., 2013). While large-scale and convective events are comparably realistic (or unrealistic), this division of precipitation is an artifact of modeling, rather than a realistic description of two types of precipitating systems.

Heavy, predominantly large-scale rain events are found in models, and the extent to which they are realistic is unclear. Held et al. (2007) called these grid-point storms. They showed, with idealized simulations of a model related to the GFDL-ESM atmosphere model, that grid-point storms appear above a threshold temperature, and with further warming the amount of rain from grid-point storms increases. The threshold temperature, but not the overall behavior, depends on resolution.

We would like to investigate how resolved (large-scale) and unresolved (convective) precipitation play a role in the model-dependent extreme precipitation response we see. Daily convective precipitation data is available for just eight of the models in the CO₂ doubling experiment. Unfortunately, all of the models with available data for this experiment have increases in extreme rain rate that are much greater than the prediction from the shift-plus-increase. While the CO₂ doubling experiment is clean, free of the effects of differing changes in aerosol forcing precipitation (see Chapter 2

for the impact in CMIP3 experiments), most modeling groups archive both total and convective precipitation at daily timescales for the realistic-forcing RCP8.5 scenario. In the models we examine here, the rain amount distribution response is similar between the RCP8.5 and CO₂ increase experiments.

We focus on just three models to illustrate the different types of extreme rain rate response: MPI-ESM-LR (Giorgetta et al., 2013), IPSL-CM5A-LR (Dufresne et al., 2013), and GFDL-ESM2G (Dunne et al., 2012). These models were chosen because they are clear examples, and most other models fall in between them. Figure 4.17 shows key aspects of the three models' rain amount distributions and responses to realistic forcing in the RCP8.5 experiment: the rain amount distribution compared to coarsened GPCP, the climatological convective fraction as a function of cumulative frequency distribution, the rain amount response to warming (total change simulated by the models, convective precipitation contribution to the total, and the fit by the shift-plus-increase), and the extreme precipitation response.

The MPI-ESM-LR rain amount response to warming is captured most closely of all the models by the shift-plus-increase (Fig. 4.6). Its change in rain amount looks like the ideal shift and increase illustrated partially in Fig. 4.4. It has one of the largest shifts of any model, 5.7 % K⁻¹ (only MPI-ESM-P is higher at 5.8 % K⁻¹). For the CO₂ doubling simulation, its extreme precipitation response is captured very well by the shift-plus-increase (Fig. 4.14). Its extreme precipitation response in RCP8.5 is captured almost as closely. Furthermore, the shape of the rain amount distribution of MPI-ESM-LR matches the coarsened GPCP rain amount distribution very closely compared to most other models.

IPSL-CM5A-LR and GFDL-ESM2G contrasts with the MPI response. The shift-plus-increase only partially captures their response to warming, with errors of 67 and 74%. In both models, the shift-plus-increase captures a dip in rain amount at moderate rain rates, and the increase at rain rates just above this. But it fails to capture increases in rain amount at the highest rain rates. In both cases, these

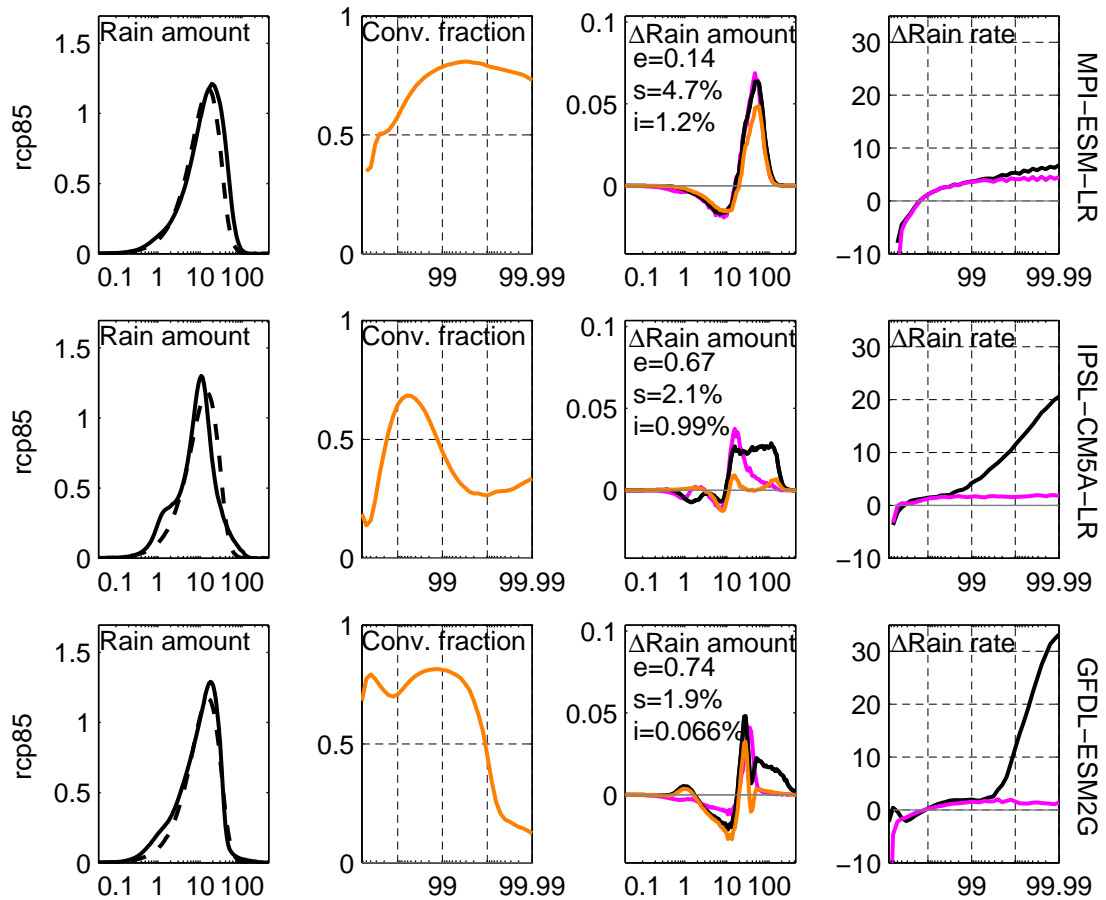


Figure 4.17: MPI-ESM-LR (top), IPSL-CM5A-LR (middle), and GFDL-ESM2G (bottom) model responses. In the rain amount climatology (far left), model distribution (solid black) is shown along with coarsened GPCP (dashed). The climatological convective fraction (center left) is shown alone (orange). In the change in rain amount distribution (center right), the model change (black), shift-plus-increase (magenta), and convective precipitation change (orange) are shown. In the change in extreme rain rate (far right), the model change (black) and shift-plus-increase (magenta) are shown.

additional increases in rain amount look like extra rain has been added to the high side of the distribution (in contrast to the MPI-ESM-LR response). The extreme rain rate response also differs from the shift-plus-increase in these models. GFDL-ESM2G has the largest 99.99th percentile rain rate increase of any model, and the IPSL-CM5A-LR response is among the largest. The shift fit to both of these responses is lower than it is for many models, around 2 % K⁻¹ (it is greater for both models in the CO₂ doubling experiments), but their increases in extreme rainfall far outpace even the largest shift.

How much of the rain amount response is convective rainfall, and how much is large-scale? Measures of convective rainfall were introduced in Section 4.2. The change in the amount of convective precipitation in each rain rate bin is shown in orange in Fig. 4.17. In MPI-ESM-LR, the majority of the change in rain amount is convective. There is just a small difference between convective and total precipitation near the peak of the increase, which is an increase in large-scale precipitation. In contrast, the IPSL-CM5A-LR change in convective rain amount is very small, indicating that most of the change in rain amount is large-scale precipitation. While some of this increase is captured by the shift-plus-increase, much of it is not. The increases at the highest rain rates which are not captured by the shift-plus-increase are changes in large-scale precipitation. In GFDL-ESM2G, there are two peaks at the high end of the rain amount response. The highest peak, at moderate rain rates near 10 mm d⁻¹, is mostly convective rainfall, and is captured by the shift-plus increase. The smaller peak, which is at higher rain rates, is mostly large-scale precipitation, and is not captured by the shift-plus-increase. As in the case of the IPSL model, this uncaptured large-scale increase in rain amount accounts for the large increase in rain rate at the highest cumulative probabilities.

Held et al. (2007) suggested that the sensitivity of grid-point storms in any particular model might be related to the fraction of convective precipitation in the model. Motivated by this, we calculate the climatological fraction of convective precipitation

as a function of cumulative probability distribution in each of the models. In MPI-ESM-LR, rainfall at the 99.99th percentile at the beginning of the 21st Century is about 75% convective, and only 25% large-scale. In IPSL-CM5A-LR, about 30% of 99.99th percentile precipitation is convective, with a majority large-scale above the 99th percentile. In GFDL-ESM2G, less than 20% of the 99.99th percentile rainfall is convective. Large-scale precipitation makes up a majority of the rainfall above the 99.9th percentile. The divergence of the extreme rain rate response from the shift-plus-increase fit in these models occurs around the percentile where large-scale rain fall constitutes a majority. Consistent with control by grid-point storms, the driver of the differences in extreme rain rate response across models is the fraction of the events that occur as large-scale precipitation in the climatological distribution.

We can look at individual heavy events in each of the models. Figure 4.18 shows the rain amount from the top 0.1% of events in the MPI-ESM-LR and GFDL-ESM2G models, as well as GPCP and TRMM observations. In the MPI-ESM-LR model, rain falling from heavy events peaks in the Pacific and Indian oceans off of the Equator, which is consistent with tropical cyclones as important drivers of heavy rain. In GFDL-ESM2G, rain from the heaviest events peaks within the Maritime Continent, closer to land and to the Equator than MPI-ESM-LR. A rain maximum on the Equator is inconsistent with tropical cyclones. In GPCP, rain from the heaviest events falls over land, in contrast to both of the models. But in TRMM, most rain from the heaviest events falls over ocean. Satellite retrievals and availability of gauge measurements differ over land and ocean, which may contribute to the differences between land and sea within each observational dataset.

We choose a region where much of the heavy rain falls for each of the two models, and then choose a day with a 99.99th percentile event from each model. The evolution for an event, from one day the event through five days after, is shown in Figure 4.19 for the MPI-ESM-LR model. Both the rain rate on each day and the convective (unresolved) rain is shown for each model. In the MPI-ESM-LR model, the event

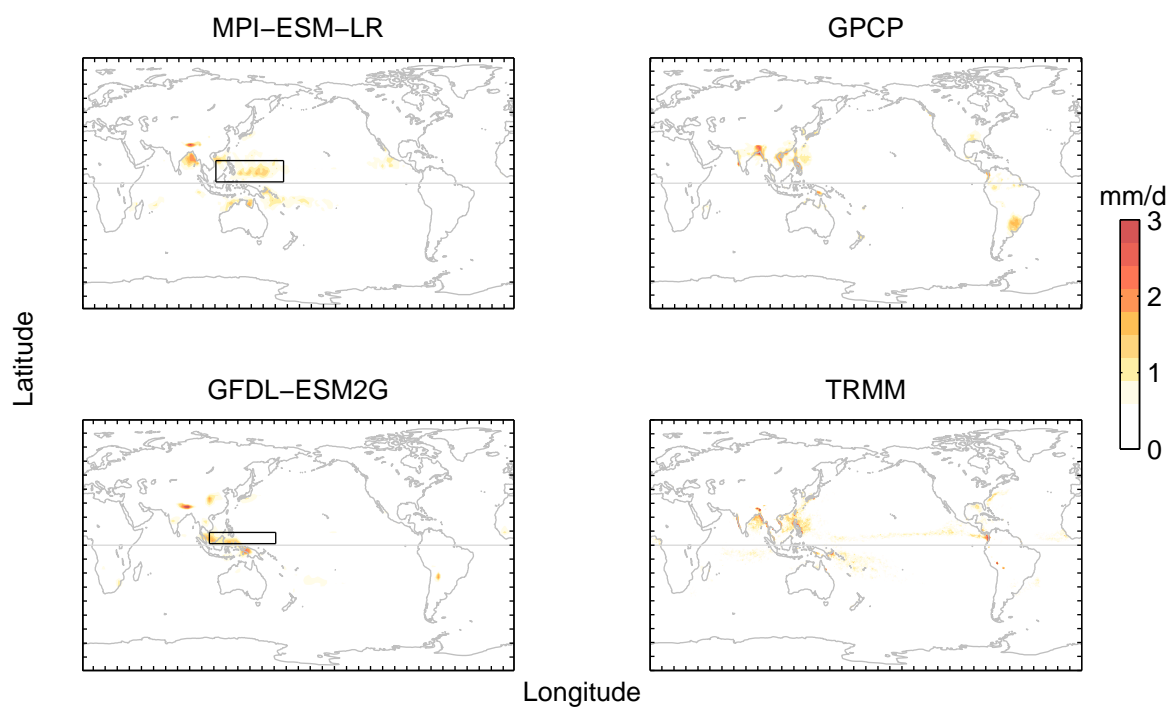


Figure 4.18: Maps of the rain amount (mm d^{-1}) falling in the top 0.1% of events from the first ten years of the RCP8.5 scenario in MPI-ESM-LR (top left) and GFDL-ESM2G (bottom left) model simulations and GPCP (top right) and TRMM (bottom right) observations. Boxes for each model show the subdomain in Figures 4.19 and 4.20.

spans a few grid cells in each direction with similar rain rates. The event persists for six of the seven days of the event shown, with many of the grid points constituting 99.99th percentile events. Notably, most of the rain falls as convective precipitation.

The evolution of a heavy event in the GFDL-ESM2G model is shown in Figure 4.20. The 99.99th percentile event is also part of a system that evolves over a few days. But in this case, just a few grid cells, between one and four, have much larger rain rates than the adjacent grid cells. Furthermore, nearly all of the rain falls as large-scale (resolved) precipitation. This is consistent with the picture of grid point storms from Held et al. (2007).

If grid-point storms account for the difference in extreme rain rate response among the models, and if these storms exhibit increases with temperature as Held et al. (2007) saw in the idealized GFDL model, we should see increases in the response with increased forcing and warming. Figure 4.21 shows the rain amount and extreme rain rate responses to doubling and quadrupling of CO₂ in the transient CO₂ increase experiment for these three models. In all three models, even MPI-ESM-LR, the increases in rain rate at the highest percentiles is larger for quadrupling than for doubling of CO₂, and the portion of the increase not captured by the shift-plus-increase is larger. Furthermore, in all three models, the magnitude of the fitted shift and increase get smaller, while the error of the fit increases.

These changes occur in other models as well. Table 4.5 lists the average of the (22) model responses to 2x, 3x, and 4xCO₂. Just as we saw for the three illustrative models, the following changes are all present with increasing CO₂: the increase in modeled rain rate at the 99.99th percentile, the decrease in fitted shift and increase of rain amount, and the increase in the error of the fit. For all three levels of CO₂ forcing, the total rain amount response is 1.5 % K⁻¹.

Taken together, these tendencies indicate that with increased warming, more of the precipitation increase comes as an increase in large-scale precipitation at very high rain rates and less comes as a change in the rain amount distribution. Less of

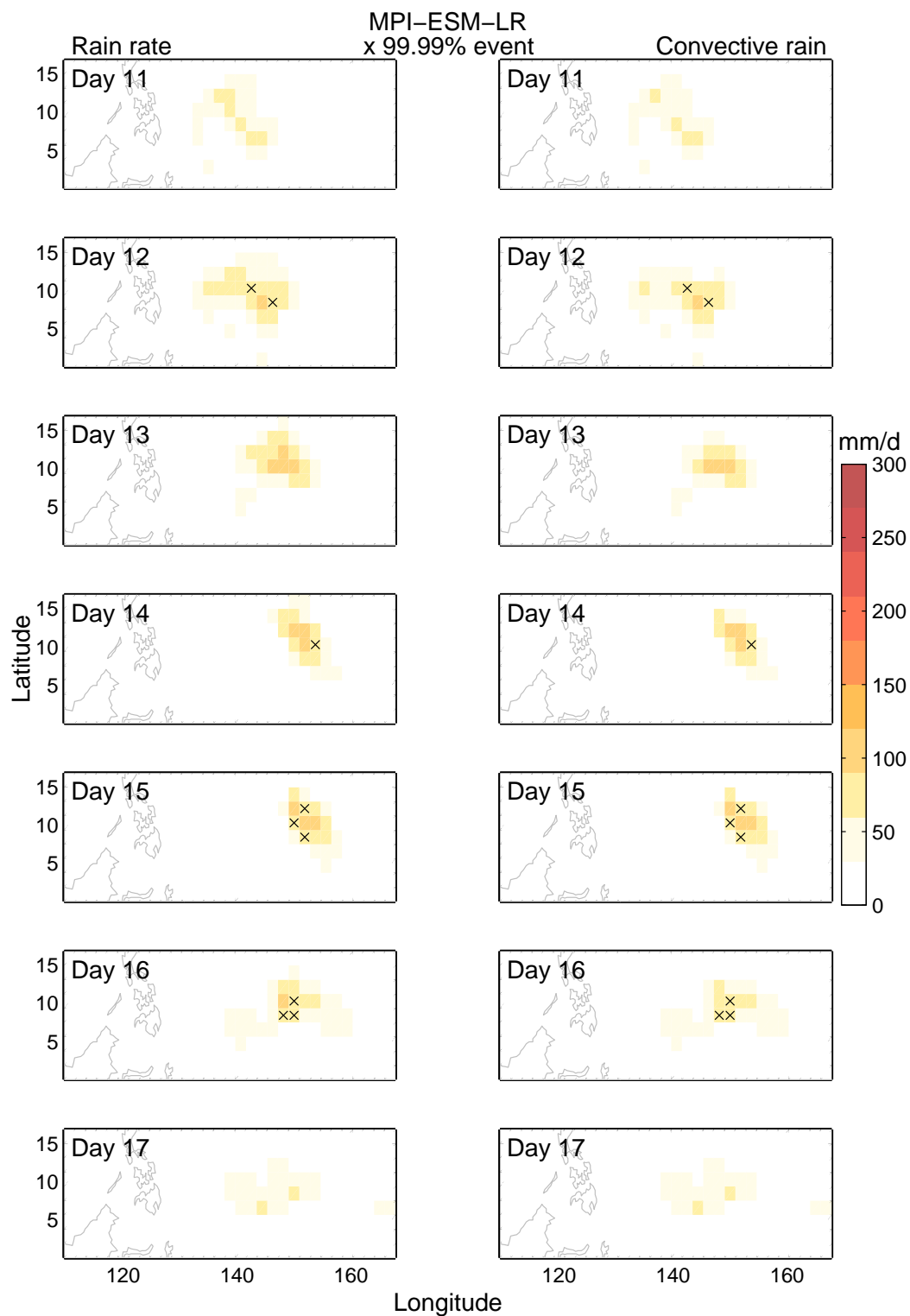


Figure 4.19: Rain rate and convective rain (mm d^{-1}) for a 99.99th percentile event in the MPI-ESM-LR model chosen from the first ten years of the RCP8.5 simulation.

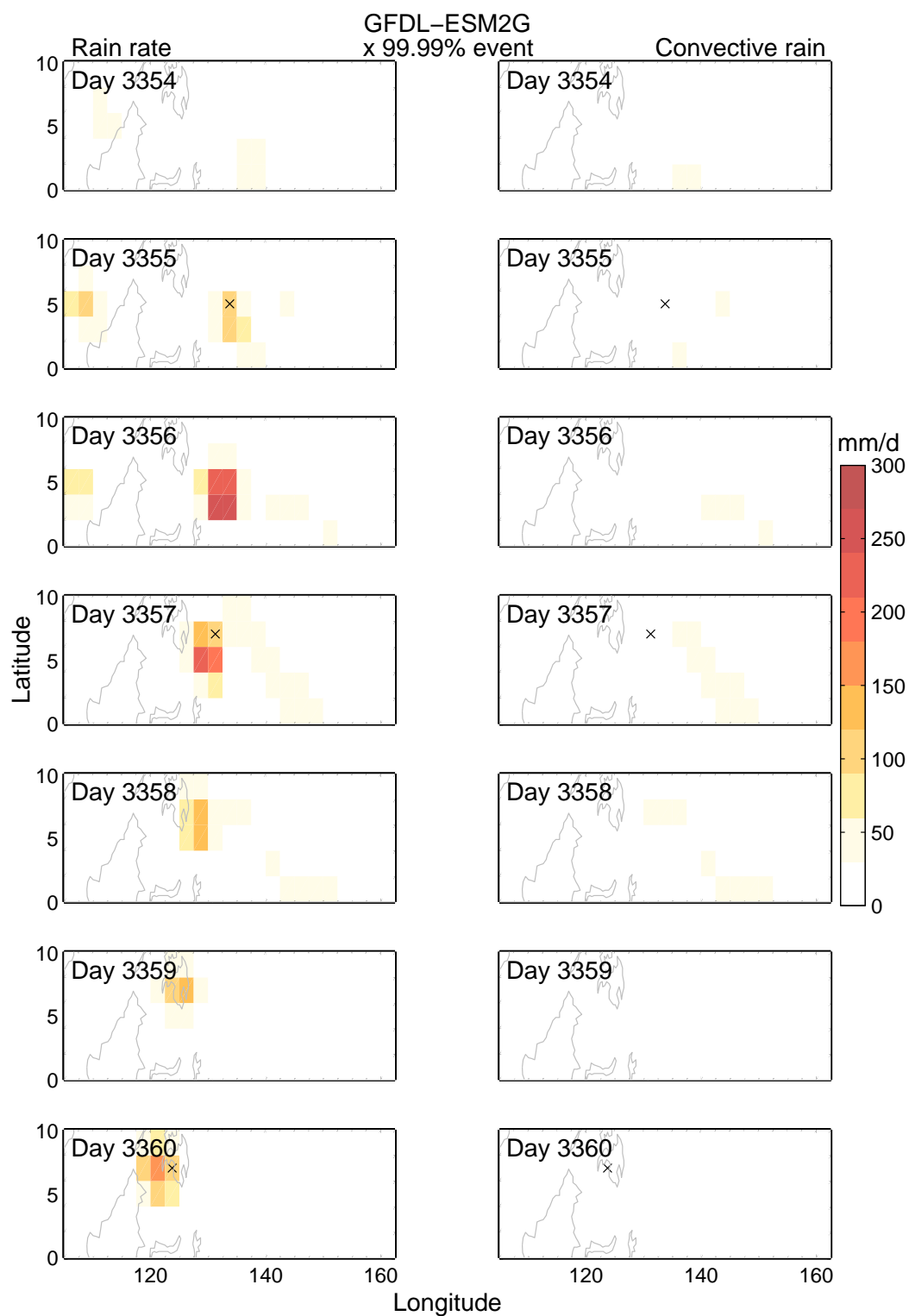


Figure 4.20: Rain rate and convective rain (mm d^{-1}) for a 99.99th percentile event in the GFDL-ESM2G model chosen from the first ten years of the RCP8.5 simulation.

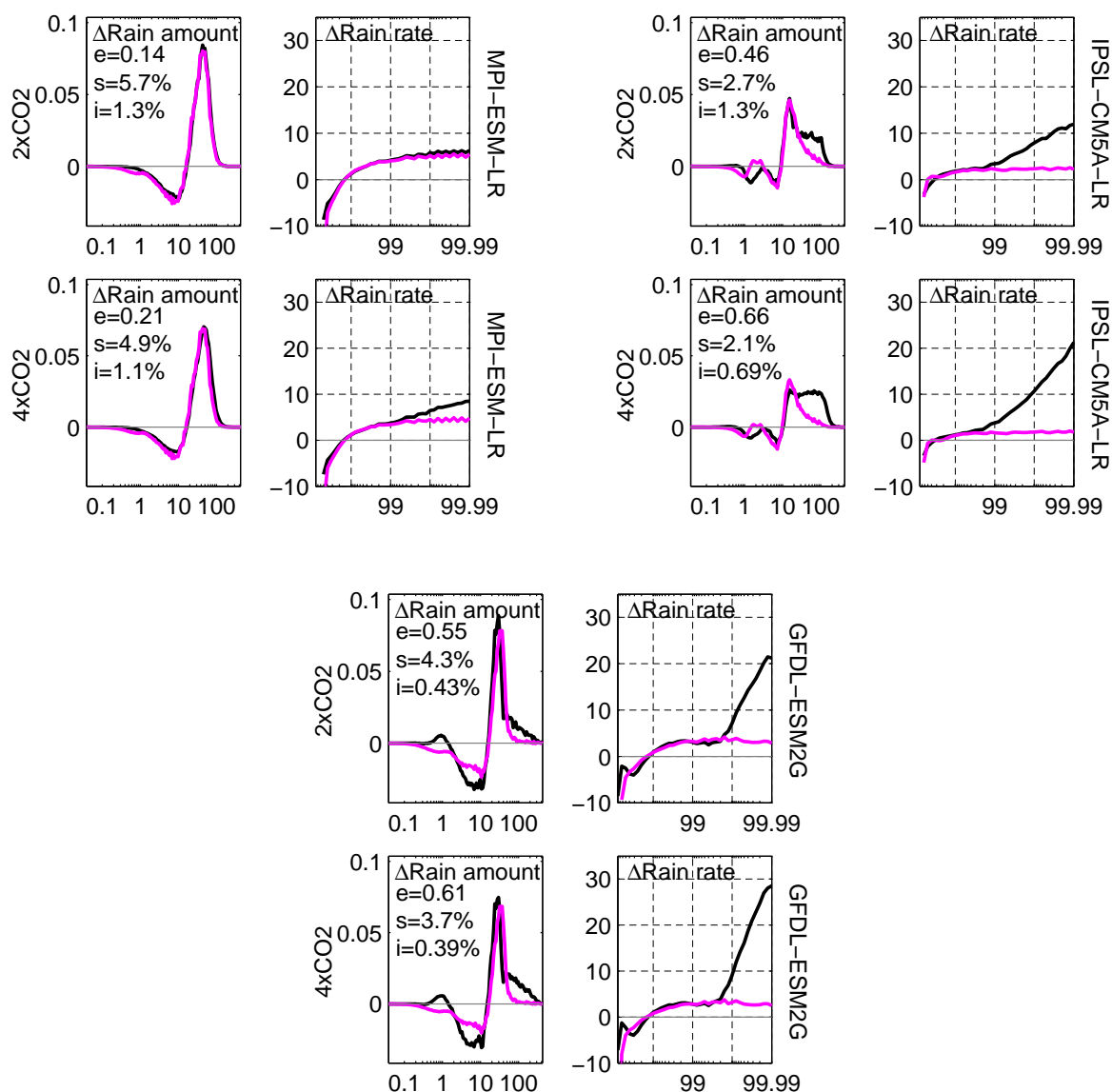


Figure 4.21: MPI-ESM-LR (top left), IPSL-CM5A-LR (top right), and GFDL-ESM2G (bottom) models 2x (top) and 4xCO₂ (bottom) rain amount (left) and extreme rain rate (right) responses. Model response (black) and shift-plus-increase (magenta). Error, shift, and increase are noted in the top left of the rain amount response panels.

Table 4.5: Mean of model responses to CO₂ doubling, tripling, and quadrupling. The units for most variables are % K⁻¹. Exceptions are the global-mean temperature increase ΔT , which has units of K, and the error, which is a unitless fraction.

CO ₂	Fit		Actual	$\Delta R_{99.99}$		Δf_d		Error	ΔT (K)
	Shift (% K ⁻¹)	Inc. (% K ⁻¹)	ΔP (% K ⁻¹)	Fit (% K ⁻¹)	Actual	Fit (% K ⁻¹)	Actual		
2x	3.3	1.1	1.5	2.9	8.4	1.5	0.26	0.49	1.7
3x	3.2	0.94	1.5	2.8	10	1.4	0.24	0.53	3.0
4x	3.0	0.92	1.5	2.6	12	1.3	0.23	0.54	4.1

the total rainfall response is captured by the shift-plus-increase, and more of it is due to rain falling as heavy large-scale precipitation events.

The aspect of the grid-point storms that is not captured by the shift-plus-increase is likely the transition from convective to large-scale events. This transition involves abrupt changes in the rain rate of events, likely driven by large changes in vertical velocity. Studies focusing on the relationship between vertical velocity, moisture changes, and rain rates in extreme precipitation (e.g., O’Gorman and Schneider, 2009b; Sugiyama et al., 2010) assume the changes are linear, which is probably not the case in the transition from convective (or no heavy events) to large-scale grid-point storms (Held et al., 2007).

4.5.2 *Sorting models by comparing their response to ENSO phases with observations*

Can we discern whether some models are more consistent with observations than others by comparing AMIP experiments with observations? O’Gorman (2012) showed that the responses of inter-annual variability and long-term change in each model’s 99.9th percentile precipitation response are related, and used the modeled relationship between inter-annual variability and long-term change to predict the long-term change based on observed variability. For the 14 models analyzed here with simulations for both RCP8.5 and AMIP experiments, the 99.99th percentile response due to 21st

Century climate forcing and ENSO phase are positively correlated, significant at the 90th (but not 95th) confidence level. If the observed response to ENSO phase clearly favored some models over others, we might take that as an indication that those models were closer to reality, and more heavily weight their response to global warming.

A difficulty with this approach is that the two observational datasets disagree about many aspects of the response. They disagree about the sign of the total change in rainfall. They agree on the magnitude of the shift, but disagree about whether the heaviest events should increase at rates greater (TRMM) or less (GPCP) than the shift-plus-increase prediction. But they do agree that the shift is $14 \% \text{ K}^{-1}$. They put a wide margin on the magnitude of the increase at the 99.99th percentile, from -3 to $21 \% \text{ K}^{-1}$ (the bottom of the GPCP range through to high end of TRMM). We use these two measures to sort the models: 99.99th percentile rain rate response within the error bounds of either observational dataset (-2 to $21 \% \text{ K}^{-1}$, a wide range of allowed responses), and a shift within one standard deviation ($6.5 \% \text{ K}^{-1}$) of the observational datasets (8 to $20 \% \text{ K}^{-1}$). The range of acceptable model responses is still quite wide, but half of models do not meet it. Table 4.6 lists the models that do and do not meet the criteria for consistency. Only models that also participated in the RCP8.5 or CO_2 increase experiments are shown. Two examples of model responses are shown in Fig. 4.22, one that is consistent with observations (MPI-ESM-LR) and one that is not (IPSL-CM5A-LR).

Models that are consistent with observations according to this criteria have increases in 99.99th percentile rain rate for RCP8.5 or CO_2 doubling experiments that are at most $9.0 \% \text{ K}^{-1}$. Furthermore, the consistent models are those with a larger initial convective fraction. Models with large increases in extreme precipitation participating in the AMIP experiment are inconsistent with observations.

Table 4.6: CMIP5 models sorted by whether or not their response to ENSO phases in AMIP simulations are consistent with GPCP and TRMM observed responses. To be considered consistent, a model's shift must be within 1 standard deviation ($6.5\% \text{ K}^{-1}$) of the observed shift, $14\% \text{ K}^{-1}$, and its 99.99th percentile rain rate response must also fall with the uncertainty range which spans -2 to $21\% \text{ K}^{-1}$. Only models participating in AMIP as well as either CO_2 doubling or RCP8.5 experiments are included.

Model	AMIP		2xCO ₂		RCP8.5	
	Shift (% K ⁻¹)	$\Delta R_{99.99}$ (% K ⁻¹)	Shift (% K ⁻¹)	$\Delta R_{99.99}$ (% K ⁻¹)	Shift (% K ⁻¹)	$\Delta R_{99.99}$ (% K ⁻¹)
Consistent						
BNU-ESM	12	3.4			2.3	9.0
CMCC-CM	19	2.6	1.8	8.2		
CSIRO-Mk3-6-0	9.9	8.5			3.6	5.0
CanAM4	15	14	2.6	8.9	1.9	7.5
FGOALS-g2	14	8.3			0.41	1.1
INM-CM4	13	9.8			2.8	2.3
IPSL-CM5B-LR	18	20	3.7	3.4	4.0	3.2
MPI-ESM-LR	19	17	5.7	6.3	4.7	6.8
MPI-ESM-MR	17	9.8	5.6	6.9		
Not consistent						
ACCESS1.3	21	0.37	4.0	4.5		
BCC-CSM1.1	30	7.9	4.8	5.8	5.2	8.1
CCSM4	15	27	4.7	9.7	2.8	14
CNRM-CM5	5.9	21			2.0	7.7
FGOALS-s2	25	29	0.18	6.6		
GFDL-CM3	21	30	2.5	9.4	2.8	13
IPSL-CM5A-LR	4.9	17	2.7	12	2.1	21
IPSL-CM5A-MR	0.96	13	2.1	12		
MIROC5	6.8	11	-0.16	4.8	0.77	8.0
MRI-CGCM3	20	31	5.2	16		
NorESM1-M	14	25	3.7	4.1	3.7	9.0

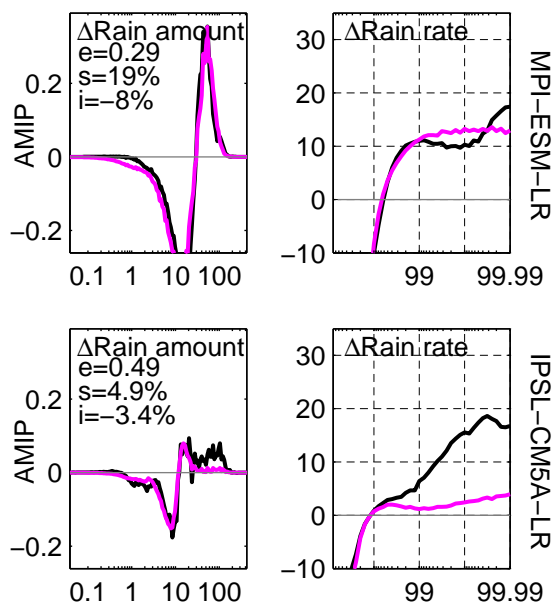


Figure 4.22: MPI-ESM-LR (top) and IPSL-CM5A-LR (bottom) model rain amount (left) and extreme rain rate (right) responses to ENSO phases.

4.6 Discussion

4.6.1 Summary of changes in the distribution of rain

With the analysis above, we are in a position to describe three components of the rain amount response to CO_2 doubling.

First, the rain amount distribution shifts to higher rain rates, and this is captured by the shift-plus-increase. For CO_2 doubling, the shift of $3.3\% \text{ K}^{-1}$ in the multi-model mean indicates that the same amount of rain falls at $3.3\% \text{ K}^{-1}$ higher rain rates, with fewer total events. Simultaneously, the rain frequency and amount distributions increase by $0.9\% \text{ K}^{-1}$. The error of this fit is 0.3, and the increase accounts for 0.9 of $1.5\% \text{ K}^{-1}$, both of which indicate that the shift-plus-increase describes about two-thirds of the change in rain distribution in response to CO_2 doubling.

The rest of the increase in rain amount comes as deviations from this coherent response. A small contribution comes as an increase in light rain over ocean, unrelated

to changes in the distribution. Whether or not this light rain mode is real is questionable, since observations disagree with models in their climatological frequency of light rain, but observations contain many uncertainties of their own.

Finally, there is an increase in the heaviest events, beyond the coherent change in the distribution, in some but not all models, which we have argued above is due to an increase in grid-point storms. These increases contribute most of the remaining third of the increase in total rainfall in the multi-model mean in response to CO₂ doubling, and grid-point storms contribute more with increased CO₂ forcing.

4.6.2 Reconciling energetic and moisture constraints

We are also in a position to articulate how energetic and moisture constraints can be simultaneously met. First, the energetic constraint is met by the total increase in rain amount. In the previous section, we saw that this consists primarily of the increase mode, and secondarily the extreme mode.

But moisture, and moisture convergence, increase much more than the total rainfall. First, consider models like MPI-ESM-LR, in which the extreme precipitation change follows closely the shift-plus-increase. The increase mode results in a change in rain rate of just 1.3 % K⁻¹ for the heaviest events, not enough to account for the increased moisture convergence. In order to make up the difference, the energetically-neutral shift mode provides a mechanism for further increases in the heaviest rain rates. The same amount of rain falls at heavier rain rates, so that increased moisture convergence can be accommodated without violating the energetic constraint, or requiring further increases in atmospheric radiative cooling. In this scenario, there would be fewer events governed by moisture convergence, because the shift decreases the frequency of rain events. This implies an increase in dry day frequency (the MPI models have the biggest increase in dry-day frequency). Furthermore, the distribution of vertical velocity would shift to account for these changes in the distribution of rain. This stands in contrast to the idea that changes in the distribution of rain are deter-

mined by changes in moisture and vertical velocity. It is probably more appropriate to think of circulation and precipitation change as a chicken-and-egg problem.

In models with an extreme mode, like the IPSL and GFDL models, the shift accounts for less of the extreme rain rate response, which is instead accounted for by the extreme mode. These large increases of extreme rain rate are not accompanied by increases in dry day frequency, since they contribute little to the total frequency. The model whose 99.9th percentile rain response was least captured by the precipitation extremes scaling in O’Gorman and Schneider (2009a) was GFDL CM2.0, a predecessor to the GFDL-ESM2G (though, the GFDL CM2.1 model was better captured by the scaling). This scaling assumes that changes are linear, whereas grid point storms may not respond linearly.

4.6.3 Changes in vertical velocity

Figure 4.23 shows the pressure vertical velocity (ω) and its change for the MPI, IPSL, and GFDL models. The distribution was calculated by calculating the average vertical velocity at 500 hPa for all days with rain rates falling in each bin, and then take the global average of the distribution.

The vertical velocity distribution for the MPI model is simplest. At heavy rain rates, vertical motion is upward (negative), while at light rain rates it is upward. In response to warming over the century, both upward and downward motions get stronger. This response seems plausible. For the IPSL model, the light events also have downward motion, and heavier events have upward motion, similar to MPI for days with rain rates up to about 20 mm d⁻¹. But, for the events with the heaviest rain rates, ω is downward, which is surprising. The response as a function of percentile is similar to the MPI response, with more downward motion for light events and more upward motion for heavy events. The GFDL vertical velocity distribution is even more complex. Rain events lighter than about 1 mm d⁻¹ have upward motion, light rain events about 1 mm d⁻¹ have downward motion, events around 10 mm d⁻¹

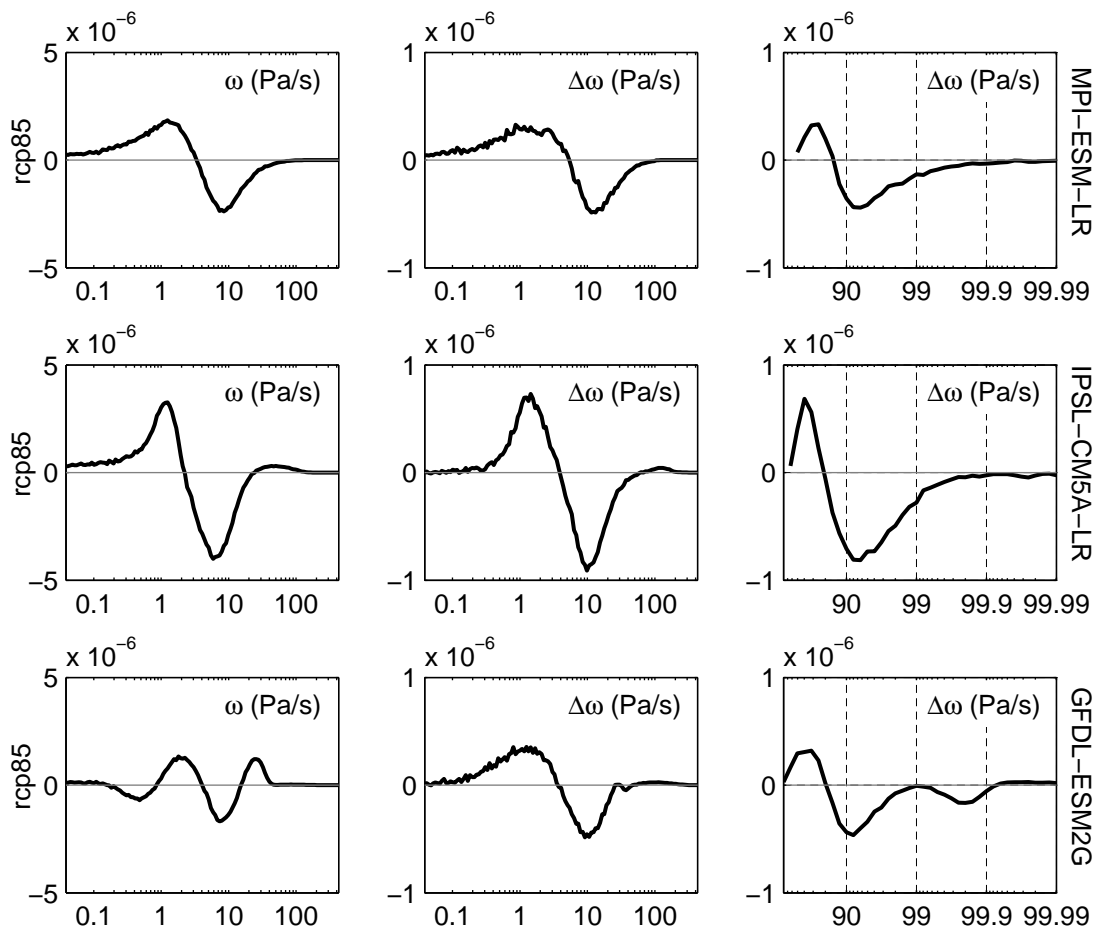


Figure 4.23: Pressure vertical velocity at 500 hPa in Pa s^{-1} (left) and its change (center) as a function of rain rate, and pressure vertical velocity change as a function of cumulative percentile (right) for MPI-ESM-LR (top), IPSL-CM5A-LR (middle), and GFDL-ESM2G (bottom) models for the RCP8.5 scenario.

have upward motion, and the heaviest events have downward motion. The change in pressure vertical velocity shows more downward motion at light rain rates, and more upward motion for events from the 90th through the 99.9th percentiles. The initial distribution of the GFDL model is difficult to rationalize as realistic. Further analysis of the relationship between vertical velocity and the distribution of rain could elucidate the substantial differences among models.

4.7 Conclusions

We have considered the change in rain amount and rain frequency distribution of daily precipitation data in response to CO₂ increase and warm and cold phases of ENSO in CMIP5 models, and to ENSO phases in GPCP 1DD and TRMM 3B42 version 7 observational datasets.

CMIP5 models do a tolerable job of simulating the global distribution of rain amount by rain rate when compared to the GPCP 1DD observational dataset. The models overestimate the frequency of rain falling at light rain rates, but the rain amount contributed at these light rates is small.

We introduce two modes of coherent change of the rain amount distribution: an increase in rain amount at all rain rates, and a shift of the rain amount distribution to higher rain rates. The increase changes total rainfall, while the shift does not. The degree of shift is expressed as a percentage change in rain rate, representing a movement of the rain amount distribution along an axis of the log of rain rate. The increase is expressed as a percentage change in rain amount at all rain rates.

We fit the shift and increase of the rain amount distribution to the response of models and observations to CO₂ increase and warm and cold ENSO phases, and considered this coherent response as well as the deviations from it. In response to CO₂ doubling in CMIP5 models, the rain amount distribution shifts by 3.3 % K⁻¹ and increases by about 1 % K⁻¹. Observational datasets disagree with each other about the change in mean rainfall over ocean. Nonetheless, the shift-plus-increase fits

much of the change in rain amount reasonably in all cases, reinforcing our confidence in the framework. Despite disagreement about total rain, AMIP model simulations and both observational datasets produce a similar shift, between 14 and 15 % K^{-1} during ENSO events.

The response of the rain frequency as a function of rain rate and extreme rain rate as a function of percentile are also included in the framework. In response to warming, dry-day frequency increases in models and observations. It increases more over land than over the ocean. However, the increase in the modeled and observed response is smaller than the fitted shift-plus-increase, indicating that increased drying is more modest than we might have anticipated from changes in the rest of the distribution alone.

In response to CO_2 doubling, some of the models have increases of extreme precipitation (greater than the 99th percentile) that closely follow the shift-plus-increase fitted to each model's change in rain amount distribution. Other models produce much bigger increases in extreme precipitation than the shift-plus-increase, indicating that extreme precipitation change is not tied to the change in the rest of the rain amount distribution in these models. We attribute these additional increases in very heavy rain rate to changes in large-scale precipitation probably related to grid-point storms.

CMIP5 models have more light rain (around 1 mm d^{-1}) than observations, and they have an increase in light rain over ocean in response to CO_2 doubling. This light rain and its change contribute little to the total amount of rainfall, so they are not tightly constrained by the atmospheric energy budget.

These results indicate that with warming, rainfall shifts to higher rain rates, as argued by Trenberth (1999), but the rate of change is smaller than the increase in moisture and extreme events. The very high rate of increase of extreme precipitation found in some studies (e.g., Allen and Ingram, 2002; Sugiyama et al., 2010; O'Gorman, 2012) is not associated with changes in the rest of the distribution of rain.

Chapter 5

CONCLUDING REMARKS

In this dissertation, we have considered how atmospheric radiative cooling changes in response to carbon dioxide and black carbon forcings, how these changes in the atmospheric radiative cooling are related to changes in global-mean precipitation, and how this change in global-mean precipitation manifests as changes in the rate at which rain falls. We have focused on diagnostic analysis of a suite of comprehensive climate model simulations and their evolution over the rest of this century in response to greenhouse gas forcing.

In CMIP3 experiments with realistic forcing, we saw that differences in global-mean precipitation increase across models are strongly related to changes in clear-sky shortwave absorption in the atmosphere. We focused on two models: the one with the largest rate of precipitation increase and the one with the smallest rate of increase. We showed that the model with the largest increase in precipitation has a decrease in absorbing aerosol forcing, while the model with the smallest increase in precipitation has an increase in absorbing aerosol forcing. This example illustrates how potent absorption of shortwave radiation in the atmosphere by aerosols can be for precipitation. Comprehensive model comparisons are used for many applications and research studies, so this finding is also important for other users of the dataset.

Around the time this work was undertaken, other groups were also documenting how important black carbon is for global-mean precipitation. Frieler et al. (2011) showed that the black carbon forcing was needed to explain differences in precipitation change across models and emissions scenarios in CMIP3. More recent work has tried to establish a bound on many aspects of black carbon in climate (Bond et al., 2013),

which has been an elusive climate forcing despite its impacts.

In CMIP5 experiments forced by carbon dioxide increase, we made a detailed accounting of the clear-sky atmospheric radiative cooling response that balances the change in global-mean precipitation. We saw that much of this response is due to vertically-uniform warming and moistening at constant relative humidity, as well as the carbon dioxide forcing itself. In contrast to the top-of-atmosphere water vapor feedback, moistening contributes to an increase in longwave cooling of the atmospheric column. Inter-model spread in atmospheric longwave cooling was also examined. Also in contrast to the top-of-atmosphere, the responses of clear-sky atmospheric radiative cooling to changes in water vapor and lapse rate do not show compensation. They each contribute to the range in model longwave cooling response.

This work made an important contribution by presenting consistent calculations that documented the contributions from warming, moistening, and carbon dioxide forcing. Future work on this topic could investigate why clear-sky shortwave absorption due to water vapor differs among climate models. While clear-sky radiative cooling is the dominant factor for changes atmospheric radiative cooling, progress could be made understanding the role that clouds play, why it is not bigger, and whether the response of clouds and sensible heat flux are connected.

To address how the distribution of precipitation responds to climate change, we devised two modes of coherent change of the rain amount distribution: a shift mode and an increase mode. The increase mode is the component of change that is uniform at all rain rates. The shift mode is an energetically-neutral movement of rain from lower rain rates to higher rates. We fit these modes to CMIP5 model simulations forced by increasing carbon dioxide, CMIP5 simulations of the response to warm and cold ENSO phases, and two merged satellite-gauge gridded observational precipitation datasets over warm and cold phases of ENSO. These two modes explain most of the change in rain amount distribution in these cases. In the CMIP5 multi-model mean response to carbon dioxide increase, the shift and increase together explain about

two thirds of the change in rain. In some models, but not others, an extreme mode where precipitation increases at the highest rain rates drives the change in extreme rain rate, and also contributes to the increase in total rainfall.

The shift mode quantifies how increases in heavy rain events could be related to decreasing frequency of all rain events under the constraint of a limited ability to change the total rainfall. If the shift mode were responsible for the entire increase in extreme rain rate, then we would expect to see increases in dry-day frequency, as Trenberth (1999) envisioned. But in the model simulations we looked at in this dissertation, the extreme mode (instead of the shift mode) is responsible for a substantial component of the extreme rain increase. The extreme mode is not associated with substantial increases in dry-day frequency. In summary, extreme rain events will get heavier, but models disagree on whether this implies a substantial increase in the frequency of dry events or merely a small one.

The increase and shift modes of change of the rain distribution introduced in this work are novel contribution to the discussion of how rain can change. Future work could establish the changes in moisture and circulation that accompany the shift mode and the mechanisms driving the response. There is also more work to be done to understand the differences among model rain distributions and how they relate to circulation change.

This dissertation focused on understanding long-term changes in precipitation and its drivers by starting from the very largest scales. The goal for this work is for it to form a basis upon which to connect the response of rainfall at smaller scales, especially in space. Ultimately, it is the precipitation at the regional scale which is relevant for both dynamical responses of climate and impacts on the environment and society. We hope that by providing a solid foundation that connects the large-scale precipitation response to fundamental aspects of long-term climate change, this work will support future advances in our understanding of climate at all scales.

BIBLIOGRAPHY

- Ackerman, A. S., O. B. Toon, D. E. Stevens, A. J. Heymsfield, V. Ramanathan, and E. J. Welton, 2000: Reduction of tropical cloudiness by soot. *Science*, **288** (5468), 1042–1047, doi:10.1126/Science.288.5468.1042.
- Allan, R. P., 2006: Variability in clear-sky longwave radiative cooling of the atmosphere. *J. Geophys. Res.*, **111**, D22 105, doi:10.1029/2006JD007304.
- Allan, R. P., C. Liu, M. Zahn, D. A. Lavers, E. Koukouvagias, and A. Bodas-Salcedo, 2013: Physically consistent responses of the global atmospheric hydrological cycle in models and observations. *Surv. Geophys.*, 1–20, doi:10.1007/s10712-012-9213-z.
- Allan, R. P. and B. J. Soden, 2008: Atmospheric warming and the amplification of precipitation extremes. *Science*, **321** (5895), 1481–1484, doi:10.1126/science.1160787.
- Allan, R. P., B. J. Soden, V. O. John, W. Ingram, and P. Good, 2010: Current changes in tropical precipitation. *Environ. Res. Lett.*, **5** (2), 025 205, doi:10.1088/1748-9326/5/2/025205.
- Allen, M. R. and W. J. Ingram, 2002: Constraints on future changes in climate and the hydrologic cycle. *Nature*, **419** (6903), 224–232, doi:10.1038/nature01092.
- Andrews, T., P. M. Forster, O. Boucher, N. Bellouin, and A. Jones, 2010: Precipitation, radiative forcing and global temperature change. *Geophys. Res. Lett.*, **37**, L14 701, doi:10.1029/2010GL043991.
- Boer, G. J., 1993: Climate change and the regulation of the surface moisture and energy budgets. *Clim. Dyn.*, **8** (5), 225–239, doi:10.1007/BF00198617.

- Bond, T., et al., 2013: Bounding the role of black carbon in the climate system: A scientific assessment. *J. Geophys. Res.*, doi:10.1002/jgrd.50171.
- Bony, S., et al., 2006: How well do we understand and evaluate climate change feedback processes? *J. Clim.*, **19** (15), 3445–3482, doi:10.1175/JCLI3819.1.
- Cess, R. D., 1975: Global climate change: an investigation of atmospheric feedback mechanisms. *Tellus*, **27** (3), 193–198, doi:10.1111/j.2153-3490.1975.tb01672.x.
- Chen, C.-T. and T. Knutson, 2008: On the verification and comparison of extreme rainfall indices from climate models. *J. Clim.*, **21** (7), 1605–1621, doi:10.1175/2007JCLI1494.1.
- Chou, C., C.-A. Chen, P.-H. Tan, and K. T. Chen, 2012: Mechanisms for global warming impacts on precipitation frequency and intensity. *J. Clim.*, **25** (9), 3291–3306, doi:10.1175/JCLI-D-11-00239.1.
- Chuang, C. C., J. E. Penner, J. M. Prospero, K. E. Grant, G. H. Rau, and K. Kawamoto, 2002: Cloud susceptibility and the first aerosol indirect forcing: Sensitivity to black carbon and aerosol concentrations. *J. Geophys. Res.*, **107** (D21), 4564, doi:10.1029/2000JD000215.
- Chung, C. E., V. Ramanathan, D. Kim, and I. A. Podgorny, 2005: Global anthropogenic aerosol direct forcing derived from satellite and ground-based observations. *J. Geophys. Res.*, **110** (D24), D24 207, doi:10.1029/2005JD006356.
- Collins, W., et al., 2006: Radiative forcing by well-mixed greenhouse gases: Estimates from climate models in the Intergovernmental Panel on Climate Change (IPCC) Fourth Assessment Report (AR4). *J. Geophys. Res.*, **111** (D14), doi:10.1029/2005JD006713.

- Costa, S. M. S. and K. P. Shine, 2012: Outgoing longwave radiation due to directly transmitted surface emission. *J. Atmos. Sci.*, **69** (6), 1865–1870, doi:10.1175/JAS-D-11-0248.1.
- Dufresne, J.-L., et al., 2013: Climate change projections using the IPSL-CM5 earth system model: From CMIP3 to CMIP5. *Clim. Dyn.*, 1–43, doi:10.1007/s00382-012-1636-1.
- Dunne, J. P., et al., 2012: GFDL’s ESM2 global coupled climate-carbon earth system models. Part I: Physical formulation and baseline simulation characteristics. *J. Clim.*, **25** (19), 6646–6665, doi:10.1175/JCLI-D-11-00560.1.
- Emori, S. and S. Brown, 2005: Dynamic and thermodynamic changes in mean and extreme precipitation under changed climate. *Geophys. Res. Lett.*, **32** (17), L17706, doi:10.1029/2005GL023272.
- Frieler, K., M. Meinshausen, T. S. v. Deimling, T. Andrews, and P. Forster, 2011: Changes in global-mean precipitation in response to warming, greenhouse gas forcing and black carbon. *Geophys. Res. Lett.*, **38**, 5 PP., doi:201110.1029/2010GL045953.
- Fu, Q. and K. N. Liou, 1992: On the correlated k-distribution method for radiative transfer in nonhomogeneous atmospheres. *J. Atmos. Sci.*, **49** (22), 2139–2156.
- Giorgetta, M. A., et al., 2013: Climate and carbon cycle changes from 1850 to 2100 in MPI-ESM simulations for the Coupled Model Intercomparison Project phase 5. *J. Adv. Model. Earth Syst.*, **5** (3), 572–597, doi:10.1002/jame.20038.
- Gonzalez, R. C. and R. E. Woods, 2002: *Digital image processing*. 2d ed., Prentice Hall, Upper Saddle River, NJ, 793 pp.
- Held, I. and K. Shell, 2012: Using relative humidity as a state variable in climate feedback analysis. *J. Clim.*, **25** (8), 2578–2582, doi:10.1175/JCLI-D-11-00721.1.

- Held, I. M. and B. J. Soden, 2000: Water vapor feedback and global warming. *Annu. Rev. Energy Environ.*, **25** (1), 441–475.
- Held, I. M. and B. J. Soden, 2006: Robust responses of the hydrological cycle to global warming. *J. Clim.*, **19** (21), 5686–5699, doi:10.1175/JCLI3990.1.
- Held, I. M., M. Zhao, and B. Wyman, 2007: Dynamic radiative-convective equilibria using gcm column physics. *J. Atmos. Sci.*, **64** (1), 228–238, doi:10.1175/JAS3825.11.
- Horowitz, L. W., 2006: Past, present, and future concentrations of tropospheric ozone and aerosols: Methodology, ozone evaluation, and sensitivity to aerosol wet removal. *J. Geophys. Res.*, **111** (D22), D22 211, doi:10.1029/2005JD006937.
- Horowitz, L. W., et al., 2003: A global simulation of tropospheric ozone and related tracers: Description and evaluation of Mozart, version 2. *J. Geophys. Res.*, **108** (D24), 4784, doi:10.1029/2002Jd002853.
- Huffman, G. J., R. F. Adler, M. M. Morrissey, D. T. Bolvin, S. Curtis, R. Joyce, B. McGavock, and J. Susskind, 2001: Global precipitation at one-degree daily resolution from multisatellite observations. *Journal of Hydrometeorology*, **2** (1), 36–50, doi:10.1175/1525-7541(2001)002<0036:GPAODD>2.0.CO;2.
- Huffman, G. J., et al., 2007: The TRMM Multisatellite Precipitation Analysis (TMPA): Quasi-global, multiyear, combined-sensor precipitation estimates at fine scales. *J. Hydrometeor.*, **8** (1), 38–55, doi:10.1175/JHM560.1.
- Inamdar, A., V. Ramanathan, and N. Loeb, 2004: Satellite observations of the water vapor greenhouse effect and column longwave cooling rates: Relative roles of the continuum and vibration-rotation to pure rotation bands. *J. Geophys. Res.*, **109** (D6), D06 104, doi:10.1029/2003JD003980.

IPCC, 2007: *Climate Change 2007: The Physical Science Basis. Contribution of Working Group I to the Fourth Assessment Report of the Intergovernmental Panel on Climate Change*. S. Solomon, D. Qin, M. Manning, Z. Chen, M. Marquis, K.B. Averyt, M. Tignor and H.L. Miller, (Eds.). Cambridge University Press, Cambridge, United Kingdom And New York, NY, USA.

IPCC, 2013: *Climate Change 2013: The Physical Science Basis. Contribution of Working Group I to the Fifth Assessment Report of the Intergovernmental Panel on Climate Change*. T. F. Stocker, D. Qin, G.-K. Plattner, M. Tignor, S. K. Allen, J. Boschung, A. Nauels, Y. Xia, V. Bex and P. M. Midgley (Eds.). Cambridge University Press, Cambridge, United Kingdom And New York, NY, USA.

Jones, P., D. Lister, T. Osborn, C. Harpham, M. Salmon, and C. Morice, 2012: Hemispheric and large-scale land-surface air temperature variations: An extensive revision and an update to 2010. *J. Geophys. Res.*, **117** (D5), doi:10.1029/2011JD017139.

Jones, P. W., 1999: First-and second-order conservative remapping schemes for grids in spherical coordinates. *Mon. Wea. Rev.*, **127** (9), 2204–2210.

Kiehl, J. and K. E. Trenberth, 1997: Earth's annual global mean energy budget. *Bull. Amer. Meteorol. Soc.*, **78** (2), 197–208.

Klein Tank, A., et al., 2002: Daily dataset of 20th-century surface air temperature and precipitation series for the european climate assessment. *International Journal of Climatology*, **22** (12), 1441–1453.

Klein Tank, A. M. G., F. W. Zwiers, and X. Zhang, 2009: *Guidelines on analysis of extremes in a changing climate in support of informed decisions for adaptation*. Climate Data and Monitoring WCDMP-No. 72, WMO-TD No. 1500, World Meteorological Organization, Geneva, Switzerland, 56 pp.

- Kopparla, P., E. Fischer, C. Hannay, and R. Knutti, 2013: Improved simulation of extreme precipitation in a high resolution atmosphere model. *Geophys. Res. Lett.*, doi:10.1002/2013GL057866.
- Kvalevåg, M. M., B. H. Samset, and G. Myhre, 2013: Hydrological sensitivity to greenhouse gases and aerosols in a global climate model. *Geophys. Res. Lett.*, **40**, 1432–1438, doi:10.1002/grl.50318.
- Lamarque, J.-F., G. P. Kyle, M. Meinshausen, K. Riahi, S. J. Smith, D. P. van Vuuren, A. J. Conley, and F. Vitt, 2011: Global and regional evolution of short-lived radiatively-active gases and aerosols in the Representative Concentration Pathways. *Clim. change*, **109** (1-2), 191–212, doi:10.1007/s10584-011-0155-0.
- Lambert, F. H. and M. R. Allen, 2009: Are changes in global precipitation constrained by the tropospheric energy budget? *J. Clim.*, **22**, 4995–17, doi:10.1175/2008JCLI2135.1.
- Lambert, F. H. and M. J. Webb, 2008: Dependency of global mean precipitation on surface temperature. *Geophys. Res. Lett.*, **35** (16), L16706, doi:10.1029/2008GL034838.
- Lau, W. K.-M., H.-T. Wu, and K.-M. Kim, 2013: A canonical response of precipitation characteristics to global warming from CMIP5 models. *Geophys. Res. Lett.*, **40**, 3163–3169, doi:10.1002/grl.50420.
- Levy, I. I. H., M. D. Schwarzkopf, L. Horowitz, V. Ramaswamy, and K. L. Findell, 2008: Strong sensitivity of late 21st century climate to projected changes in short-lived air pollutants. *J. Geophys. Res.*, **113** (D6), D06102, doi:10.1029/2007JD009176.
- Lin, Y., M. Zhao, Y. Ming, J.-C. Golaz, L. J. Donner, S. A. Klein, V. Ramaswamy, and

- S. Xie, 2013: Precipitation partitioning, tropical clouds and intraseasonal variability in GFDL AM2. *J. Clim.*, **26**, 5453–5466, doi:10.1175/JCLI-D-12-00442.1.
- Liu, C. and R. P. Allan, 2012: Multisatellite observed responses of precipitation and its extremes to interannual climate variability. *J. Geophys. Res.*, **117** (D3), doi:10.1029/2011JD016568.
- Liu, C., R. P. Allan, and G. J. Huffman, 2012: Co-variation of temperature and precipitation in CMIP5 models and satellite observations. *Geophys. Res. Lett.*, **39** (13), doi:10.1029/2012GL052093.
- Loeb, N. G., J. M. Lyman, G. C. Johnson, R. P. Allan, D. R. Doelling, T. Wong, B. J. Soden, and G. L. Stephens, 2012: Observed changes in top-of-the-atmosphere radiation and upper-ocean heating consistent within uncertainty. *Nat. Geosci.*, **5** (2), 110–113, doi:10.1038/ngeo1375.
- Lohmann, U. and J. Feichter, 2005: Global indirect aerosol effects: A review. *Atmos. Chem. Phys.*, **5** (3), 715–737, doi:10.5194/acp-5-715-2005.
- Lorenz, D. J., E. T. DeWeaver, and D. J. Vimont, 2010: Evaporation change and global warming: The role of net radiation and relative humidity. *J. Geophys. Res.*, **115**, D20 118, doi:201010.1029/2010JD013949.
- Manabe, S. and R. T. Wetherald, 1967: Thermal equilibrium of the atmosphere with a given distribution of relative humidity. *Journal of the Atmospheric Sciences*, **24** (3), 241–259.
- Mauritsen, T., et al., 2012: Tuning the climate of a global model. *J. Adv. Model. Earth Syst.*, **4** (3), doi:10.1029/2012MS000154.
- McCusker, K. E., D. S. Battisti, and C. M. Bitz, 2012: The climate response to stratospheric sulfate injections and implications for addressing climate emergencies. *J. Clim.*, **25** (9), 3096–3116, doi:10.1175/JCLI-D-11-00183.1.

- Meehl, G., et al., 2007a: Global climate projections. *Climate Change 2007: The Physical Science Basis. Contribution Of Working Group I To The Fourth Assessment Report Of The Intergovernmental Panel on Climate Change*, S. Solomon, D. Qin, M. Manning, Z. Chen, M. Marquis, K.B. Averyt, M. Tignor and H.L. Miller, (Eds.). Cambridge University Press, Cambridge, United Kingdom and New York, NY, USA.
- Meehl, G. A., C. Covey, K. E. Taylor, T. Delworth, R. J. Stouffer, M. Latif, B. Mcanavey, and J. F. Mitchell, 2007b: The WCRP CMIP3 multimodel dataset: A new era in climate change research. *Bull. Amer. Meteorol. Soc.*, **88 (9)**, 1383–1394, doi:10.1175/BAMS-88-9-1383.
- Meehl, G. A., et al., 2006: Climate change projections for the Twenty-First century and climate change commitment in the CCSM3. *J. Clim.*, **19**, 2597–2616, doi:10.1175/JCLI3746.1.
- Ming, Y., V. Ramaswamy, and G. Persad, 2010: Two opposing effects of absorbing aerosols on global-mean precipitation. *Geophys. Res. Lett.*, **37 (13)**, L13701, doi:10.1029/2010GL042895.
- Mitchell, J. F. B., C. A. Wilson, and W. M. Cunningham, 1987: On CO₂ climate sensitivity and model dependence of results. *Quart. J. Roy. Meteor. Soc.*, **113 (475)**, 293–322, doi:10.1002/qj.49711347517.
- Nakicenovic, N. and R. Swart, (Eds.) , 2000: *Special Report on Emissions Scenarios. A Special Report of Working Group III of the Intergovernmental Panel On Climate Change*. Cambridge University Press, Cambridge, United Kingdom and New York, NY, USA, 599 pp.
- O’Gorman, P. A., 2012: Sensitivity of tropical precipitation extremes to climate change. *Nat. Geosci.*, **5 (10)**, 697–700, doi:10.1038/NGEO1568.

- O’Gorman, P. A., R. P. Allan, M. P. Byrne, and M. Previdi, 2012: Energetic constraints on precipitation under climate change. *Surv. Geophys.*, **33** (3-4), 585–608, doi:10.1007/s10712-011-9159-6.
- O’Gorman, P. A. and T. Schneider, 2008: The hydrological cycle over a wide range of climates simulated with an idealized GCM. *J. Clim.*, **21** (15), 3815–3832, doi:10.1175/2007JCLI2065.1.
- O’Gorman, P. A. and T. Schneider, 2009a: The physical basis for increases in precipitation extremes in simulations of 21st-century climate change. *Proc. Natl. Acad. Sci. U. S. A.*, **106** (35), 14 773–14 777, doi:10.1073/pnas.0907610106.
- O’Gorman, P. A. and T. Schneider, 2009b: Scaling of precipitation extremes over a wide range of climates simulated with an idealized gcm. *J. Clim.*, **22** (21), 5676–5685, doi:10.1175/2009JCLI2701.1.
- Pall, P., M. Allen, and D. Stone, 2007: Testing the Clausius–Clapeyron constraint on changes in extreme precipitation under CO₂ warming. *Clim. Dyn.*, **28** (4), 351–363, doi:10.1007/s00382-006-0180-2.
- Pendergrass, A. and D. Hartmann, in press: The atmospheric energy constraint on global-mean precipitation change. *J. Clim.*, doi:JCLI-D-13-00163.1.
- Pendergrass, A. G. and D. L. Hartmann, 2012: Global-mean precipitation and black carbon in AR4 simulations. *Geophys. Res. Lett.*, **39**, L01 703, doi:201210.1029/2011GL050067.
- Previdi, M., 2010: Radiative feedbacks on global precipitation. *Environ. Res. Lett.*, **5**, 025 211, doi:10.1088/1748-9326/5/2/025211.
- Ramanathan, V. and G. Carmichael, 2008: Global and regional climate changes due to black carbon. *Nat. Geosci.*, **1** (4), 221–227, doi:10.1038/Ngeo156.

- Ramanathan, V., P. J. Crutzen, J. T. Kiehl, and D. Rosenfeld, 2001: Aerosols, climate, and the hydrological cycle. *Science*, **294** (5549), 2119–2124, doi:10.1126/science.1064034.
- Richter, I. and S.-P. Xie, 2008: Muted precipitation increase in global warming simulations: A surface evaporation perspective. *J. Geophys. Res.*, **113** (D24118), doi:10.1029/2008JD010561.
- Roberts, D. L. and A. Jones, 2004: Climate sensitivity to black carbon aerosol from fossil fuel combustion. *J. Geophys. Res.*, **109** (D16), D16 202, doi:10.1029/2004JD004676.
- Rossow, W. B., A. Mekonnen, C. Pearl, and W. Goncalves, 2013: Tropical precipitation extremes. *J. Clim.*, **26** (4), 1457–1466, doi:10.1175/JCLI-D-11-00725.1.
- Schneider, S. H., 1972: Cloudiness as a global climatic feedback mechanism: The effects on the radiation balance and surface temperature of variations in cloudiness. *J. Atmos. Sci.*, **29** (8), 1413–1422.
- Shiogama, H., K. Takahashi, T. Nagashima, T. Ogura, T. Nozawa, S. Emori, and T. Takemura, 2009: Emission scenario dependency of precipitation on global warming in the MIROC3.2 model. *J. Clim.*, doi:10.1175/2009JCLI3428.1.
- Shiogama, H., et al., 2010: Emission scenario dependencies in climate change assessments of the hydrological cycle. *Clim. Change*, **99** (1), 321–329, doi:10.1007/S10584-009-9765-1.
- Soden, B. J. and I. M. Held, 2006: An assessment of climate feedbacks in coupled ocean–atmosphere models. *J. Clim.*, **19** (14), 3354–3360, doi:10.1175/JCLI3799.1.
- Stephens, G. L. and T. D. Ellis, 2008: Controls of global-mean precipitation increases in global warming GCM experiments. *J. Clim.*, **21**, 6141–6155, doi:10.1175/2008JCLI2144.1.

- Stephens, G. L., et al., 2010: Dreary state of precipitation in global models. *J. Geophys. Res.*, **115** (D24), D24 211, doi:10.1029/2010JD014532.
- Stephens, G. L., et al., 2012: An update on earth's energy balance in light of the latest global observations. *Nat. Geosci.*, doi:10.1038/ngeo1580.
- Sugiyama, M., H. Shiogama, and S. Emori, 2010: Precipitation extreme changes exceeding moisture content increases in MIROC and IPCC climate models. *Proc. Natl. Acad. Sci. U. S. A.*, **107** (2), 571–575, doi:10.1073/pnas.0903186107.
- Sun, Y., S. Solomon, A. Dai, and R. W. Portmann, 2006: How often does it rain? *J. Clim.*, **19** (6), 916–934, doi:10.1175/JCLI3672.1.
- Sun, Y., S. Solomon, A. Dai, and R. W. Portmann, 2007: How often will it rain? *Journal of Climate*, **20** (19), 4801–4818, doi:10.1175/JCLI4263.1.
- Takahashi, K., 2009a: The global hydrological cycle and atmospheric shortwave absorption in climate models under CO₂ forcing. *J. Clim.*, **22** (21), 5667–5675, doi:10.1175/2009JCLI2674.1.
- Takahashi, K., 2009b: Radiative constraints on the hydrological cycle in an idealized radiative–convective equilibrium model. *J. Atmos. Sci.*, **66** (1), 77–91, doi:10.1175/2008JAS2797.1.
- Taylor, K. E., R. J. Stouffer, and G. A. Meehl, 2012: An overview of CMIP5 and the experiment design. *Bull. Amer. Meteor. Soc.*, **93** (4), 485–498, doi:10.1175/BAMS-D-11-00094.1.
- Trenberth, K. E., 1997: The definition of El Niño. *Bull. Amer. Meteorol. Soc.*, **78** (12), 2771–2777.
- Trenberth, K. E., 1999: Conceptual framework for changes of extremes of the hydrological cycle with climate change. 327–339, doi:10.1007/978-94-015-9265-9_18.

- Trenberth, K. E., 2011: Changes in precipitation with climate change. *Clim. Res.*, **47** (1), 123, doi:10.3354/cr00953.
- Trenberth, K. E., A. Dai, R. M. Rasmussen, and D. B. Parsons, 2003: The changing character of precipitation. *Bull. Amer. Meteorol. Soc.*, **84** (9), 1205–1217, doi:10.1175/BAMS-84-9-1205.
- Vecchi, G. A. and B. J. Soden, 2007: Global warming and the weakening of the tropical circulation. *J. Clim.*, **20** (17), 4316–4340, doi:10.1175/JCLI4258.1.
- Watterson, I. and M. Dix, 2003: Simulated changes due to global warming in daily precipitation means and extremes and their interpretation using the gamma distribution. *J. Geophys. Res.*, **108** (D13), 4379, doi:10.1029/2002JD002928.
- Wigley, T., S. J. Smith, and M. Prather, 2002: Radiative forcing due to reactive gas emissions. *J. Clim.*, **15** (18), 2690–2696.
- Zelinka, M. D. and D. L. Hartmann, 2010: Why is longwave cloud feedback positive? *J. Geophys. Res.*, **115**, D16 117, doi:10.1029/2010JD013817.
- Zelinka, M. D., S. A. Klein, and D. L. Hartmann, 2012: Computing and partitioning cloud feedbacks using cloud property histograms. Part II: attribution to changes in cloud amount, altitude, and optical depth. *J. Clim.*, **25** (11), 3736–3754, doi:10.1175/JCLI-D-11-00249.1.
- Zhang, M., J. Hack, J. Kiehl, and R. Cess, 1994: Diagnostic study of climate feedback processes in atmospheric general circulation models. *J. Geophys. Res.*, **99** (D3), 5525–5537, doi:10.1029/93JD03523.

Appendix A

MODEL SIMULATIONS

The Coupled Model Intercomparison Project, phases 3 and 5 (CMIP3 and CMIP5), is run by the World Climate Research Programme's (WCRP) Working Group on Climate Modeling. Model simulations analyzed in this dissertation were generously produced and provided by modeling centers from around the world, and coordinated by the WCRP. The U.S. Department of Energy's Program for Climate Model Diagnosis and Intercomparison archives and makes the model simulations available, in partnership with the Global Organization for Earth System Science Portals. Table 2.1 lists models whose simulations were analyzed in Chapter 2. Table A.1 lists models whose simulations were analyzed in Chapters 3 and 4.

Table A.1: CMIP5 model simulations analyzed in this dissertation.

Modeling center	Model name	Chapter 3	Chapter 4		
		1pctCO2	1pctCO2	RCP8.5	AMIP
Commonwealth Scientific and Industrial Research Organization and Bureau of Meteorology CSIRO-BOM, Australia	ACCESS1.0	x	x		
	ACCESS1.3		x		x
Beijing Climate Center, China Meteorological Administration	BCC-CSM1.1	x	x	x	x
College of Global Change and Earth System Science, Beijing Normal University	BNU-ESM			x	x
Canadian Centre for Climate Modelling and Analysis	CanESM2	x	x	x	
	CanAM4				x
National Center for Atmospheric Research	CCSM4	x		x	x
Community Earth System Model Contributors	CESM1-BGC		x	x	
Centro Euro-Mediterraneo per I Cambiamenti Climatici	CMCC-CESM			x	
	CMCC-CM		x		x
	CMCC-CMS			x	
Centre National de Recherches Météorologiques / Centre Européen de Recherche et Formation Avancée en Calcul Scientifique	CNRM-CM5	x	x	x	x
Commonwealth Scientific and Industrial Research Organization in collaboration with Queensland Climate Change Centre of Excellence	CSIRO-Mk3.6.0			x	x
EC-EARTH consortium	EC-EARTH				x
LASG, Institute of Atmospheric Physics, Chinese Academy of Sciences and CESS, Tsinghua	FGOALS-g2			x	x
LASG, Institute of Atmospheric Physics, Chinese Academy of Sciences	FGOALS-s2		x		x

Modeling center	Model name	Chapter 3	Chapter 4		
		1pctCO2	1pctCO2	RCP8.5	AMIP
NOAA Geophysical Fluid Dynamics Laboratory	GFDL-CM3	x	x	x	x
	GFDL-ESM2G	x	x	x	
	GFDL-ESM2M	x	x	x	
	GFDL-HIRAM-C180				x
	GFDL-HIRAM-C360				x
NASA Goddard Institute for Space Studies	GISS-E2-R	x			x
Met Office Hadley Centre (additional HadGEM2-ES realizations contributed by Instituto Nacional de Pesquisas Espaciais)	HadGEM2-ES HadGEM2-A		x		x
Institute for Numerical Mathematics	INM-CM4	x		x	x
Institut Pierre-Simon Laplace	IPSL-CM5A-LR	x	x	x	x
	IPSL-CM5A-MR	x	x		x
	IPSL-CM5B-LR	x	x	x	x
Japan Agency for Marine-Earth Science and Technology, Atmosphere and Ocean Research Institute (The University of Tokyo), and National Institute for Environmental Studies	MIROC-ESM MIROC-ESM-CHEM	x	x	x	
Atmosphere and Ocean Research Institute (The University of Tokyo), National Institute for Environmental Studies, and Japan Agency for Marine-Earth Science and Technology	MIROC5	x	x	x	x
Max-Planck-Institut für Meteorologie (Max Planck Institute for Meteorology)	MPI-ESM-LR		x	x	x
	MPI-ESM-MR		x		x
	MPI-ESM-P		x		
Meteorological Research Institute	MRI-CGCM3	x	x		
	MRI-AGCM3.2H				x
	MRI-AGCM3.2S				x
Norwegian Climate Center	NorESM1-M	x	x	x	x
	NorESM1-ME	x			

Appendix B

RAIN AMOUNT AND RAIN FREQUENCY DISTRIBUTION CALCULATIONS

We calculate the distribution of rain amount p and rain frequency f for each dataset, using daily rain accumulation r from model output or gridded observations. R_i^l and R_i^r are left and right bin edges, $R_i^c = (R_i^l + R_i^r)/2$ are bin centers, which we use in transforming the distribution.

$$p_i(R_i^c) = \frac{1}{\Delta \ln R} \int_{\ln R_i^l}^{\ln R_i^r} p(\ln r) d \ln r = \frac{1}{\Delta \ln R} \sum_{gridpts} r(R_i^l \leq r \leq R_i^r) \frac{A_{gridpt}}{A_{total}}, \quad (\text{B.1})$$

$$f_i(R_i^c) = \frac{1}{\Delta \ln R} \int_{\ln R_i^l}^{\ln R_i^r} f(\ln r) d \ln r = \frac{1}{\Delta \ln R} \sum_{gridpts} \frac{N_d(R_i^l \leq r \leq R_i^r)}{\Sigma N_d} \frac{A_{gridpt}}{A_{total}}, \quad (\text{B.2})$$

$$F_d = \frac{1}{\Sigma N_d} \sum_{gridpts} N_d(r = 0) \frac{A_{gridpt}}{A_{total}}, \quad (\text{B.3})$$

where A are areas of each gridpoint and the total area, and N_d is the number of days. The distributions are calculated a bin width $\Delta \ln R = (R_{i+1} - R_i)/R_i = 7.67\%$, which gives reasonable sampling across the distribution.

We use the daily convective rainfall accumulation r_{conv} to calculate the distribution of convective rain amount p^{conv} and convective precipitation fraction f^{conv} in each bin of daily rain rate r ,

$$p_i^{conv}(R_i^c) = \frac{1}{\Delta \ln R} \sum_{gridpts} r_{conv}(R_i^l \leq r \leq R_i^r) \frac{A_{gridpt}}{A_{total}}, \quad (\text{B.4})$$

$$f_i^{conv}(R_i^c) = \frac{1}{\Delta \ln R} \sum_{gridpts} \frac{r_{conv}}{r}(R_i^l \leq r \leq R_i^r) \frac{A_{gridpt}}{A_{total}}. \quad (\text{B.5})$$

VITA

Angeline Greene Pendergrass grew up in South Bend, Indiana and Crystal Lake, Illinois, the daughter of a chemist and environmental engineer. Hours spent watching The Weather Channel, sighting a tornado from a pool party on her birthday, and experiencing the difference in climate up- and down-wind of Lake Michigan were early influences that pushed her toward studying the atmosphere. In high school she enjoyed and excelled at physics and math, and was valedictorian of the Crystal Lake South class of 2002. She then went to college at the University of Miami, where she graduated *magna cum laude* with majors in meteorology, math, and physics and a minor in French. She entered the Department of Atmospheric Sciences in 2006 and completed a masters degree studying paleoclimate data assimilation. She then traveled to the South Pacific for a brief foray on an oceanographic research vessel before finding her true calling studying the rain. In addition to atmospheric science, she loves the water and traveling. She has spent much of her free time in Seattle swimming and kayaking in Lake Washington and other nearby waterways. She has visited all fifty states and four continents. The next leg of her journey will bring her to the National Center for Atmospheric Research in Boulder, Colorado where she will continue her research on rain as an Advanced Studies Program postdoctoral fellow.